



## Monte Carlo Study of TeV-Scale String Resonances in Photon-Jet Scattering Events at the LHC

An attempt to discover extra dimensions and prove string theory

by

**Kyle Drury**

Supervised by Dr. Douglas Gingrich

A research report presented for NSERC 2023



Department of Physics and Astronomy  
The University of Alberta  
Canada  
2023/08/09

## Dedications and Acknowledgements

First and foremost, I'd like to dedicate this report to my friend and peer Udbhav Ram, whose own work and research from a young age motivated and inspired me to do the same. Your guidance and assistance in my learning to code and sending applications bestowed me with this opportunity.

I'd like to thank my supervisor, Dr. Douglas Gingrich, for agreeing to work with me, and whose patience and wisdom were instrumental in my success.

Thank you, Mom, Dad, and Ryan. Your love has always been my engine. Babi and Dziadzio, I could not have asked for more amazing grandparents; and to Dziadzio, thank you for always nurturing my curiosity and being a shining example of how to constantly pursue knowledge. Thank you also to my Auntie Anna and Uncle Mike. Lauren and Megan, I wish you luck in your future endeavours and I hope your passions will bring you as much happiness as mine does me.

I thank all of my long-time friends; Alex Davis, Benjamin Childerhose, Douglas Chen, Geoffrey Bowen, Michele Fiore, Nathan Dunne, Phoenix Pullen, and Saad Zaki, who have all encouraged and strengthened me through times of hardship. It's easy to succeed when so many people have your back.

Finally, I'd like to thank my physics friends & colleagues from McMaster University, BRO 3A03, for their continued support. Amanda Takacs, Jackson Roden, Madeline Perry, and William Marinache; in Clancy, we trust.

## Abstract

We conduct a Monte Carlo study with STRINGS and Pythia for evidence of low TeV-scale string resonances in  $gg \rightarrow g\gamma$  and  $gq \rightarrow q\gamma$  subprocesses on the order of a few TeV. If the extra compacted spatial dimensions predicted by string theory are sufficiently large, then the fundamental string scale  $M_s$  will also be on the order of a few TeV, energy levels attainable by the Large Hadron Collider (LHC) at CERN. Proton-proton ( $pp$ ) collisions producing string resonances are simulated with STRINGS and Pythia using center-of-mass energies  $\sqrt{s} = 13.0$  and  $13.6$  TeV. We probe string scales  $M_s = [5.0, 7.0]$  TeV in 0.5-TeV steps. The Monte Carlo samples produced in this study can be used for photon-jet scattering resonance searches with ATLAS at the LHC.

# Contents

<b>1</b>	<b>Introduction</b>	<b>6</b>
<b>2</b>	<b>Review of Theory</b>	<b>7</b>
2.1	The Hierarchy Problem . . . . .	7
2.2	String Theory . . . . .	7
2.3	Extra Dimensions and Compactification . . . . .	8
<b>3</b>	<b>Proton Collisions at the LHC</b>	<b>10</b>
3.1	Proton Collision Kinematics . . . . .	10
3.2	Diparton to Parton-Photon Interactions . . . . .	10
3.3	Parton Distribution Functions . . . . .	12
3.4	Scattering Amplitudes and cross-sections . . . . .	12
3.5	Differential Cross-sections . . . . .	14
3.6	Jets . . . . .	15
<b>4</b>	<b>STRINGS Monte Carlo Event Generator</b>	<b>15</b>
4.1	Overview . . . . .	15
4.2	Les Houches Event Files . . . . .	16
<b>5</b>	<b>STRINGS Validation</b>	<b>17</b>
5.1	$\sigma$ Plots . . . . .	17
5.2	Cross-section as a Function of $M_s$ . . . . .	21
<b>6</b>	<b>Analysis</b>	<b>24</b>
6.1	String Scale Selection . . . . .	24
6.2	Sample Generation . . . . .	26
6.2.1	Validity of Samples . . . . .	27
6.3	Kinematic Data . . . . .	27
6.3.1	Angular Distribution Study . . . . .	30
6.4	Pythia Samples . . . . .	31
<b>7</b>	<b>Conclusions</b>	<b>34</b>
<b>8</b>	<b>Sources</b>	<b>35</b>
<b>9</b>	<b>Appendices</b>	<b>36</b>
9.1	$\alpha_s$ Coupling Testing . . . . .	36
9.2	Cross-section vs. $M_s$ Invariant Mass BOI Testing . . . . .	41
9.2.1	Finding $M_{cut}$ . . . . .	42
9.3	Differential Cross-sections . . . . .	44
9.3.1	$M_s = [7, 9]$ TeV . . . . .	44
9.3.2	$M_s = [5, 7]$ TeV . . . . .	46
9.4	Kinematic Data Histograms . . . . .	48
9.4.1	$\sqrt{s} = 13$ TeV, $M_s = 5$ TeV . . . . .	48
9.4.2	$\sqrt{s} = 13$ TeV, $M_s = 5.5$ TeV . . . . .	53
9.4.3	$\sqrt{s} = 13$ TeV, $M_s = 6$ TeV . . . . .	58
9.4.4	$\sqrt{s} = 13$ TeV, $M_s = 6.5$ TeV . . . . .	63
9.4.5	$\sqrt{s} = 13$ TeV, $M_s = 7$ TeV . . . . .	68
9.4.6	$\sqrt{s} = 13.6$ TeV, $M_s = 5$ TeV . . . . .	73
9.4.7	$\sqrt{s} = 13.6$ TeV, $M_s = 5.5$ TeV . . . . .	78
9.4.8	$\sqrt{s} = 13.6$ TeV, $M_s = 6$ TeV . . . . .	83
9.4.9	$\sqrt{s} = 13.6$ TeV, $M_s = 6.5$ TeV . . . . .	88
9.4.10	$\sqrt{s} = 13.6$ TeV, $M_s = 7$ TeV . . . . .	93
9.5	Pythia Kinematic Data . . . . .	98
9.5.1	$M_s = 5$ TeV, $\sqrt{s} = 13$ TeV . . . . .	98
9.5.2	$M_s = 5.5$ TeV, $\sqrt{s} = 13$ TeV . . . . .	99

<b>9.5.3</b>	$M_s = 6 \text{ TeV}, \sqrt{s} = 13 \text{ TeV}$	100
<b>9.5.4</b>	$M_s = 6.5 \text{ TeV}, \sqrt{s} = 13 \text{ TeV}$	101
<b>9.5.5</b>	$M_s = 7 \text{ TeV}, \sqrt{s} = 13 \text{ TeV}$	102
<b>9.5.6</b>	$M_s = 5 \text{ TeV}, \sqrt{s} = 13.6 \text{ TeV}$	103
<b>9.5.7</b>	$M_s = 5.5 \text{ TeV}, \sqrt{s} = 13.6 \text{ TeV}$	104
<b>9.5.8</b>	$M_s = 6 \text{ TeV}, \sqrt{s} = 13.6 \text{ TeV}$	105
<b>9.5.9</b>	$M_s = 6.5 \text{ TeV}, \sqrt{s} = 13.6 \text{ TeV}$	106
<b>9.5.10</b>	$M_s = 7 \text{ TeV}, \sqrt{s} = 13.6 \text{ TeV}$	107
<b>9.6</b>	Data and MC Samples	108
<b>9.7</b>	File Organization on the UofA Local Cluster	108

## List of Abbreviations

- BOI ..... Bounds of integration
- EWS ..... Electroweak Scale
- $g$  ..... Gluon
- $gg$  ..... Gluon-gluon
- $gq$  ..... Gluon-quark
- LHC ..... Large Hadron Collider
- LHE ..... Les Houches Event
- MC ..... Monte Carlo
- $pp$  ..... Proton-proton
- $q$  ..... Quark
- QCD ..... Quantum Chromodynamics
- QFT ..... Quantum Field Theory
- ROI ..... Region of Interest
- SM ..... Standard Model
- $\gamma$  ..... Photon
- TeV ..... Tera-electron-volt
- $\sqrt{s}$  ..... Center-of-mass-energy (energy in the rest frame)

# 1 Introduction

The Standard Model (SM) of particle physics is the most successful theory explaining observed phenomena in the universe. According to the SM, all fundamental particles are zero-dimensional points that can be broken into several categories according to their characteristics. Fermions (quarks or leptons) constitute 'matter,' Bosons, which can be scalar or vectorial in nature, are responsible for mediating the interactions between the fermions.

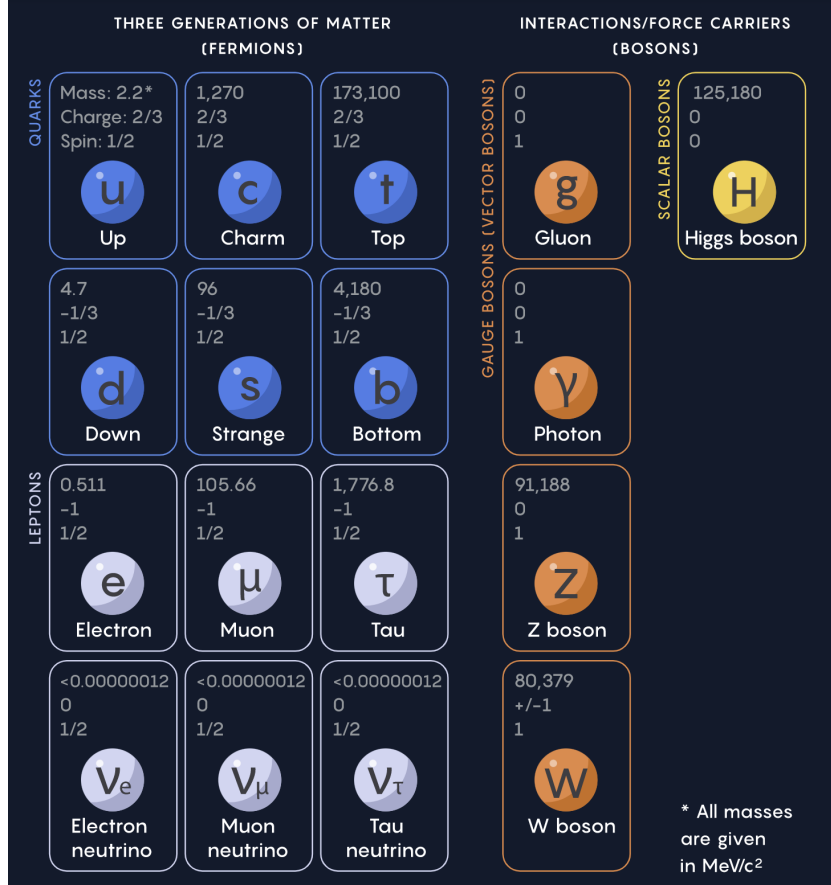


Figure 1: The current standard model [2]

The SM is lacking in some areas and fails to satisfy outstanding issues such as the Hierarchy problem [3]. String theory is a proposed framework that grapples with these issues by describing the fundamental particles of the SM in terms of one-dimensional strings. These strings may be open or closed, and interact with each other in ten-dimensional spacetime.

If the six unperceived spatial dimensions are sufficiently large, the scale of the interactions between strings (the string scale)  $M_s$  should be on the order of a few TeV. By using the Large Hadron Collider (LHC) at CERN to study  $pp$  collisions and the generated string resonances, we can determine if these interactions are being driven by theories predicted by the SM or low-scale string theory. For this project, we focus on observing single-parton scattering processes, which can either be  $gg \rightarrow g\gamma$ , or  $qg \rightarrow q\gamma$ . These interactions manifest at the LHC as  $\gamma + \text{jet}$ .

Section 2 reviews some relevant ideas to low-scale string theory, such as the D-brane model, and the Hierarchy problem. Section 3 discusses the kinematics of  $pp$  collisions simulated by STRINGS, Pythia, and those detected by ATLAS at the LHC. Section 4 outlines the STRINGS MC generator and the basic structure of a .lhe file. In section 5 we validate the STRINGS generator by comparing to previously established literature. In section 6, data collection and analysis is conducted. In section 7, conclusions are made. Sources are listed in section 8, and various appendices are found in section 9.

## 2 Review of Theory

### 2.1 The Hierarchy Problem

Despite the successes of the SM, there is a nagging problem that it cannot come to terms with; there appear to be two different fundamental energy scales of nature. The electroweak scale (EWS)  $m_{EW} \sim 1$  TeV, and the Planck scale  $M_{Pl} \sim 10^{15}$  TeV, which has been experimentally verified. The Planck scale is the energy scale at which gravitational interactions become equal in strength to the other three forces described by the SM. Gravity, which is described by Einstein's theory of general relativity, has yet to be united with the quantum field theory (QFT) framework that the SM is currently based on. The gravitational force seems fundamentally weaker than its peers, the strong and weak nuclear force and the electromagnetic force).

One can easily observe this fact by realizing the force experienced between a typical handheld magnet and a fridge is orders of magnitude greater than the force experienced between a person and the entire Earth he is standing on.

It would appear that our current understanding of gravity may be flawed; because the EWS has been measured at distances far smaller than we are currently capable of measuring gravitational interactions (which are distances of  $\sim 0.01$ m), we may attempt to formulate a new framework that incorporates gravity.

### 2.2 String Theory

The D-brane model, which underpins our current understanding of low-scale string theory, posits that fermions are manifestations of open strings with their ends attached to stacks of D $p$ -branes ( $p$ -dimensional D-brane; a brane is a multidimensional object), while bosons stretch between individual D $p$ -branes in the same stack.

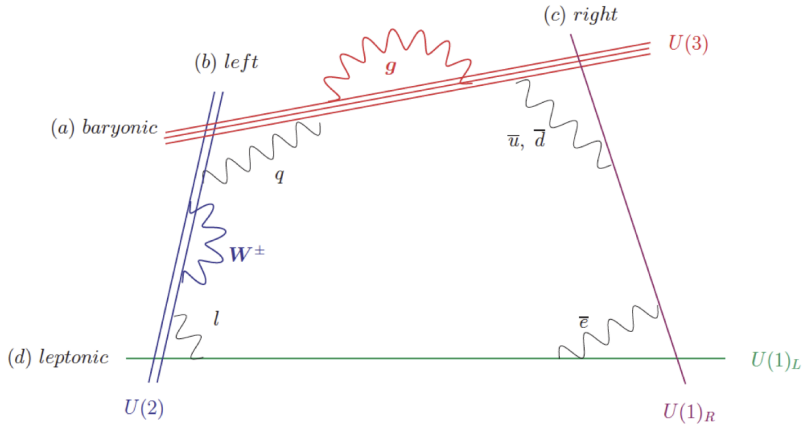


Figure 2: Bosons stretch between the layers of stacks of D-branes. Fermions have endpoints that are attached to different stacks. The closed loop is a graviton. [5]

Since we cannot detect the 6 extra spatial dimensions predicted by string theory, they must be compactified; unlike the 3 dimensions we are used to, these dimensions are *finite*. The D-brane model states that the undiscovered boson that mediates gravity, the so-called graviton, is a manifestation of a closed string that can propagate through all 9 spatial dimensions, completely untethered. Meanwhile, the other bosons are *open* strings that stretch *between* D-branes, restricted in their movement by the Dirichlet boundary condition that D-branes are named after. Therefore gravity might seem fundamentally weaker than the other forces due to its effects 'leaking' into the compactified spatial dimensions that cannot be seen on the macroscopic scale.

In Figure 2, the open strings are gauge bosons whose ends are attached to the D3-brane, and the closed string is a graviton propagating in the  $d_\perp$  direction.

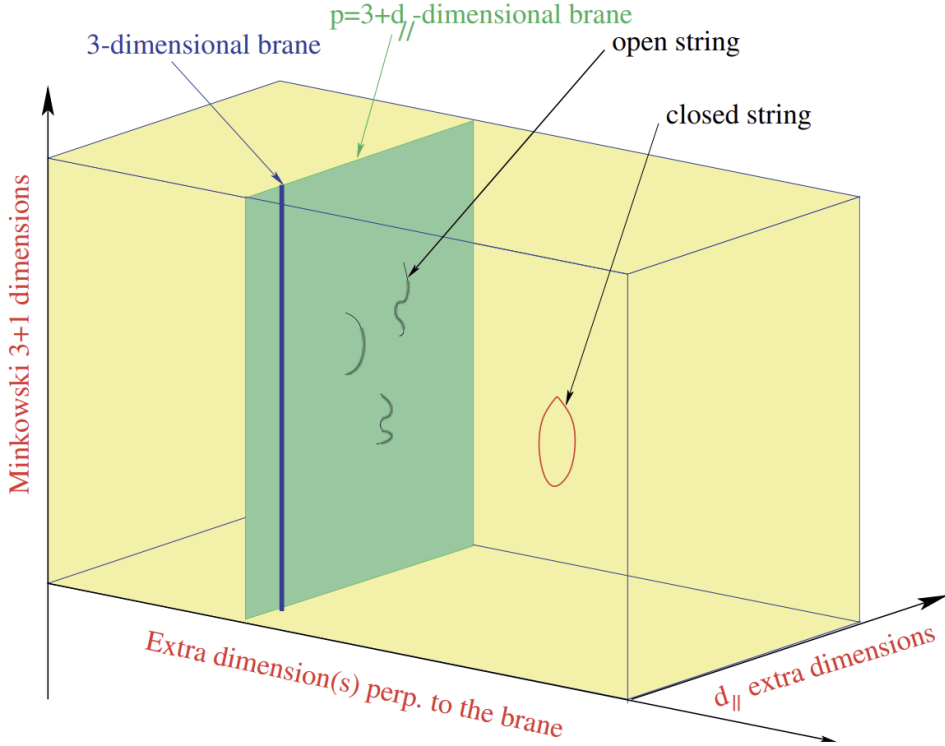


Figure 3: D-brane model diagram [4]

### 2.3 Extra Dimensions and Compactification

Since the (4-dimensional) Planck scale has been experimentally measured, we are free to use this in calculations. If we imagine a simple geometric compactification where all 6 compacted dimensions are of radius  $R$ , and the volume of the compactified dimensions is given by  $V_6 = (2\pi R)^6$ , then the effective four-dimensional Planck scale  $M_{Pl4}^2$  is related to the ten-dimensional Planck scale  $M_{Pl10}$  by [4]:

$$M_{Pl4}^2 \sim M_{Pl10}^8 R^6 \quad (1)$$

This is the simplest possible compactification of extra dimensions. We imagine a scenario where every possible point in our familiar 4D-spacetime has 6 more spatial dimensions wrapped around them. These dimensions are not like the ones that we know; they are finite. Unlike the way I can move infinitely far along the  $x$ ,  $y$ , and  $z$  axes, I cannot do the same in the other six spatial dimensions. Eventually, I would end up back where I started.

This phenomenon can be understood qualitatively. Refer to the figure below:

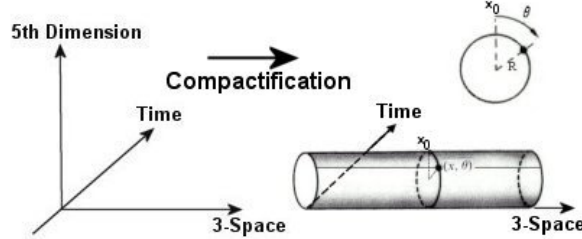


Figure 4: 5-dimensional spacetime with 1 compactified spatial dimension of radius  $R$  [16].

In this picture, 3D space extends infinitely across the page, and time moves into the page. Any object is free to move infinitely far away from the origin in 3-space, but to move through the 5th dimension amounts to traversing across the curved surface of the cylindrical worldvolume, such that an object that moves in this way would eventually return to the same point on the cylinder, completing the definition of compactedness.

An observer may traverse the fifth dimension at any point along the 3-space. For every point in 3D space, there exists a curled-up 5th dimension of radius  $R$  that can almost be considered a 1D line. If we extend the 3D space outward, the fifth dimension becomes continuous; that is, the 1D lines combine to form the 2D curved surface of a cylinder. In other words, an observer may move through 3-space while moving through the 5th dimension. This would appear to be a sort of helical path around the curved surface of the worldvolume.

We imagine that all 6 extra dimensions have an effective radius  $R$ , a distance through which I would have to move in order to return to the original point, just as above; we imagine that all six extra dimensions have the same  $R$ . Consider all of 3D space with a 3D coordinate system, where the distance between adjacent points is the Plank length  $l_p$ :

$$l_p = \sqrt{\frac{\hbar G}{c^3}} \quad (2)$$

Around each of these points in 3D space exist 6 compactified dimensions curled around them. Setting  $M_{Pl10}$  to the electroweak scale  $m_{EW}$  to remedy the Hierarchy problem, and set  $M_{Pl4}$  to the observed  $10^{15}$  TeV. This gives  $R \sim 10^5$  TeV $^{-1}$  [3].

The 4D Planck scale may be related to the volume of the extra dimensions  $V_6$  by [5];

$$M_{Pl4}^2 = \frac{8}{g_s^2} M_s^8 \frac{V_6}{(2\pi)^6} = \frac{8}{g_s^2} M_s^8 R^6 \quad (3)$$

where  $g_s$  is the dimensionless string coupling. Plugging in the previously derived  $R \sim 10^5$  TeV $^{-1}$  as well as  $M_{Pl4} \sim 10^{15}$  TeV and solving for  $M_s$  gives  $M_s \sim g_s^{\frac{1}{4}}$  TeV. This means that if our current approximations are correct, then the fundamental string scale, where string effects become pertinent, is on the order of a few TeV. This energy can currently be reached using the LHC at CERN.

### 3 Proton Collisions at the LHC

#### 3.1 Proton Collision Kinematics

In proton collisions discussed in this paper, collisions take place along the horizontal beam ( $z$ ) axis. In this section, we consider the center-of-mass frame, where the total momentum of the system is zero. Consider two protons approaching each other along the beam axis and then scattering at an angle  $\theta$  from the axis [4]:

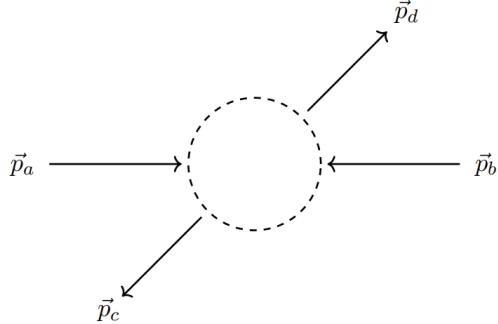


Figure 5:  $pp$  collision diagram

If the momentum transfer between  $p_a$  and  $p_b$  is minimal, the interaction is classified as a *soft* collision; if it is large, it is said to be *hard*. To perform calculations, we define the Lorentz invariant Mandelstam variables, which, as the name suggests, are invariant under Lorentz boosts along the beam axis:

$$s = (p_a + p_b)^2 = (p_c + p_d)^2 \quad t = (p_a - p_c)^2 = (p_b - p_d)^2 \quad u = (p_a - p_d)^2 = (p_b - p_c)^2 \quad (4)$$

where  $p_i$  denotes a proton's four-vector  $(E, p_x, p_y, p_z)$ . At TeV-order energy scales, we can neglect mass and consider only the energy that comes from momentum, so the initial protons' four-vectors can be written as the following:

$$p_a = \left(\frac{s}{2}, 0, 0, \frac{s}{2}\right), \quad p_b = \left(\frac{s}{2}, 0, 0, -\frac{s}{2}\right) \quad (5)$$

#### 3.2 Diparton to Parton-Photon Interactions

When protons collide, partons within them interact and often give rise to new particles. In this paper, we focus on  $gg \rightarrow g\gamma$  and  $gq \rightarrow q\gamma$  subprocesses. Quarks and gluons, the main components of protons, collide when the protons that they are a part of smash together along the beam axis. Each parton, whether it be a  $g$  or a  $q$ , carries a fraction  $x$  of its parent proton's momentum  $p$ . We define  $k_1$  and  $k_2$ , the 4-momentum of the incident partons:

$$x_1 = \frac{|\vec{k}_1|}{|p_1|} \quad x_2 = \frac{|\vec{k}_2|}{|p_2|} \quad (6)$$

To describe these subprocesses, we define new Mandelstam variables

$$\hat{s} = (k_1 + k_2)^2 = (k_3 + k_4)^2 \quad \hat{t} = (k_1 - k_4)^2 = (k_2 - k_4)^2 \quad \hat{u} = (k_1 - k_3)^2 = (k_2 - k_3)^2 \quad (7)$$

according to the diagram

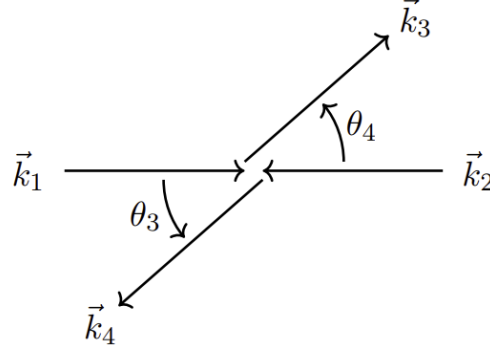


Figure 6: Parton-scattering diagram with 4-vectors

As with the protons, energy scales are sufficiently high that energy contributions due to mass can be neglected. Therefore the invariant mass of the parton scattering event is

$$M = \sqrt{\hat{s}} \quad (8)$$

The transverse momentum  $p_\perp$  of an outgoing parton is Lorentz invariant and can be written the following way:

$$k_\perp = \sqrt{k_x^2 + k_y^2} \quad (9)$$

The rapidity of an outgoing parton, a quantity related to the angle that the path makes with the beam axis, is also Lorentz invariant. Two particles with the same rapidities remain at the same angular separation throughout the event and after [6].

$$y = \frac{1}{2} \ln \frac{E + p_z}{E - p_z} \quad (10)$$

In the case of massless particles (such as gluons and photons), we may express  $y$  in terms of  $\theta$ , the angle with the beam axis:

$$y = \frac{1}{2} \ln \frac{1 + \cos \theta}{1 - \cos \theta} = -\ln \tan \frac{\theta}{2} = \eta \quad (11)$$

where  $\eta$  is psuedorapidity. If a particle moves along the beam axis after the collision, it is said to have an infinite rapidity. If the parton ricochets at a right angle, the rapidity is zero.

It is handy to define parameters  $y$  and  $Y$  here to helps define the relationship between  $y$  and  $M$  of the collision:

$$y = \frac{1}{2}(y_3 - y_4) \quad Y = \frac{1}{2}(y_3 + y_4) \quad p_\perp = \frac{M}{2 \cosh y} \quad (12)$$

Outgoing partons have energies

$$E = p_\perp \cosh y \quad (13)$$

and three momenta

$$k_x = p_\perp \cos \theta \quad k_y = p_\perp \sin \theta \quad k_z = p_\perp \sinh \theta \quad (14)$$

### 3.3 Parton Distribution Functions

Inside a proton, partons are constantly exchanging momentum with each other on the quantum level, and the exact portion of the proton's momentum that is carried by a particular parton is inherently probabilistic. We introduce Parton Distribution Functions (PDFs) to grapple with this problem. A PDF  $f_i(x, Q^2)$  is a function that outputs the probability number density of finding a particular parton  $i$  with a particular momentum fraction  $x$  at the energy scale of the collision  $Q$  [7]. Here,  $Q = M = \sqrt{s}$ .

PDFs must be determined experimentally. The so-called CTEQ6L1 [7] PDF set is used for ATLAS experiments. Discontinues in the distributions start to occur at  $x \sim 0.97$ . This is the PDF set that will be used for the work in this paper.

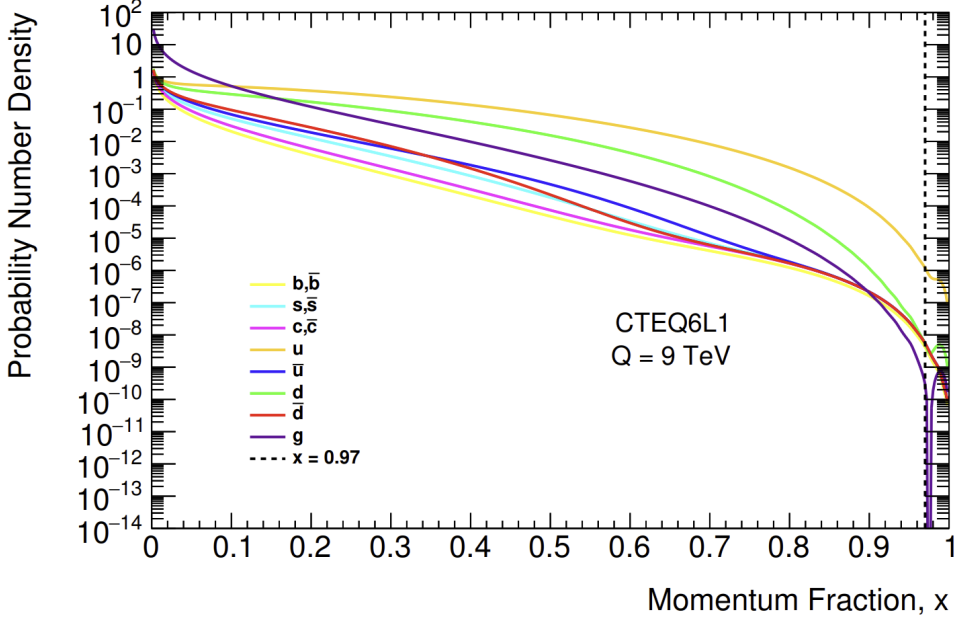


Figure 7: CTEQ6L1 PDFs at  $Q = 9$  TeV [7]

### 3.4 Scattering Amplitudes and cross-sections

In  $pp$  collisions, several different types of interactions may occur; in some instances, the incoming partons may exchange a virtual particle. We are interested in the case of two partons colliding directly and forming a string resonance in what is dubbed as the  $s$ -channel, and decaying into two more outgoing partons. The probability of a certain interaction taking place is called its 'cross-section,' similar to an area that we are trying to hit with the proton beam. The cross-section is measured in units of barns (1 barn =  $10^{-28} \text{ m}^2$ ).

To calculate the cross-section of an event, the scattering amplitude (sometimes called a 'probability amplitude')  $\mathcal{M}$  must be calculated, which depends on the energies of the involved partons. The cross-section of an event itself is a function of  $\mathcal{M}$  and the different states the involved particles may assume. Consider two incident partons with three-momenta  $k_1$  and  $k_2$  which carry positive helicities (their spin is oriented in the same direction as their momenta) and correspond to the  $U(N)$  generators  $T^{a_1}$  and  $T^{a_2}$ . Conversely,  $k_3$  and  $k_4$  carry negative helicities and correspond to the  $T^{a_3}$  and  $T^{a_4}$  generators.

Of all the ways that partons can possibly interact, most of them can be ignored when considering the amplitude because their contributions to the total amplitude are negligible [4]. We need only concern ourselves with the so-called 'tree level diagrams' shown below [11].

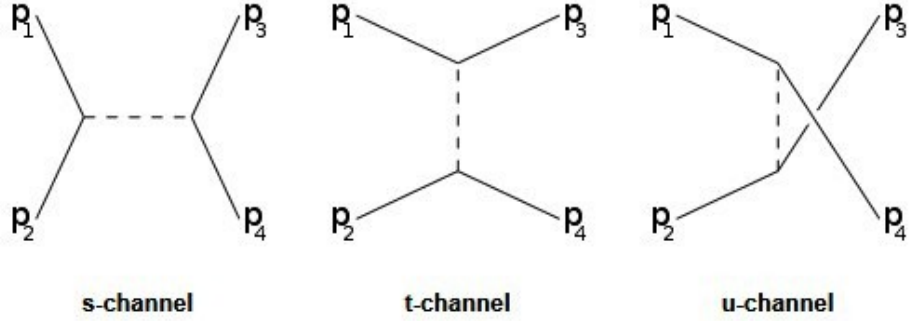


Figure 8:  $s$ ,  $t$ , and  $u$  channel tree-level diagrams. The dashed line represents a virtual interaction particle  $\xi$  and is called a bosonic line.

Each point where lines meet is called a vertex, where all quantities such as color, spin, and energy must be conserved. We include special factors called propagators for each internal line

$$\frac{1}{\xi^2 - m^2} \quad (15)$$

where  $m$  is the mass of the virtual particle. To conserve momentum in an  $s$ -channel process, we add delta functions at each vertex [4]:

$$\delta^4(k_1 + k_2 - \xi) \quad \delta^4(\xi - k_3 - k_4) \quad (16)$$

We integrate over the internal momenta of the interaction and notice that the delta functions cancel because of conservation. This implies that  $\xi = k_1 + k_2 = k_3 + k_4 = \hat{s}$ . We must also include the strong coupling  $g$ . For an  $s$ -channel interaction, we arrive at

$$\mathcal{M} \sim \frac{g^2}{\xi^2 - m^2} \sim \frac{g^2}{(k_1 + k_2)^2 - m^2} \quad (17)$$

For a  $t$ -channel interaction, the delta functions are

$$\delta^4(k_1 - k_3 - \xi) \quad \delta^4(\xi + k_2 - k_4) \quad (18)$$

which implies  $\xi = k_1 - k_3 = \hat{t}$ . Following the same math that we did for the  $s$  channel, we arrive at

$$\mathcal{M}_{\hat{s}} = \frac{g^2}{\hat{s}^2 - M^2} \quad \mathcal{M}_{\hat{t}} = \frac{g^2}{\hat{t}^2 - M^2} \quad \mathcal{M}_{\hat{u}} = \frac{g^2}{\hat{u}^2 - M^2} \quad (19)$$

the so-called tree-level process string amplitudes. Interactions with intermediate interactions, as mentioned before, are ignored. As can be seen, none of the above amplitudes represent smooth functions and are undefined at certain points called poles (for example,  $\mathcal{M}_{\hat{s}}$  u.d at  $M = \hat{s}$ ). As  $\hat{s} \rightarrow M$ , the amplitude gets increasingly large, a phenomenon tied to Regge Theory [12]. A Regge state is a sort of transitional state that is created in the  $s$  channel during two-parton scattering. These states tend to occur at energies that correspond to the pole  $\hat{s}$ , which in QCD, leads to resonance production when *the collision mass approaches the string scale  $M_s$* .

Collision data is generated with STRINGS MC event generator in which string resonances form at  $M = M_s$ . Such resonances are excitations in the  $s$ -channel and represent a vector boson mediating the interaction. If the resonances produced by STRINGS match those observed at the LHC, then particle physicists may have reason to believe that string theory is a successful model. Furthermore, the boson mediating the interaction could be a new, exotic boson, such as the graviton or a quantum black hole.

We consider only parton-parton to photon-parton interactions, which are described in the STRINGS MC event generator code [1]:

$$|\mathcal{M}(gg \rightarrow g\gamma)|^2 = \frac{5g^4 Q^2}{3M_s^4} \left[ \frac{M_s^8}{(\hat{s} - M_s^2)^2 + (M_s \Gamma_{g^*}^{J=0})^2} + \frac{\hat{t}^4 + \hat{u}^4}{(\hat{s} - M_s^2)^2 + (M_s \Gamma_{g^*}^{J=2})^2} \right] \quad (20)$$

$$|\mathcal{M}(gq \rightarrow q\gamma)|^2 = \frac{-g^4 Q^2}{3M_s^2} \left[ \frac{\hat{u} M_s^4}{(\hat{s} - M_s^2)^2 + (M_s \Gamma_{q^*}^{J=\frac{1}{2}})^2} + \frac{\hat{u}^3}{(\hat{s} - M_s^2)^2 + (M_s \Gamma_{q^*}^{J=\frac{3}{2}})^2} \right] \quad (21)$$

$M_s$  is the string scale, the Mandelstam variables are  $\hat{s}, \hat{u}$ .  $g_s$  is the string coupling [11],

$$g_s = \sqrt{4\pi\alpha_s} \quad \frac{1}{\alpha_s(M_s)} = \frac{1}{\alpha_s(M_Z)} - \frac{7}{2\pi} \ln \frac{M_s}{M_Z} \quad (22)$$

where  $M_Z = 92.1$  GeV and  $\alpha(M_Z) = 0.118$ . Here,  $\alpha_s$  is a constant called the strong coupling, or the running coupling, that communicates the strength of the electroweak scale at a particular energy level  $M_s$ . From [4], we have the resonance widths:

$$\Gamma_{g^*}^{J=0} = \frac{g^2}{4\pi} M_s \frac{3}{4} \quad \Gamma_{g^*}^{J=2} = \frac{g^2}{4\pi} M_s \frac{9}{20} \quad \Gamma_{q^*}^{J=\frac{1}{2}} = \frac{g^2}{4\pi} M_s \frac{3}{8} \quad \Gamma_{q^*}^{J=\frac{3}{2}} = \frac{g^2}{4\pi} M_s \frac{3}{16} \quad (23)$$

The factor  $Q$  is given by [9]:

$$Q^2 = \frac{1}{6} \kappa^2 \cos^2 \theta_W \quad (24)$$

Where the so-called mixing factor  $\kappa = 0.14$  and  $\theta_W$  is the fundamental Weinberg angle, related to the electroweak force [9].

### 3.5 Differential Cross-sections

The cross-section is usually described by the number of particles that scatter in some angular region of space. The differential cross-section is then the rate at which particles are scattered in a particular direction through an angular surface  $\Omega$ . The number of particles moving through the area  $d\sigma$  is  $dN = Ld\sigma$ , where  $L$  is the luminosity (particle flow-density; the number of particles moving through an area). This is also the number of particles moving through  $d\Omega$ . We can say that the cross-section multiplied by the luminosity is the event rate [8]. We may write

$$\frac{d\sigma}{d\Omega} = \frac{d\sigma}{|\sin \theta d\theta d\phi|} = \frac{|\mathcal{M}(12 \rightarrow 34)|^2}{64\pi^2 \hat{s}} \quad (25)$$

where  $\mathcal{M}$  is the scattering amplitude of the interaction (21 & 22). Scattering amplitudes depend on the energy scale and the particles involved.

We consider only tree-level partonic processes predicted by QCD, known as  $s$ -channel,  $t$ -channel, and  $u$ -channel interactions. Spins, colors, and particle flavors can vary in these processes, and we must include factors to account for this. Each particle has a spinor that represents its spin; a spinor is a vector with four entries that inform us of the quantum state of the particle: we must take the inner product of all the initial and final particle spinors for all possible permutations. We must also include the so-called 'color factor,' which is the trace of the product of all the spinor *matrices* that represent possible gluon color combinations (gluons can assume more than one color at once, so they do not have vector spinors, but matrix spinors).

We average over initial spin, color, and flavor combinations and sum over final spin, color, and flavor combinations by convoluting the partonic cross-section with the PDFs of the initial partons. In

the center-of-mass frame,  $\theta_3 = \theta_4$ , so then  $y_3 = -y_4$ ; recall that  $y_i$  denotes rapidity/pseudorapidity (refer to Fig 4). It's convenient to introduce the parameters  $y$  and  $Y$

$$y_3 = Y + y \quad y_4 = Y - y \quad \Rightarrow \quad y = \frac{1}{2}(y_3 - y_4) \quad Y = \frac{1}{2}(y_3 + y_4) \quad (26)$$

and  $\tau$

$$\tau = \frac{M}{s} = \frac{\sqrt{\hat{s}}}{s} \quad (27)$$

In terms of these new variables, we can write the momentum fractions of the incoming partons

$$x_a = \sqrt{\tau} e^Y \quad x_b = \sqrt{\tau} e^{-Y} \quad (28)$$

and the Mandelstam variables can be written as

$$\hat{s} = M^2 \quad \hat{t} = -\frac{M^2}{2} \frac{e^{-y}}{\cosh y} \quad \hat{u} = -\frac{M^2}{2} \frac{e^y}{\cosh y} \quad (29)$$

Referring to (20), we must set boundaries of integration:

$$|y_3|, |y_4| < y_{max} \quad x_1, x_2 < 1 \quad \Rightarrow \quad Y_{max} = \min \left[ \ln \frac{1}{\sqrt{\tau}}, y_{max} \right] \quad (30)$$

The differential cross-section for  $pp \rightarrow \gamma + \text{jet}$  interactions with respect to  $M$  is shown in [9]:

$$\frac{d\sigma}{dM} = M\tau \sum_{ijk} \left( \int_{-Y_{max}}^{Y_{max}} dY f_i(x_a, M) f_j(x_b, M) \int_{-y_{max}+|Y|}^{y_{max}-|Y|} dy \frac{|\mathcal{M}(12 \rightarrow 34)|^2}{16\pi\hat{s}^2} \frac{1}{\cosh^2 y} \right) \quad (31)$$

### 3.6 Jets

Jets are cone-shaped streams of particles that occur in high energy  $pp$  collisions. Consider the subprocess of interest  $gg \rightarrow g\gamma$  which results in a singular  $g$ . Gluons possess a color charge and are usually found with other gluons that possess different color charges to produce protons. Nature abhors a gluon that exists alone with a color charge, and as such, it is energetically favorable for another gluon to appear from a vacuum to restore a colorless state. A chain reaction ensues in which a gluon that appears also forces another gluon to appear, and so on. The result is a jet.

The properties of jets can help to understand the interactions that caused them. In particular, the invariant mass of the produced jet events, or all the partons that comprise it, can help us predict what virtual particle  $\xi$  may have played a part, and if this particle is novel. The invariant mass of the jet event is how we will pinpoint this detail, along with some other kinematic data that will be introduced in a later section.

## 4 STRINGS Monte Carlo Event Generator

### 4.1 Overview

Figure 9 is a screenshot of a header from a single run of STRINGS:

The user may specify all the necessary parameters for simulating collisions: 'COME' and 'Ms' are the center-of-mass-energy and the string scale, respectively. When integrating (27) to get the total cross-section, a region of integration may be chosen such that 'MinMass' and 'MaxMass' are the lower and upper bounds. The maximum rapidity 'yMax' may also be chosen, along with the number of collisions to simulate. The strong coupling is set to the default value (-1 tells the program to use the

```

#####
# Run parameters#####
#RandGenSEED=1234567      # Random numbers seed.
RandGenSEED=$(shuf -i 1-10000000 -n 1.) ##### Random number se
COMe=13600                 # Centre of mass energy [GeV].
Ms=7000                     # String scale [GeV].
MinMass=6080                # Minimum invariant mass [GeV].
MaxMass=13600                # Maximum invariant mass [GeV].
yMax=2.5                   # Maximum |y|.
Number=11000                # Number of events to generated.
PDFSet=cteq6l1               # PDF set.
Coupling=-1                  # Strong coupling constant ( $g^2/4\pi$ ).
CouplingScale=$Ms            # Running coupling scale.
PDFScale=$Ms                 # PDF scale.

#####
# Subprocesses #####
gg2gg=false                 # gg -> gg          (ID = 1)
gg2qbar=false                # gg -> qbar        (ID = 2)
gg2q=false                  # gg -> qg          (ID = 3)
ggbar2qbar=false             # gqbar -> gqbar    (ID = 4)
qqbar2gg=false                # gqbar -> gg        (ID = 5)
gg2Gamma=true                # gg -> gGamma      (ID = 6)
gg2qGamma=true               # gg -> qGamma      (ID = 7)
gg2GammaGamma=false           # gg -> GammaGamma  (ID = 8)
qqbar2GammaGamma=false        # qbar -> GammaGamma (ID = 9)
gg2ll=false                  # gg -> ll          (ID = 10)
qbar2ll=false                # qbar -> ll          (ID = 11)

#####
# Processes #####
FirstStringCoeff=true         # Include first string resonance.
SecondStringCoeff=false       # Include second string resonance.
QCDCoeff=false                # Include QCD (tree-level).

#####
# Qurak Masses #####
#dMass=5e-3      # GeV
#uMass=2e-3      # GeV
#sMass=1e-3      # GeV
#cMass=1.25      # GeV
#bMass=4.2       # GeV
#tMass=172.5     # GeV
dMass=4.7e-3      # GeV
uMass=2.2e-3      # GeV
sMass=96e-3       # GeV
cMass=1.27       # GeV
bMass=4.18       # GeV
tMass=1723.21    # GeV

```

Figure 9: STRINGS header

default value), which is described in (18). A random seed is picked for every run so that collision kinematics are randomized.

When the event generator is run, the differential cross-section is calculated in 10-GeV steps from MinMass to MaxMass. For example, the minimum and maximum are 1000 GeV and 2000 GeV, then the program will create a file `cross.txt` with 101 entries, each of which is the differential cross-section for collisions with  $M = 1000$  GeV, 1010 GeV, 1020 GeV, ... 2000 GeV.

## 4.2 Les Houches Event Files

Information on each simulated collision is saved in the corresponding LHE file.

Figure 10 shows a single entry from an LHE file produced in the generation of 10  $gg \rightarrow g\gamma$  interactions.

```

<event>
4 6 1.0 6500.0 7.905138e-03 7.567941e-02
21 -1 0 0 101 102 0.000000e+00 0.000000e+00 4.191956e+02 4.191956e+02 0.0 0.0 0.0
21 -1 0 0 103 101 0.000000e+00 0.000000e+00 -6.414450e+02 6.414450e+02 0.0 0.0 0.0
22 1 1 2 0 0 -7.792815e+01 -4.672301e+02 1.046495e+02 4.851064e+02 0.0 0.0 0.0
21 1 1 2 103 102 7.792815e+01 4.672301e+02 -3.268989e+02 5.755342e+02 0.0 0.0 0.0
#pdf 21 21 6.449163e-02 9.868384e-02 6500.0 1.061919e+00 5.436104e-01
</event>

```

Figure 10: An LHE file entry for a  $gg \rightarrow g\gamma$  interaction

In the top row, 4 indicates the number of partons involved in the interaction. 6 is the event ID, specific to this type of subprocesses. 1.0 is the weight of the event, that is, how much significance the program gives in obtaining a weighted average for the cross-section. 6500 TeV is the energy of one of the partons in the collision, which is equal to

$$\frac{\sqrt{s}}{2} = \frac{E_{cm}}{2} \quad (32)$$

$9.905138e-3$  is  $\alpha_{em}$ , and  $7.567941e-2$  is  $\alpha_s$ .  $\alpha_{em}$  is the fine structure constant which denotes the strength of the electromagnetic interaction, and  $\alpha_s$  is the strong coupling constant, which represents the strength of the strong nuclear interaction.

The next two rows represent the incoming gluons (21, 21), and the next two rows represent the outgoing photon (22) and gluon (21) respectively. -1 and +1 represent the status of the parton, whether it is incoming (-) or outgoing (+). The next two columns tell us how many mother partons each parton had. In the case of the outgoing partons, this is 2; in the incoming case, this is 0. The proceeding four columns denote the 4-momentum in the form  $(p_x, p_y, p_z, E)$ . The following column is mass, which is zero in all cases because the gluon and photon are massless. The final two are proper life and spin. The proper life is '0', and 9 means that the particles have no spin [13].

The bottom row reflects the two incoming partons (21, 21). The next two numbers denote  $x_a$  and  $x_b$ , followed by  $\frac{E_{cm}}{2}$ . The last two numbers are  $x_a f_a(x_a, Q^2)$  and  $x_b f_b(x_b, Q^2)$

## 5 STRINGS Validation

### 5.1 $\sigma$ Plots

Before we produce samples, the STRINGS MC event generator must be validated. It is important to be sure that the program is simulating  $gg \rightarrow g\gamma$  and  $gq \rightarrow q\gamma$  scattering events properly. To compare the cross-sections photon jet scatterings to dijet scatterings, we refer to [4]:

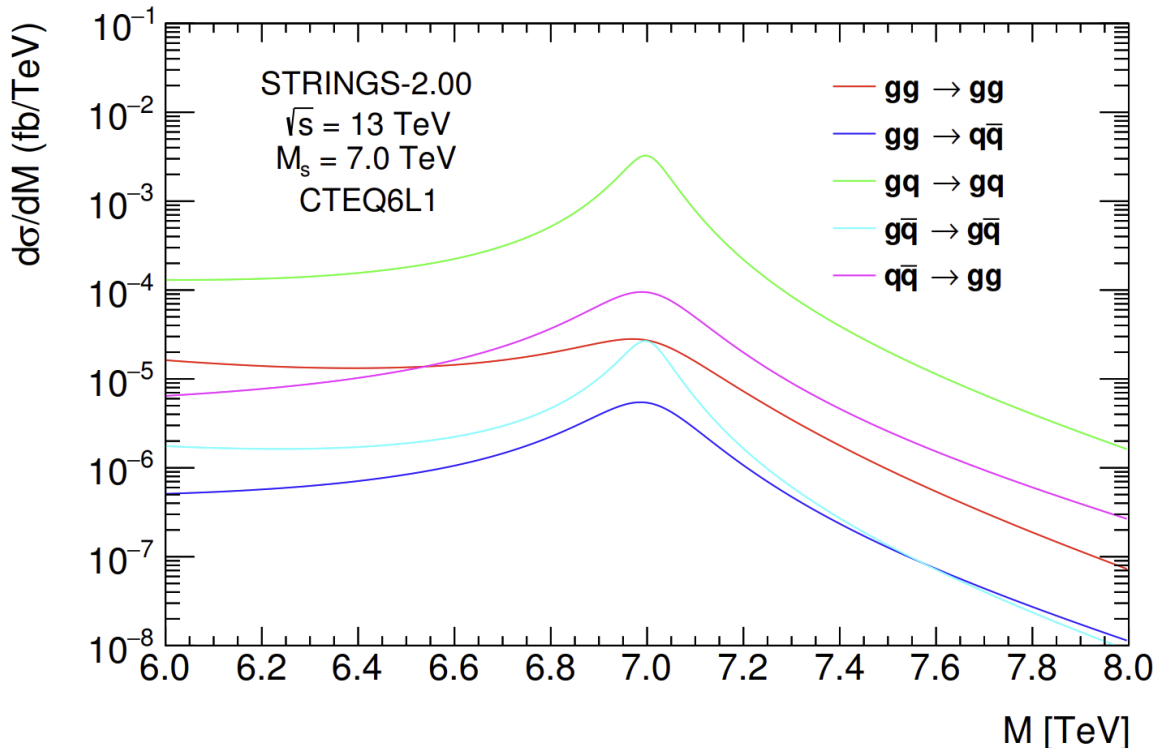


Figure 11: Differential cross-sections for dipartion (below) scattering events for  $M = [6,8]$  TeV

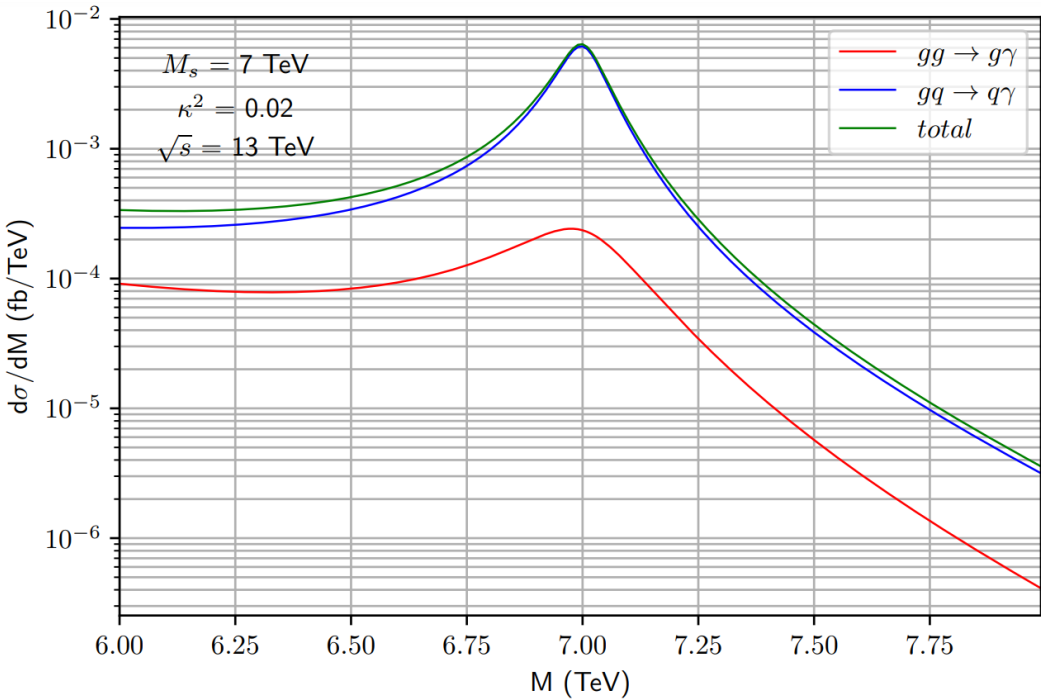


Figure 12: Differential cross-sections for single parton (above) scattering events for  $M = [6,8]$  TeV

It is observed that single parton-scattering events are greater in their differential cross-section than diparton scattering events by about an order of magnitude, which leaves more room for the discovery of string resonances.

To validate the single-parton scattering plot that we have produced, we refer to [11]:

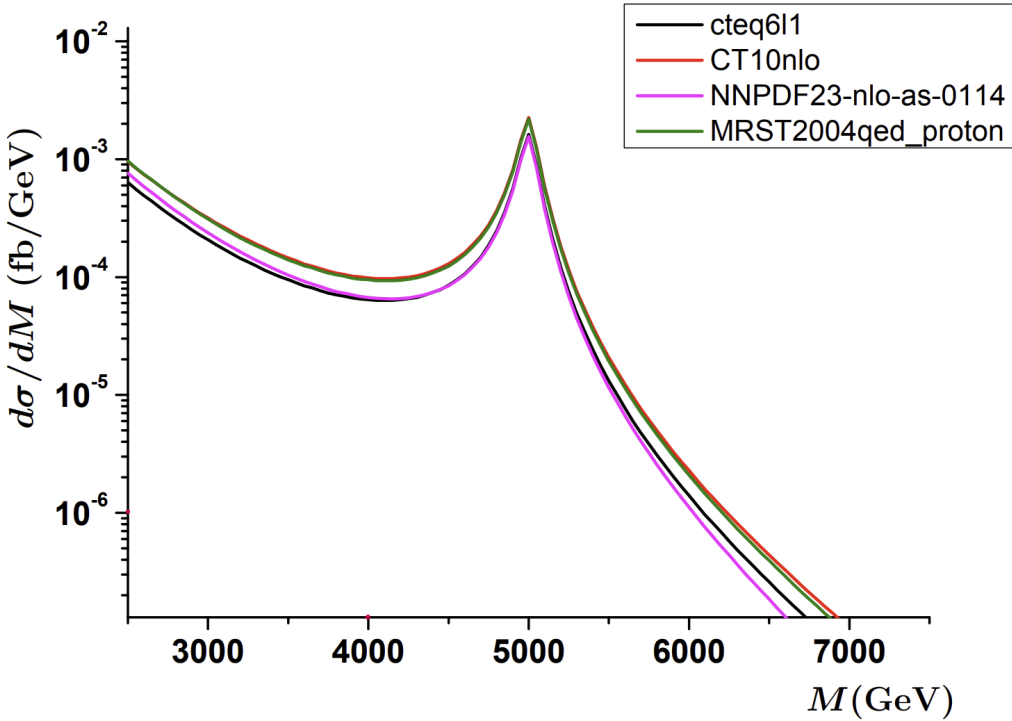


Figure 13: Differential cross-sections of single parton scattering events at  $M_s = 5$  TeV

We can recreate the above plot by running STRINGS for  $M = [2500, 6720]$  GeV at  $M_s = 5000$  GeV,  $\sqrt{s} = 14$  TeV, for  $gg$  and  $gq$  processes that lead to  $\gamma + \text{jet}$ . Several attempts were made using varying parameters. Partway through testing, a bug was located in the code that was excluding  $t$  and  $u$  channel contributions to the calculation of  $\mathcal{M}^2$ . It was also observed that in [9], a fixed coupling of 0.1 was used rather than the running coupling constant (22). Below, several of these plots are shown.

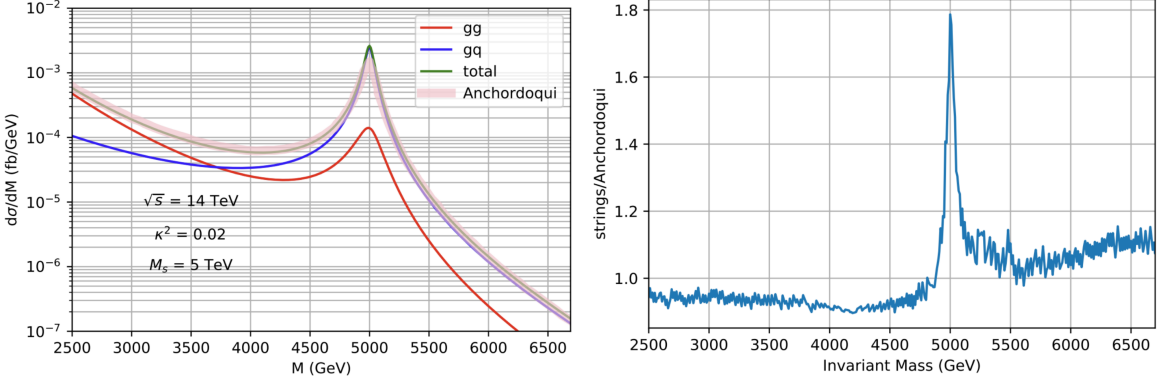


Figure 14: Differential cross-sections of single parton scattering events produced by **pre-bug-fix** STRINGS compared with [11],  $\alpha_s$  = running coupling constant.

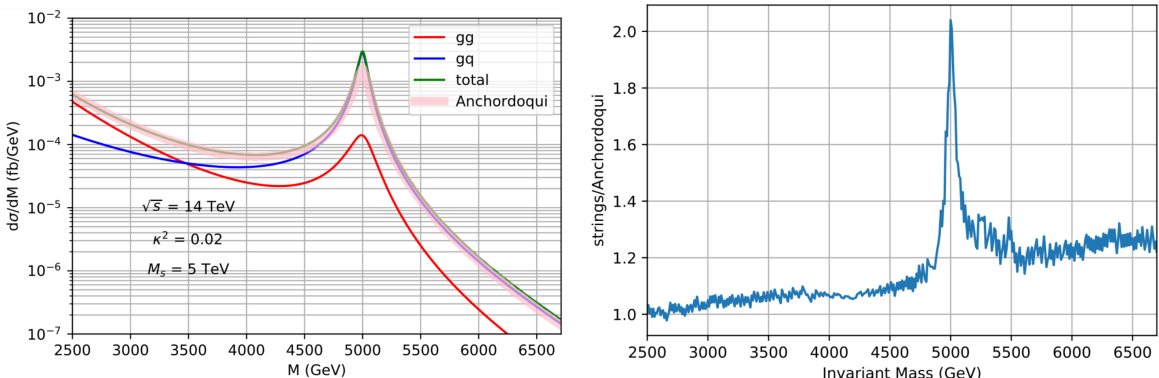


Figure 15: Differential cross-sections of single parton scattering events produced by **post-bug-fix** STRINGS compared with [11],  $\alpha_s$  = running coupling constant.

Using the running coupling constant results in a ratio plot that spikes at the peak to about a factor of 2. Predictably, adding the  $t$  and  $u$  channel contributions vertically shifted the entire curve (as can be seen in the evolution of the ratio plots). The ratio plot takes a different form when  $\alpha_s = 0.1$  is used:

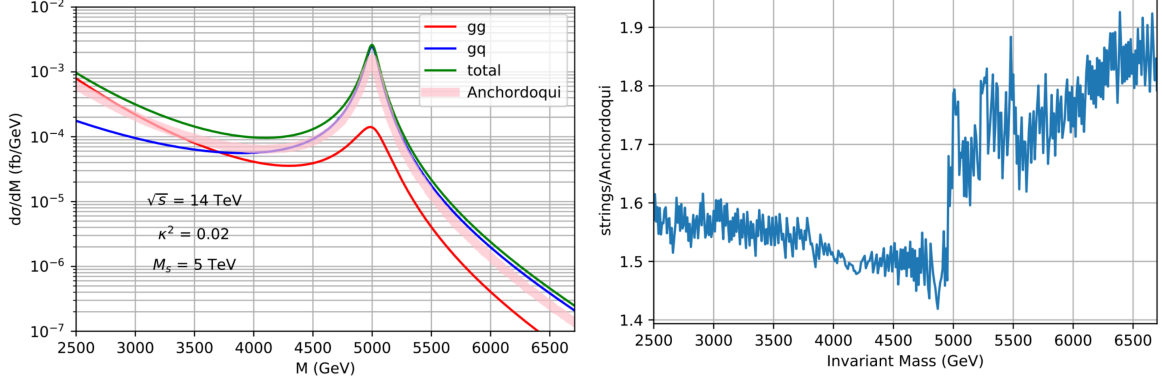


Figure 16: Differential cross-sections of single parton scattering events produced by **pre-bug-fix** STRINGS compared with [11],  $\alpha_s = 0.1$ .

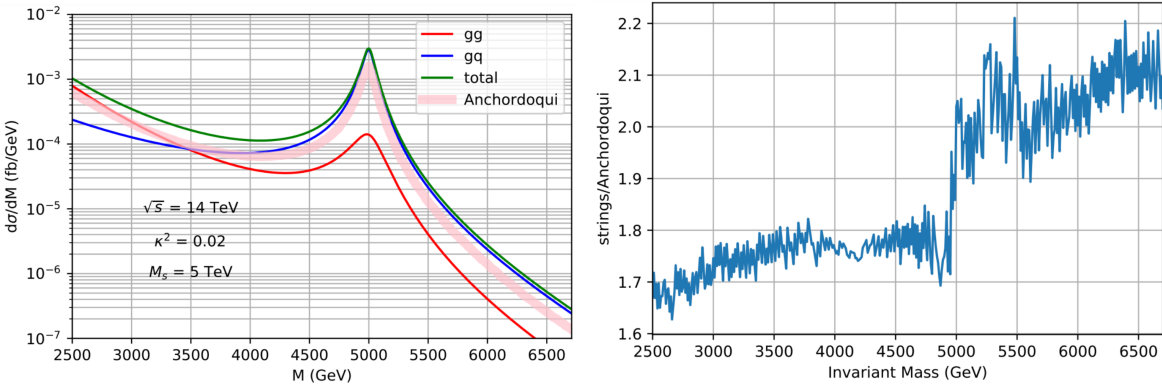


Figure 17: Differential cross-sections of single parton scattering events produced by **post-bug-fix** STRINGS compared with [11],  $\alpha_s = 0.1$ . Observe the vertical shift that occurs when the  $t$  and  $u$  channels are added.

After this further disagreement, it was discovered that in [11], the exact resonance widths described in (19) are not used in the paper; the widths are concatenated as follows:

$$\Gamma_{g^*}^{J=0} = 75 \frac{M_s}{\text{TeV}} \text{GeV} \quad \Gamma_{g^*}^{J=2} = 45 \frac{M_s}{\text{TeV}} \text{GeV} \quad \Gamma_{q^*}^{J=\frac{1}{2}} = 37 \frac{M_s}{\text{TeV}} \text{GeV} \quad \Gamma_{q^*}^{J=\frac{3}{2}} = 19 \frac{M_s}{\text{TeV}} \text{GeV} \quad (33)$$

By replacing the  $q^*$  widths in strings.py with these, the following plot is generated using the running coupling constant:

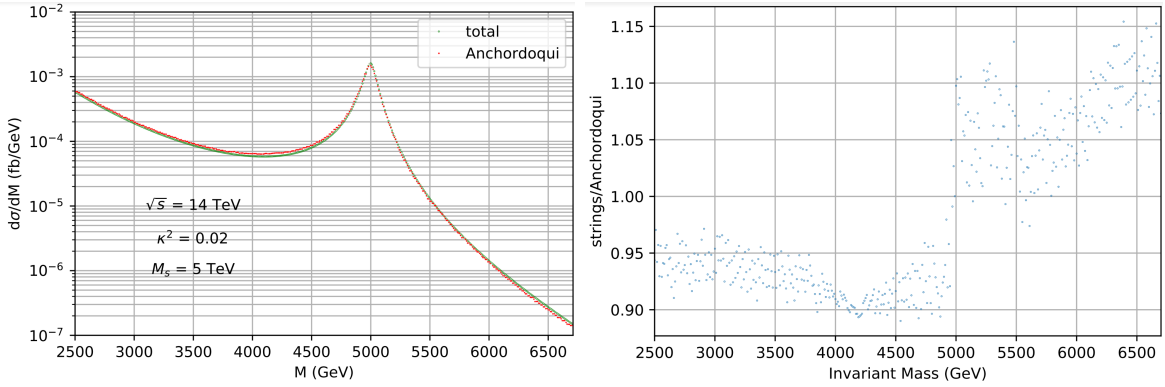


Figure 18: Differential cross-sections of single parton scattering events produced by **pre-bug-fix** STRINGS compared with [11],  $\alpha_s$  = running coupling constant, using concatenated widths.

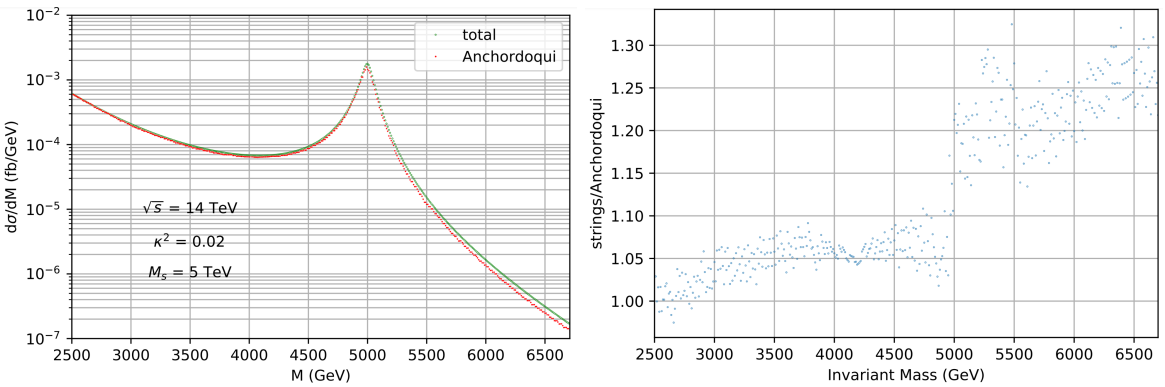


Figure 19: Differential cross-sections of single parton scattering events produced by **post-bug-fix** STRINGS compared with [11],  $\alpha_s$  = running coupling constant, using concatenated widths.

By using small dots, we can observe the reasoning for the  $\pm \sim 0.05$  fluctuations on either side of the peak: our data is smooth, but the data collected from Anchordoqui et al (pink) moves in a step-like fashion, as a result of linear interpolation of the original points. We also observe a much closer peak agreement using the concatenated widths.

To see if a better agreement may be reached, we will attempt to recreate the curve using several different  $\alpha_s$  coupling values, and then scaling by an appropriate factor to get the peaks to match. These plots are shown in Appendix 8.1.

The best results were achieved using a coupling of 0.1, and scaling the data by a factor of exactly 0.5278861221857577. On the left side of the peak, the error is about -15%, and on the right, +15%; an even spread. Going lower or above 0.1 results in the ratio plot getting 'tilted' to one side and moving up or down, depending if the coupling is increasing or decreasing. Using coupling=0.1 also demands a scale factor closer to  $\frac{1}{2}$  than all the options.

Due to the scale factor, in strings.py we divide `Msq` by  $\sim 2$  in order to adhere as closely as possible to Achordoqui et al.

## 5.2 Cross-section as a Function of $M_s$

We would also like to reproduce the results in [9], which communicates the  $gg$  cross-section for  $M_s = [1,4]$  TeV:

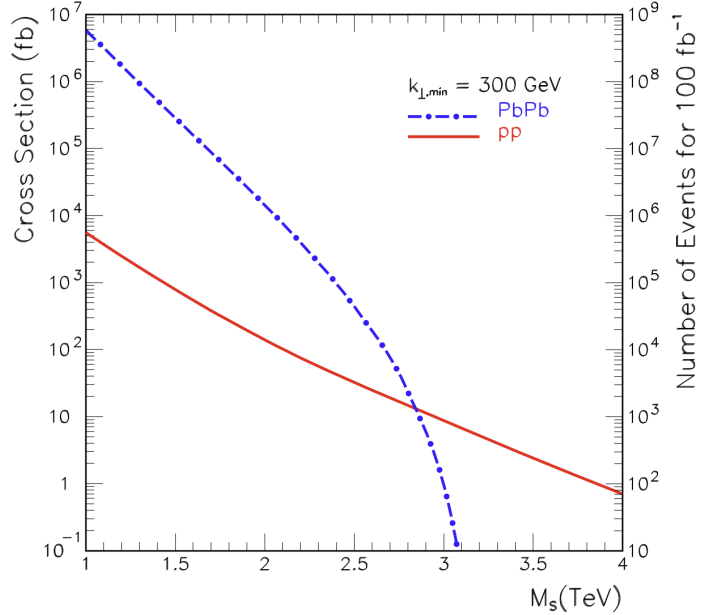


Figure 20: Cross-section vs.  $M_s$  from Anchordoqui et al

The only problem is that the region of integration is unknown. In other words, the minimum and maximum mass are not known. If  $k_{\perp,\min} = 300$  GeV, then the minimum invariant mass can be derived from the following equation:

$$k_{\perp} = \frac{M}{2 \cosh y} \quad (34)$$

This equation gives  $M_{low,cut} \sim 3334$  GeV. If we plot the cross-sections for string scales [1, 4] TeV by integrating over  $M = [3334, 14000]$  GeV, the following plot (Fig 13) is generated:

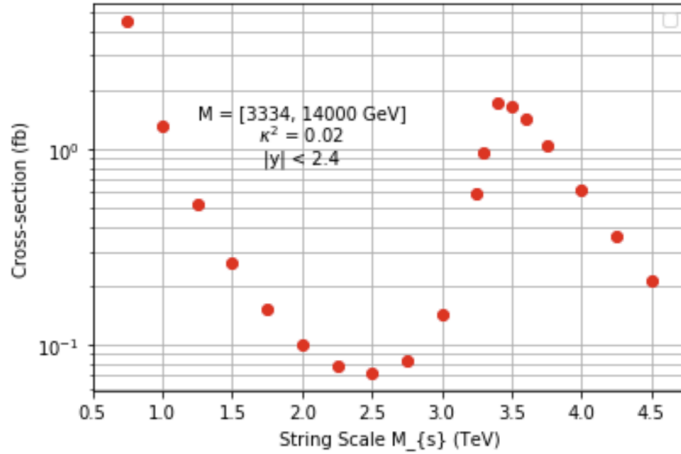


Figure 21: Cross-section of the  $gg$  subprocess (red) as a function of string scale  $M_s$  for  $M = [3334, 14000]$  GeV.

This plot is problematic because there is a spike at  $M_s = 3334$  GeV, due to the lower cut on the invariant mass also being 3334 GeV. As such, we ignore the parameter  $k_{\perp} = 300$  GeV for the time being. We plot cross-sections of string scales from 1 TeV to 14 TeV in 1-TeV-steps over an invariant mass interval of [1, 14] TeV. The following plot is generated:

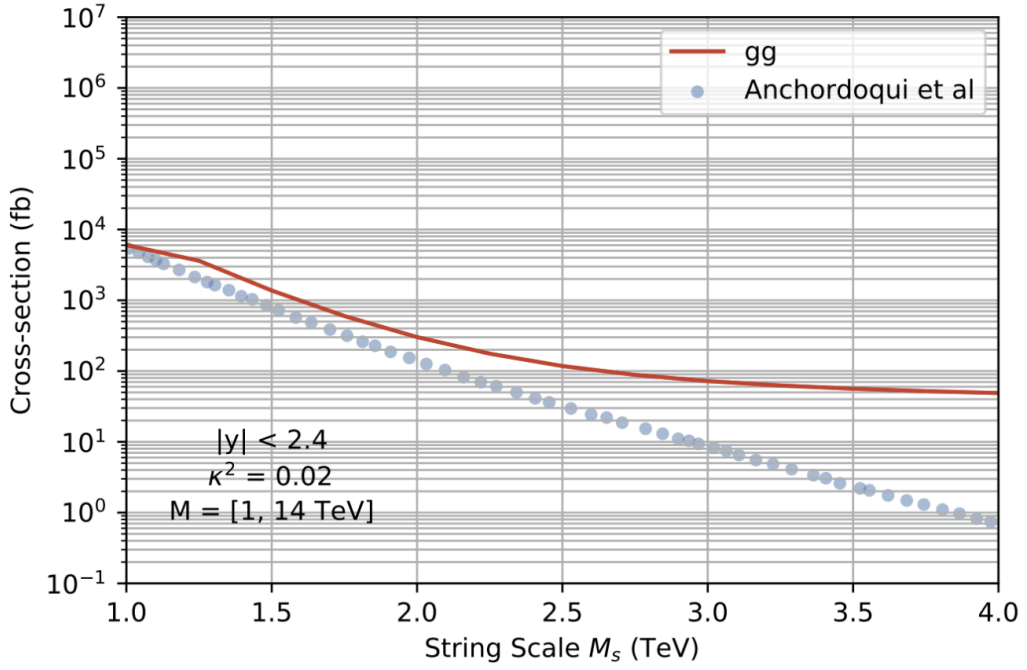


Figure 22: Cross-section of the  $gg$  subprocess (red) as a function of string scale  $M_s$ .

The plot from Fig 14 doesn't drop quickly enough; the region of integration is too large. It appears that we must choose an alternative for the invariant mass window that isn't as broad as  $[1, 14]$  TeV (see Appendix 8.2).

Using  $M = [M_{lowcut}, 14\text{TeV}]$  produces the most desirable results:

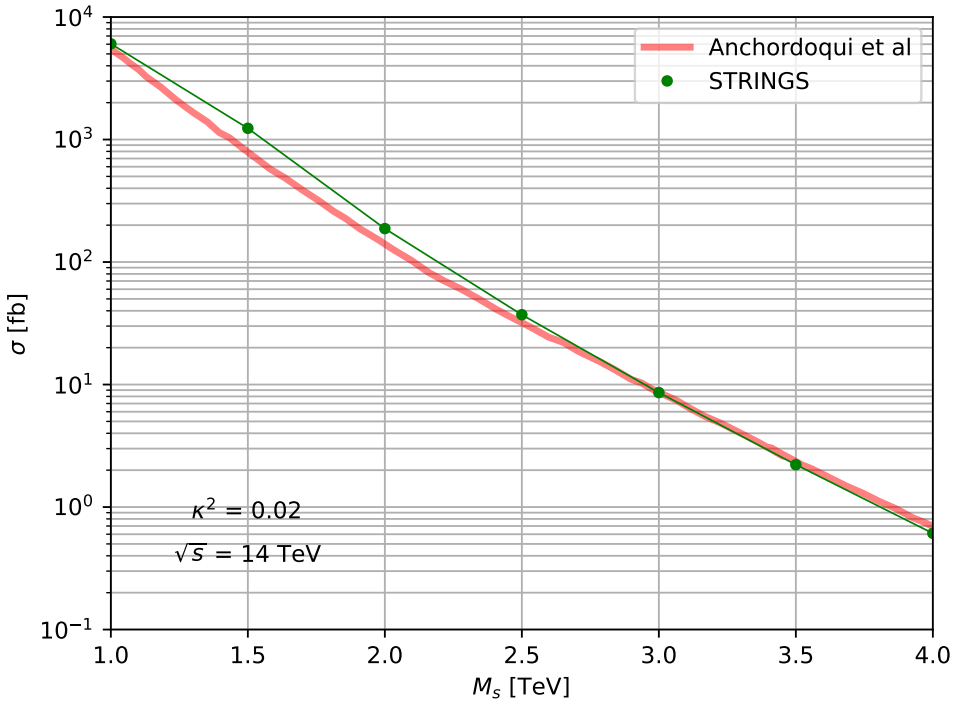


Figure 23: Total cross-section as a function of  $M_s$ ; STRINGS vs. Anchordoqui et al [11]

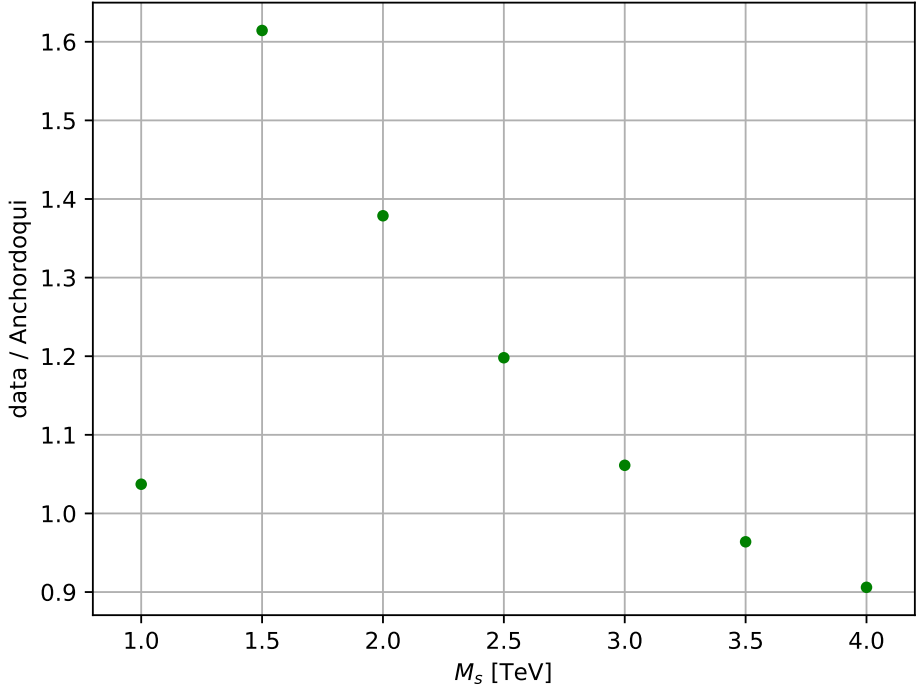


Figure 24: Ratio plot for  $M_s$  vs  $\sigma$

All of the data points fall within 20% error with the exception of  $M_s = 1.5, 2$ . However, it appears that at higher string scales, the error is poised to reach an asymptote in the low negative percentages. This is acceptable.

## 6 Analysis

### 6.1 String Scale Selection

On the order of a few TeV, it is important to make sure that our choice of string scales provides enough events for us to analyze. We begin by looking at the differential cross-sections for  $M_s = [7, 9]$  TeV (Appendix 8.3.1). For  $\sqrt{s} = 13$  TeV, and another for  $\sqrt{s} = 13.6$  TeV, separate plots will be made. The region of integration is  $M = [M_{cut}, \sqrt{s}]$

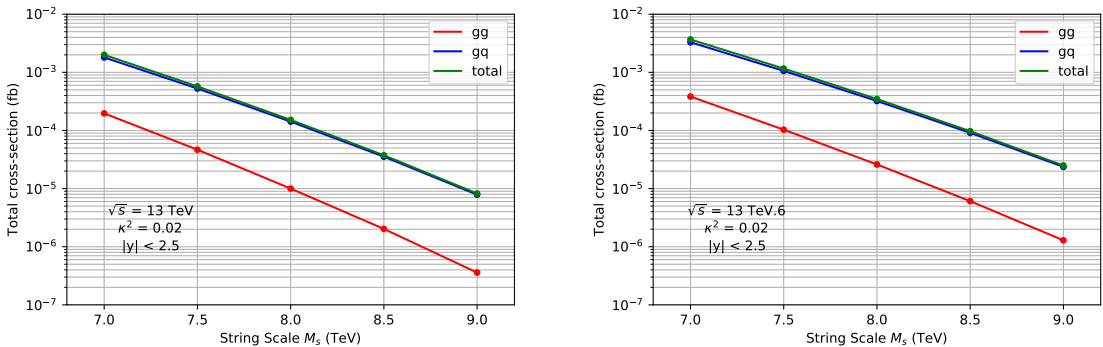


Figure 25:  $\sigma$  vs  $M_s$ ,  $M = [M_{cut}, \sqrt{s}]$

We can plot the number of events as a function of the string scale with the following formula:

$$N = 140\sigma_{13} + 115\sigma_{13.6} \quad (35)$$

where  $\sigma_i$  represents the cross-section for  $M_s = i$ .

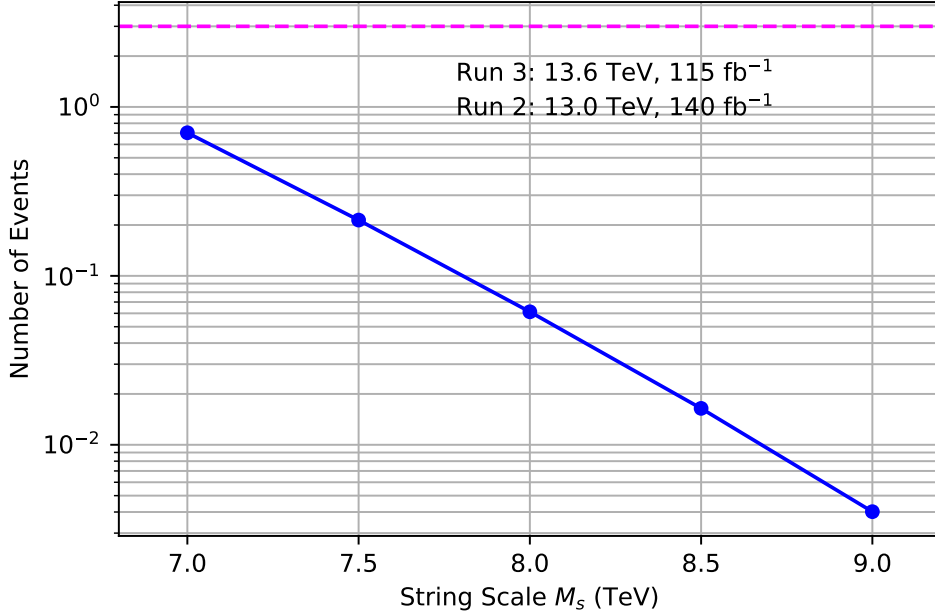


Figure 26: Number of events vs.  $M_s$ ,  $M_s = [7, 9]$  TeV

The curve is far too low on the y-axis, so more events will need to be produced. The same process but for  $M_s = [5, 7]$  TeV rather than  $[7, 9]$ , the  $\sigma$  plots for which are in Appendix 8.3.2.

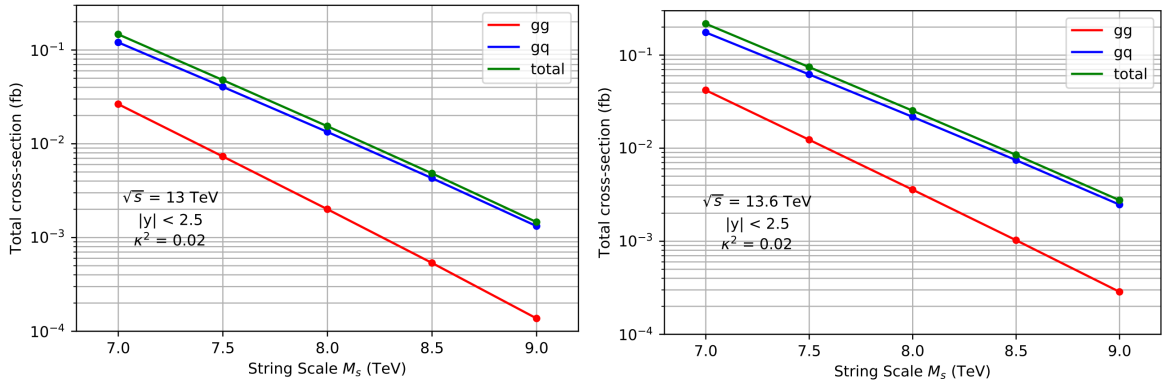


Figure 27:  $\sigma$  vs  $M_s$ ,  $M = [M_{cut}, \sqrt{s}]$

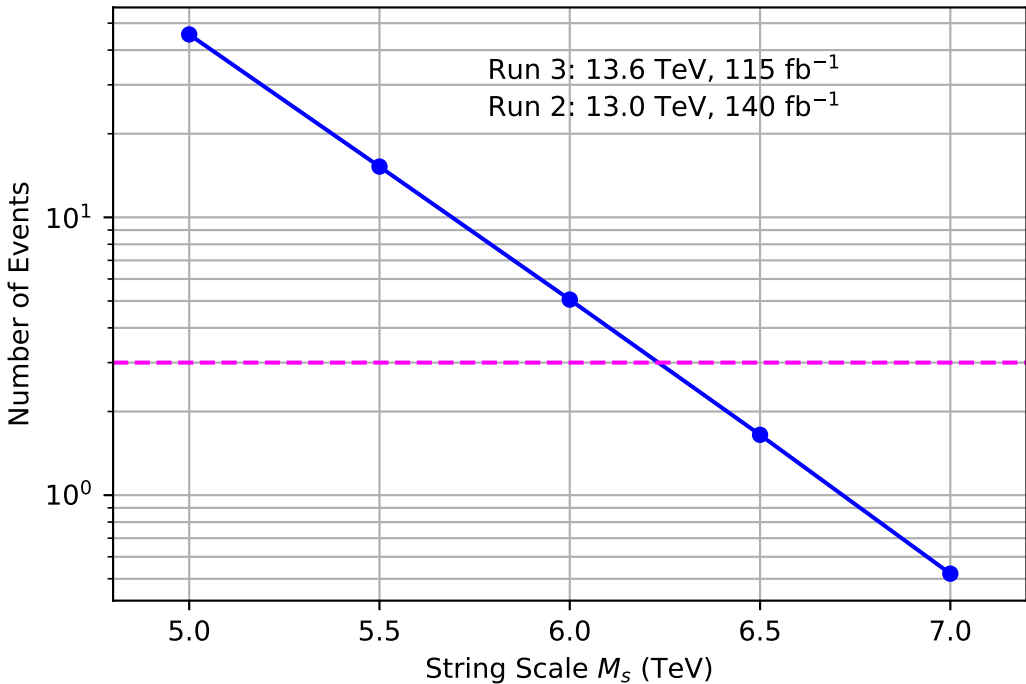


Figure 28: Number of events vs.  $M_s$ ,  $M_s = [5, 7]$  TeV. Note that 3 data points are located above  $y=3$ .

The  $M_s$  values are shown to be optimal, in line with 95% accuracy.

## 6.2 Sample Generation

For each  $M_s$  and for each  $\sqrt{s}$ , we run the generator 10 times, simulating 11000  $gg$  and  $gq$  subprocesses each time. Therefore, we will have 110,000 simulated interactions per scale per  $\sqrt{s}$ , making 1.1 million total interactions.

- mc23\_13TeV.100001.STRPy8EG\_STR\_Ms05000.evgen.TXT.e0000
- mc23\_13TeV.100002.STRPy8EG\_STR\_Ms05500.evgen.TXT.e0000
- mc23\_13TeV.100003.STRPy8EG\_STR\_Ms06000.evgen.TXT.e0000
- mc23\_13TeV.100004.STRPy8EG\_STR\_Ms06500.evgen.TXT.e0000
- mc23\_13TeV.100005.STRPy8EG\_STR\_Ms07000.evgen.TXT.e0000
- mc23\_13p6TeV.100001.STRPy8EG\_STR\_Ms05000.evgen.TXT.e0000
- mc23\_13p6TeV.100002.STRPy8EG\_STR\_Ms05500.evgen.TXT.e0000
- mc23\_13p6TeV.100003.STRPy8EG\_STR\_Ms06000.evgen.TXT.e0000
- mc23\_13p6TeV.100004.STRPy8EG\_STR\_Ms06500.evgen.TXT.e0000
- mc23\_13p6TeV.100005.STRPy8EG\_STR\_Ms07000.evgen.TXT.e0000

Each of these folders contains 10 LHE files named, for example, TXT.100005..000001.events to TXT.100005..000010.events (in the case of mc23\_13TeV.100005.STRPy8EG\_STR\_Ms07000.evgen.TXT.e0000), according to ATLAS convention.

The events generated in these MC samples are either the  $gg \rightarrow g\gamma$  subprocess or the  $gq \rightarrow q\gamma$  subprocess. At different string scales and  $\sqrt{s}$ , these portions change:

	$M_s = 5 \text{ TeV}$	$M_s = 5.5 \text{ TeV}$	$M_s = 6 \text{ TeV}$	$M_s = 6.5 \text{ TeV}$	$M_s = 7 \text{ TeV}$
$gg \rightarrow g\gamma$	18.010%	15.310%	13.028%	11.737%	9.3811%
$gq \rightarrow q\gamma$	81.990%	84.680%	86.972%	88.263%	90.618%

Table 1: Event fractions for  $\sqrt{s} = 13 \text{ TeV}$

	$M_s = 5 \text{ TeV}$	$M_s = 5.5 \text{ TeV}$	$M_s = 6 \text{ TeV}$	$M_s = 6.5 \text{ TeV}$	$M_s = 7 \text{ TeV}$
$gg \rightarrow g\gamma$	19.319%	16.564%	14.172%	12.128%	10.367%
$gq \rightarrow q\gamma$	80.681%	83.436%	85.828%	87.872%	89.633%

Table 2: Event fractions for  $\sqrt{s} = 13.6 \text{ TeV}$

### 6.2.1 Validity of Samples

Since two processes are being studied, in a single run of STRINGS both types of interactions will be generated. It is important to be confident that the number of  $gg$  and  $gq$  events being generated are proportional to the cross-sections of the two processes. For example, if the  $gg$  cross-section makes up 30% of the total cross-section for a certain invariant mass window, then 30% of the events generated should be  $gg$ . In this table, this is investigated.

Number of Events Generated	Quadrature ( $gg, gq$ )	Monte Carlo Integration ( $gg, gq$ )	Event Fraction ( $gg, gq$ )
11,000	17.999%, 82.001%	17.931%, 82.069%	18.010%, 81.990%
150,000	—	17.981%, 82.019%	18.006%, 81.994%

Table 3: Proportion of cross-section and generated events for the  $gg$  and  $gq$  processes. Cross-section integrated over  $M = [M_{cut}, \sqrt{s}]$ ,  $\sqrt{s} = 13 \text{ TeV}$ ,  $M_s = 5 \text{ TeV}$

## 6.3 Kinematic Data

In the produced  $\gamma + \text{jet}$  events, there are several kinematic quantities the outgoing partons possess that are of interest. In no particular order, they are; the 4-vectors of each outgoing particle, the radial and azimuthal coordinates  $\theta$  and  $\phi$ , the transverse momentum  $p_T$ , the energy, and the invariant mass. When the parton and photon quantities are summed, we get the characteristics of the string resonance. Histograms that convey this data are shown in Appendix 8.4.

On the next pages are histograms that have been created by superimposing each  $\gamma + \text{jet}$  invariant mass histogram for  $\sqrt{s} = 13 \text{ TeV}$  and  $13.6 \text{ TeV}$ :

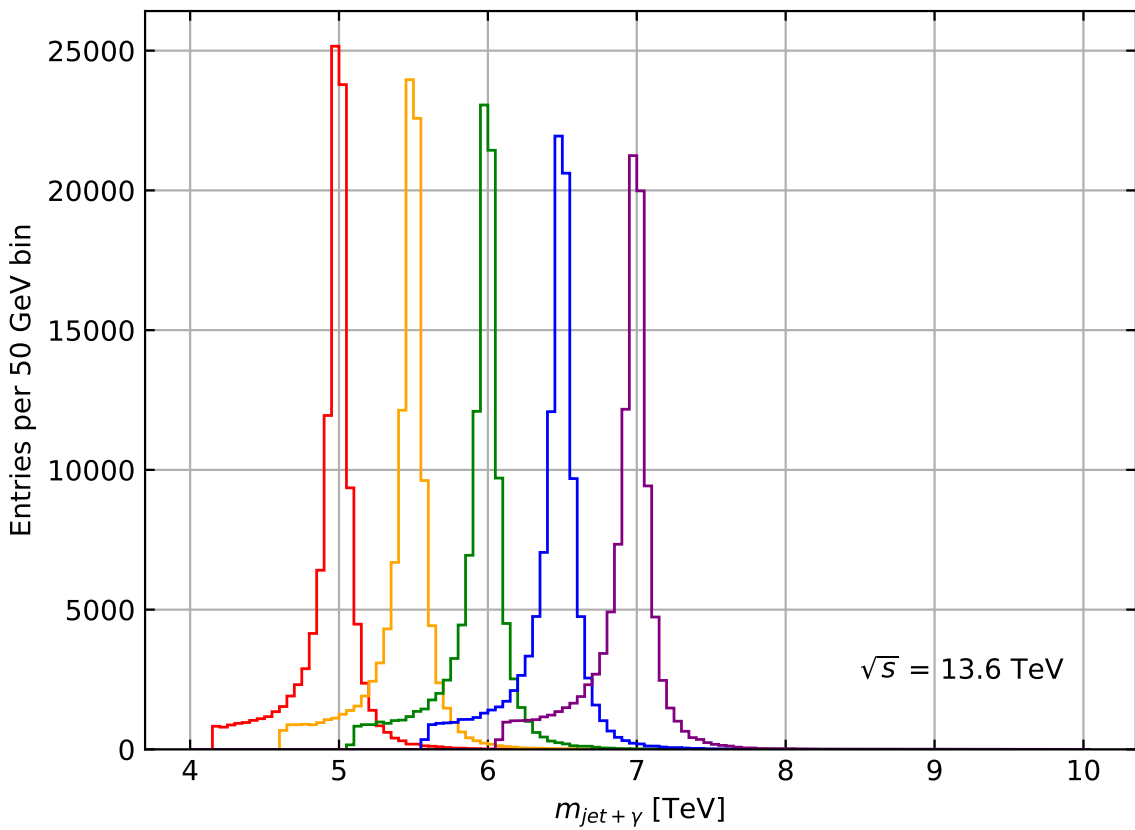
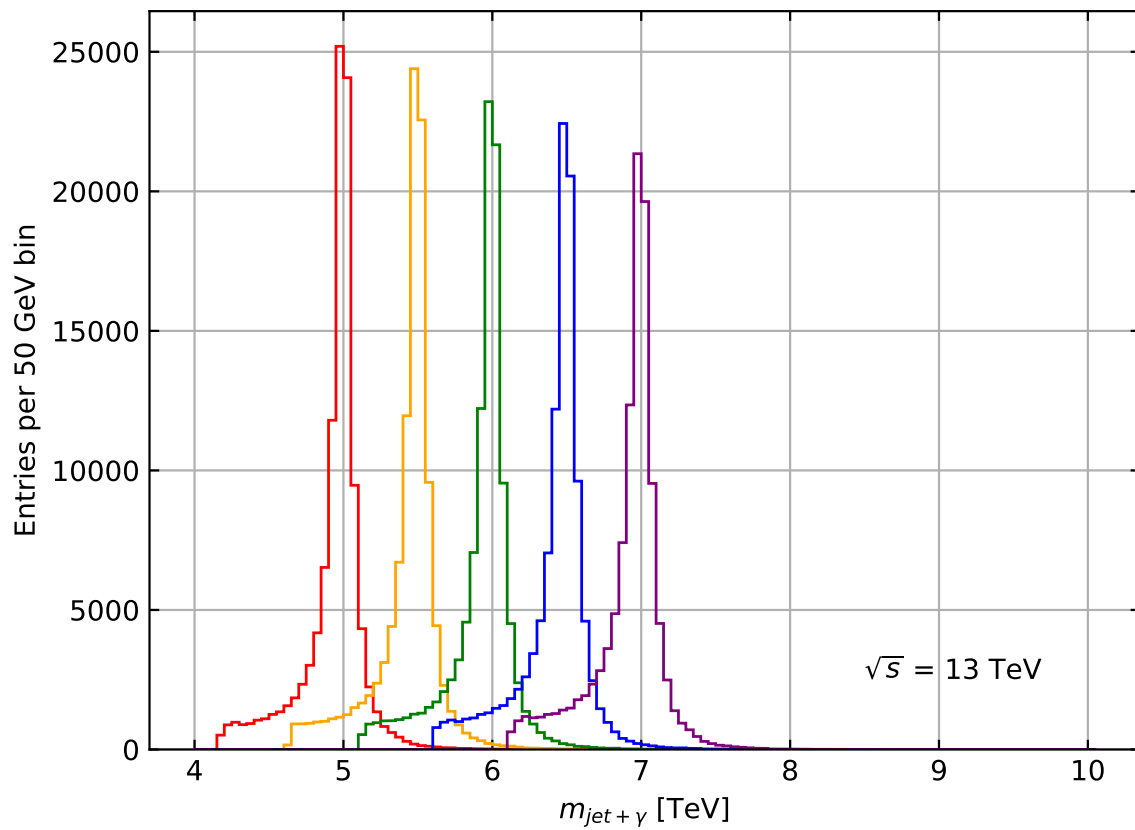


Figure 29: (Linear Axis)

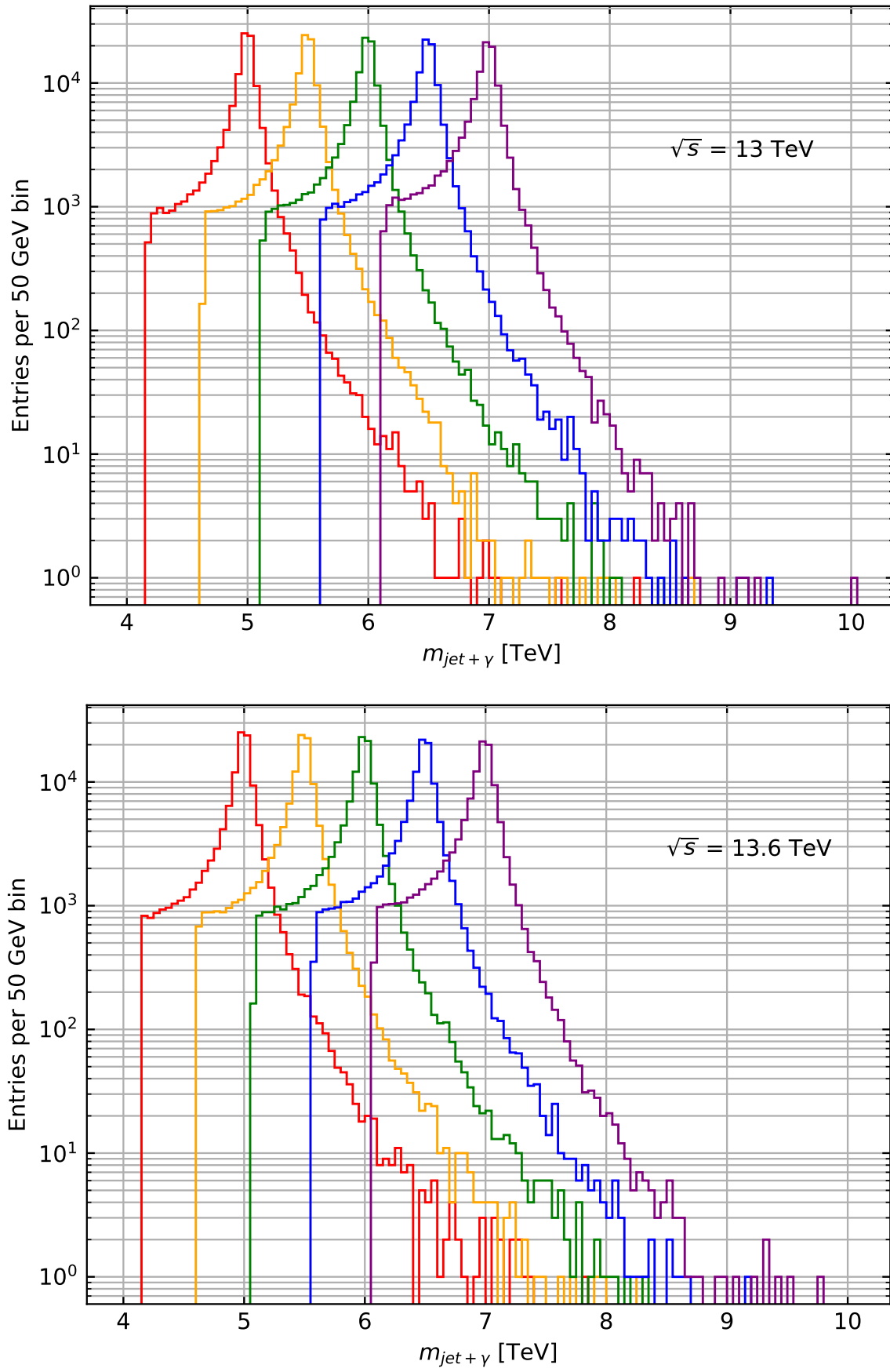


Figure 30: (Logarithmic Axis)

### 6.3.1 Angular Distribution Study

The radial angle  $\theta$  changes depending on whether is being measured in the lab frame or the resonance frame, where the radial angle is defined as  $\theta^*$ . In the resonance frame, the  $z$  momentum cancels out and the radial and azimuthal angles are opposite to each other for each outgoing parton.

The cosine of the radial angle is given by  $\theta = \frac{p_z}{p}$ . To convert  $p_z$  into the resonance frame, a Lorentz boost is applied along the  $z$ -axis:

$$p_z^* = \gamma(p_z - E\beta) \quad (36)$$

where

$$\gamma = \frac{E^s}{M^s} \quad \beta = \frac{p_z^s}{E^s} \quad (37)$$

The superscript  $s$  stands for 'string.' The distribution of the radial cosines is described by the curve  $2 + 3x^2$  in the  $gg$  case, and  $\frac{94}{25} + 6x^2 + x^4$ , where  $x = \cos \theta^*$ .

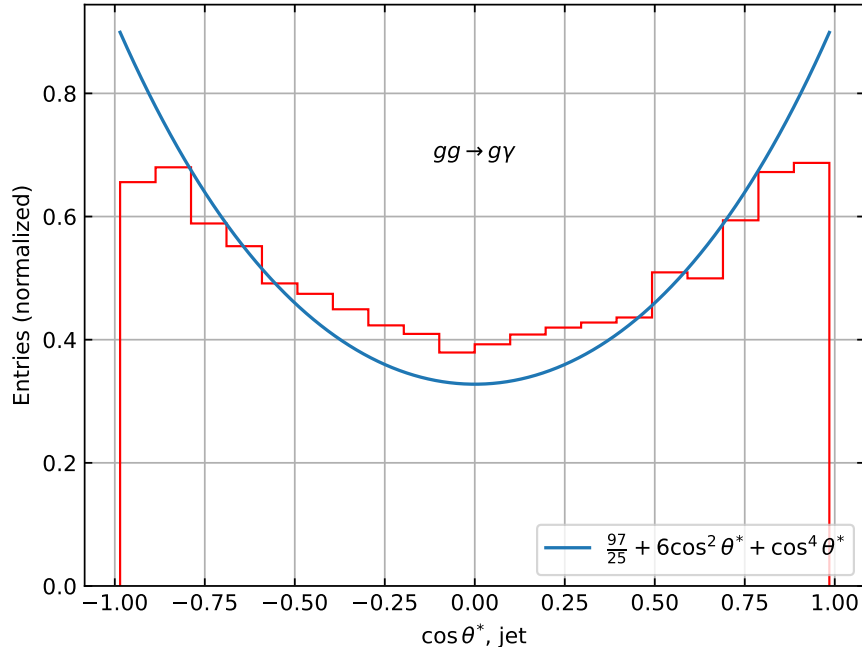


Figure 31: Angular distribution for  $M_s = 5$  TeV

One can observe that toward the  $+1$  and  $-1$ , the histogram does not match the predicted distribution. The STRINGs generator has changed since the ATLAS note. The theory is an approximation of being at the resonance, but there is actually a mass distribution. In past trials, this approximation seemed to work well [17]:

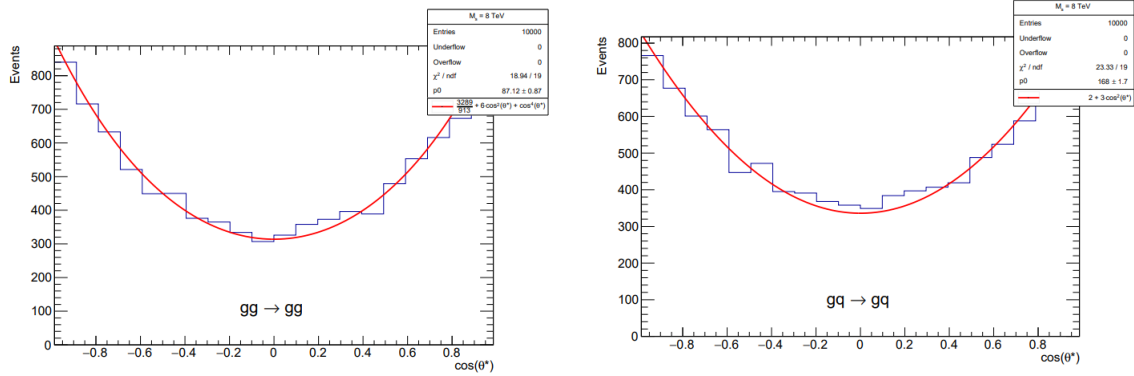


Figure 32: Angular distributions

It is possible the old version of STRINGS was more accurate than it should have been. Also for higher string scales, the distribution may be more accurate.

Furthermore, the maximum rapidity cut on the data generated was 2.5. This cut minimizes how close an outgoing parton's trajectory can be to the beam axis. With a higher rapidity cut, the distribution may be more closely matched by allowing more events to scatter partons close to the beam axis (such events would have a  $\cos \theta^*$  close to  $\pm 1$ ).

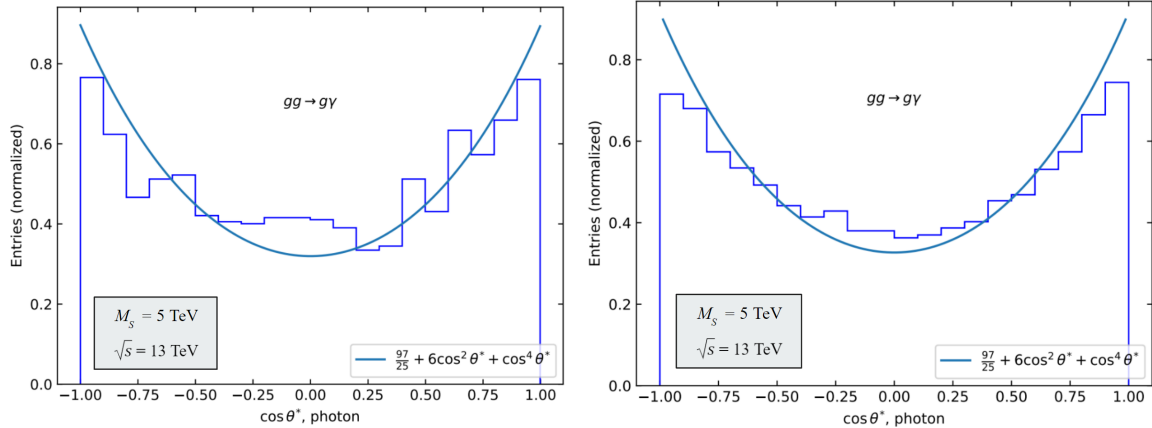


Figure 33: 11,000 events,  $y_{cut} = 10$ ; 110,000 events,  $y_{cut} = 6$

Given the data in the above figures, this seems to be the case. A cut of 6 gives a shape closer to the predicted distribution. A cut of 10 would likely be even better, but because imposing greater cuts vastly increases the time it takes for the generator to run, not many events were generated. It is likely that with more events, the distribution would be smoother.

## 6.4 Pythia Samples

Following the STRINGS simulations, LHE files are fed into the Pythia program, which is a much more sophisticated and realistic generator used for simulating scattering events. The histograms on the next page are generated using ROOT, and follow the same color scheme as the corresponding previous STRINGS histograms (note that the data in the top right-hand box is for the  $M_s = 5$  TeV dataset). Histograms presenting other kinematic variables like  $\eta$ ,  $\phi$ , and  $p_\perp$  are in appendix

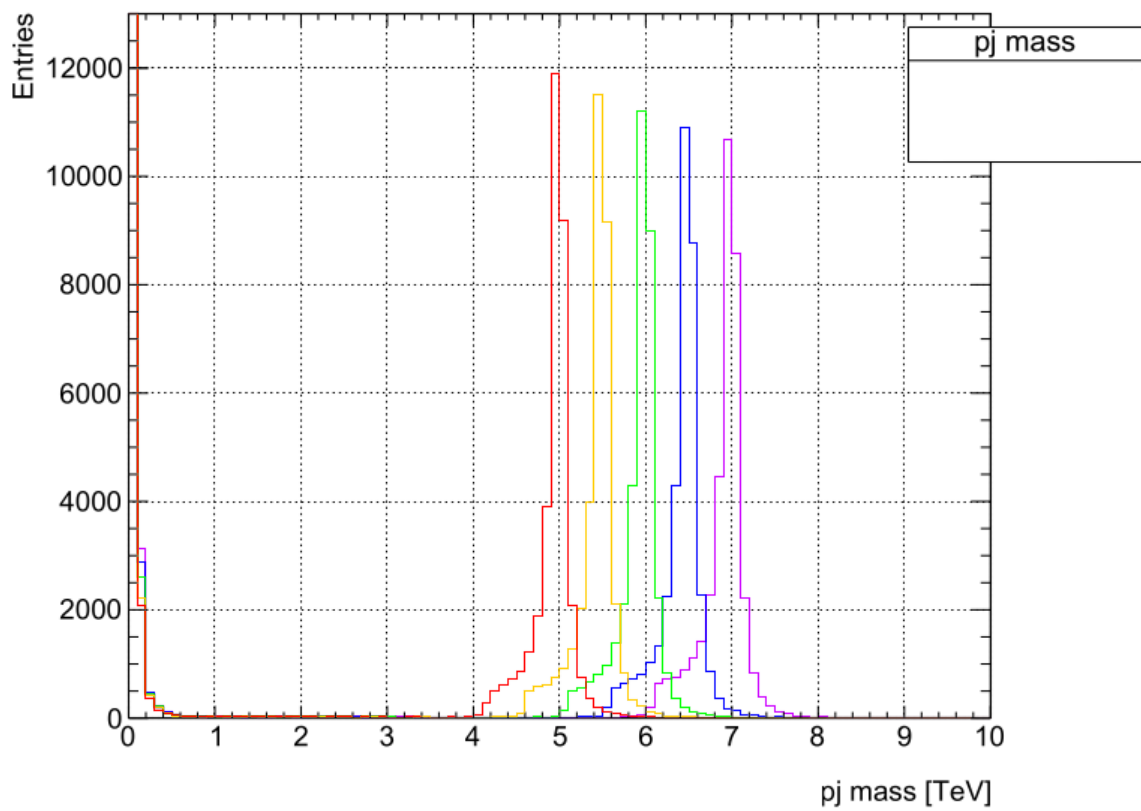
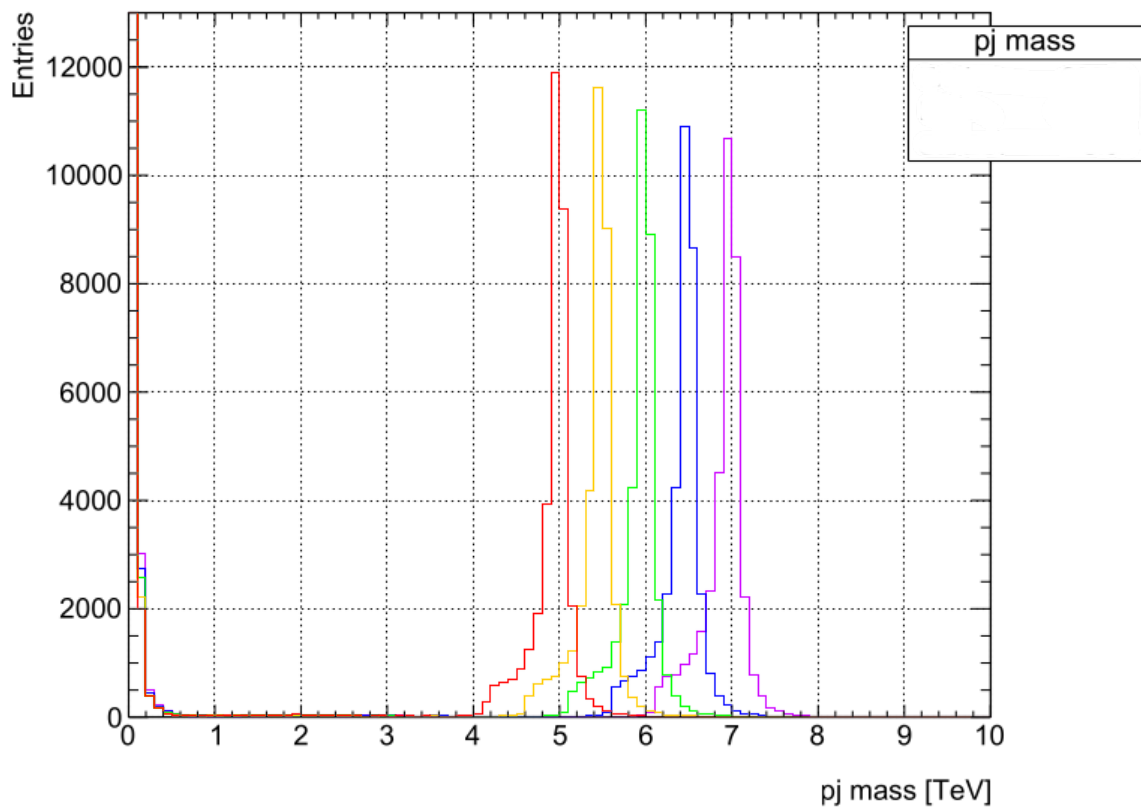


Figure 34: Linear Axis;  $\sqrt{s} = 13$  TeV (top) and 13.6 TeV (bottom)

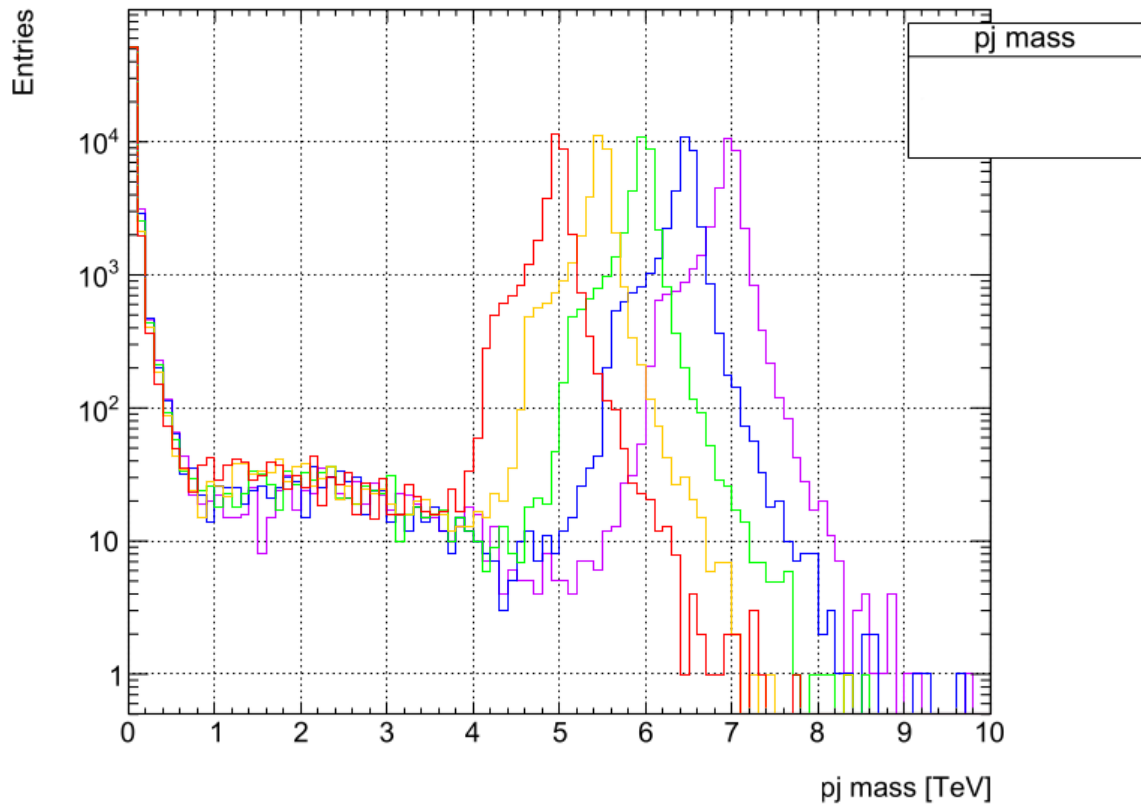
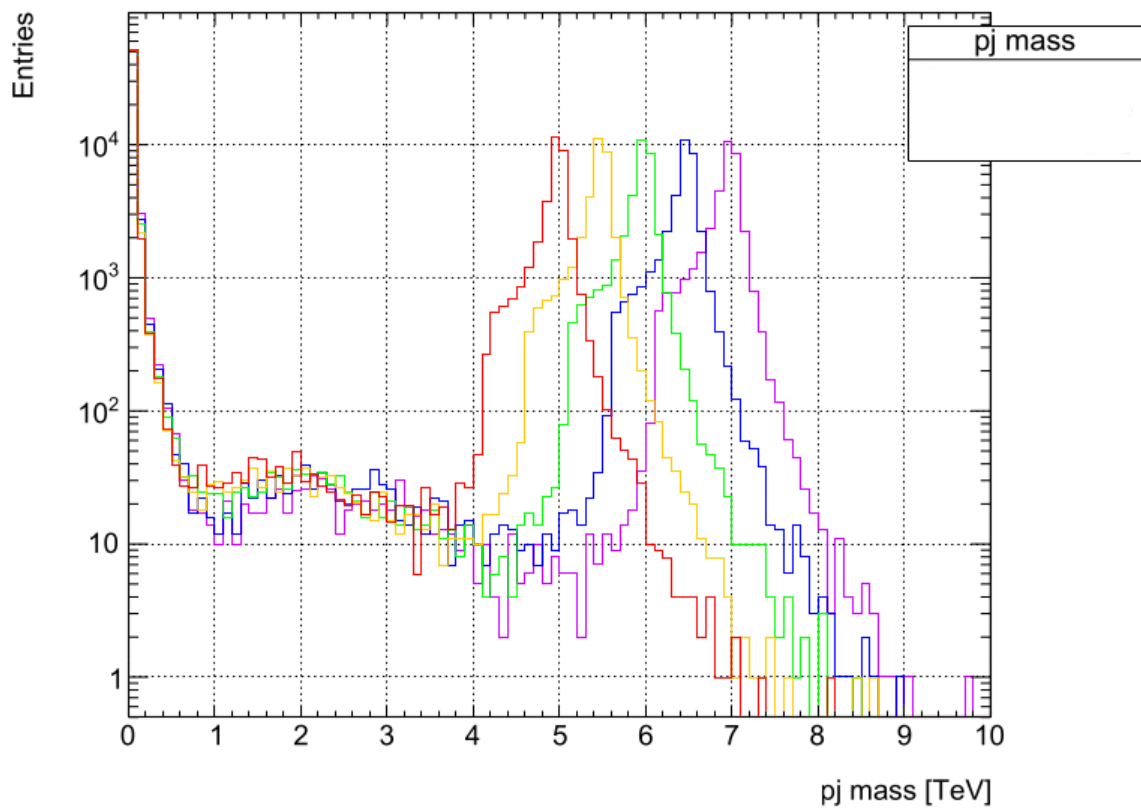


Figure 35: Logarithmic Axis;  $\sqrt{s} = 13$  TeV (top) and 13.6 TeV (bottom)

## 7 Conclusions

After concluding our Monte Carlo resonance search, there are several conclusions that we may draw. Firstly, the Pythia events generated demonstrate the resonance peaks are remarkably similar for  $\sqrt{s} = 13$  and 13.6 TeV, meaning that discovery potential at either  $\sqrt{s}$  is relatively consistent. The evolution of the resonance peak shape as  $M_s$  is consistent with our expectation; as  $M_s$  increases, the peak gets shorter and thicker at the base.

As evidenced in the initial attempt, the discovery potential for string scales on the interval [7,9] TeV is problematic because there is a significant decrease in the number of events as compared to [5,7] TeV. For studying photon jet scattering processes, discovery potential is much higher at scales lower than 7 TeV. We also observe a drastic low-mass tail in all of the invariant mass distributions generated by Pythia. These low-mass events are of little interest and could obscure events that we are interested in studying at the LHC.

Going into the future, for the purposes of resonance searches in photon jet scattering events with ATLAS at the LHC, the data acquired in this study will be especially useful, and is planned on being sent to ATLAS colleagues.

## 8 Sources

- 1 D. Gingrich, P. Vakilipourtakalou, STRINGS with PYTHON (15 December 2022).
- 2 N. Wolchover, S. Velasco, L. Reading-Ikkanda. "A New Map of All the Particles and Forces." (22 October 2020) <https://www.quantamagazine.org/a-new-map-of-the-standard-model-of-particle-physics-20201022/>
- 3 N. Arkanihamed, S. Dimopoulos, and G. Dvali. "The hierarchy problem and new dimensions at a millimeter". In: Physics Letters B 429.3-4 (1998), pp. 263–272. issn: 0370-2693. doi: 10.1016/s0370-2693(98)00466-3. url: [http://dx.doi.org/10.1016/S0370-2693\(98\)00466-3](http://dx.doi.org/10.1016/S0370-2693(98)00466-3)
- 4 F. Lyons. "Search for Low-Scale String Resonances with ATLAS at the Large Hadron Collider." (2021)
- 5 D. Lüst, S. Stieberger, and T. R. Taylor. "The LHC string Hunters companion". In: Nuclear Physics B 808.1-2 (2009), pp. 1–52. issn: 0550-3213. doi: 10.1016/j.nuclphysb.2008.09.012. url: <http://dx.doi.org/10.1016/j.nuclphysb.2008.09.012>
- 6 A. Banfi. "Hadronic Jets." 2053-2571. Morgan and Claypool Publishers, 2016. isbn: 978-1-6817-4073-7. <http://dx.doi.org/10.1088/978-1-6817-4073-7>
- 7 R. C. Myers and S. E. Vázquez. "Quark soup al dente: applied superstring theory". In: Classical and Quantum Gravity 25.11 (2008), p. 114008. doi: 10.1088/0264-9381/25/11/114008. url: <https://doi.org/10.1088/0264-9381/25/11/114008>.
- 8 D. Griffiths. Introduction to Elementary Particles. Physics textbook. Wiley, 2008. ISBN: 9783527406012. url: <https://books.google.ca/books?id=w9Dz56myXm8C>
- 9 L. Anchordoqui, H. Goldberg, S. Nawata, T. Taylor. "Direct photons as probes of low mass strings at the LHC." (April 2008) <https://arxiv.org/abs/0804.2013>.
- 10 L. Anchordoqui et al, String Resonances at Hadron Colliders, Phys. Rev. D 90 (2014) 066013, [ArXiv:1407.8120 [hep-ph]]
- 11 "Mandelstam Variables." image taken from <http://www.mysearch.org.uk/website1/html/610.Mandelstam.html>
- 12 T. Regge. "Introduction to complex orbital momenta". In: Il Nuovo Cimento (1955-1965) 14 (1959), pp. 951–976
- 13 J Alwell et al. "A standard format for Les Houches Event Files." 2 February 2008. arXiv:hep-ph(?)609017v1
- 14 S. Dimopoulos, G. Landsberg. "Black Holes at the LHC." (27 June 2001).<https://arxiv.org/abs/hep-ph/0106295>
- 15 P. Vakilipourtakalou, D. Gingrich. "Monte Carlo Event Generator for the Production and Decay of String Resonances in Proton-Proton Collisions. STRINGS Version 1.00." 19 November 2018. arXiv.1811.07458v1
- 16 <https://universe-review.ca/R15-17-relativity14.htm>
- 17 Gingrich et al. "Search for new phenomena in dijet events using 3 quark/gluon tagging based on track multiplicity." (draft version 0.3) 25 January 2022.

## 9 Appendices

### 9.1 $\alpha_s$ Coupling Testing

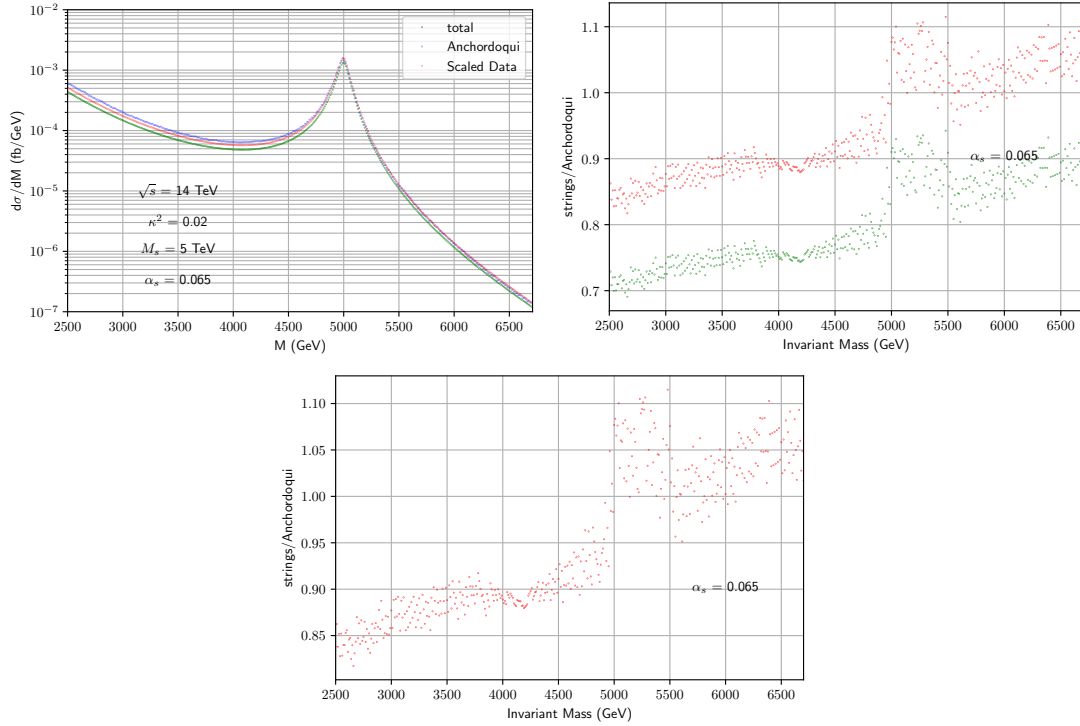


Figure 36:  $\alpha_s = 0.065$

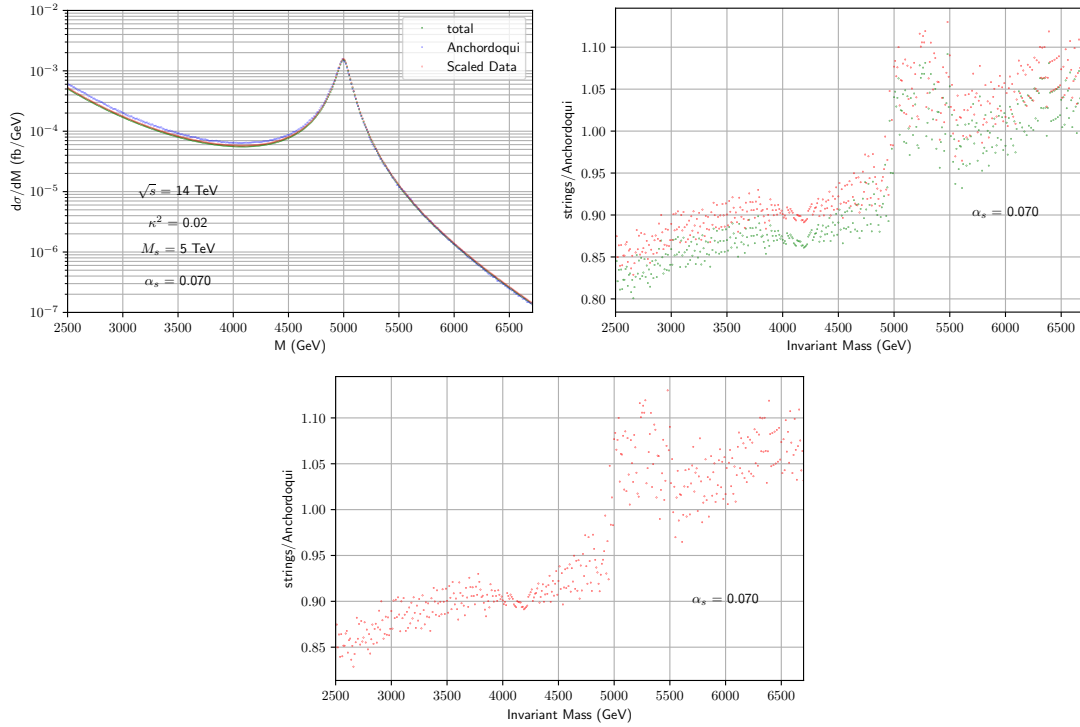


Figure 37:  $\alpha_s = 0.070$

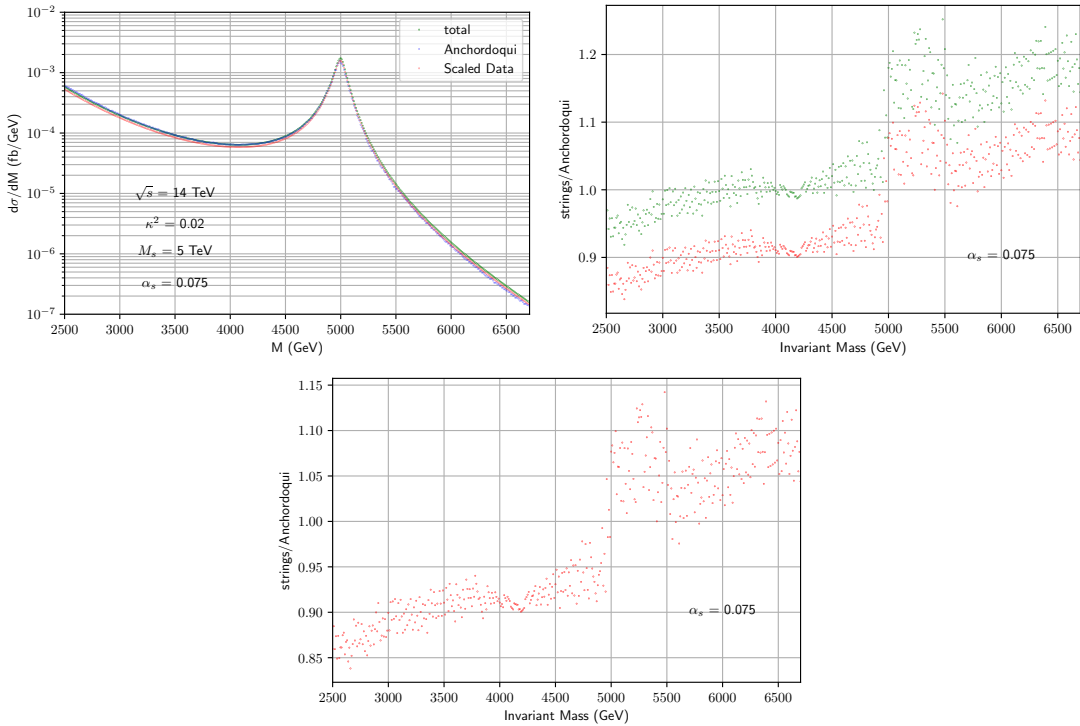


Figure 38:  $\alpha_s = 0.075$

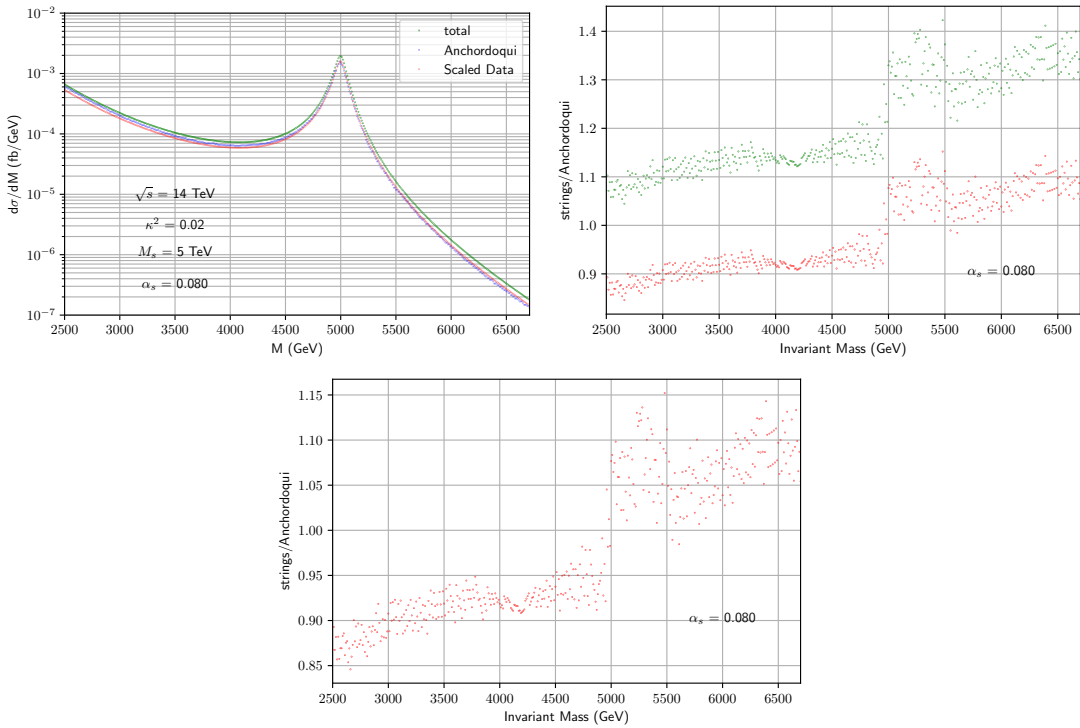


Figure 39:  $\alpha_s = 0.080$

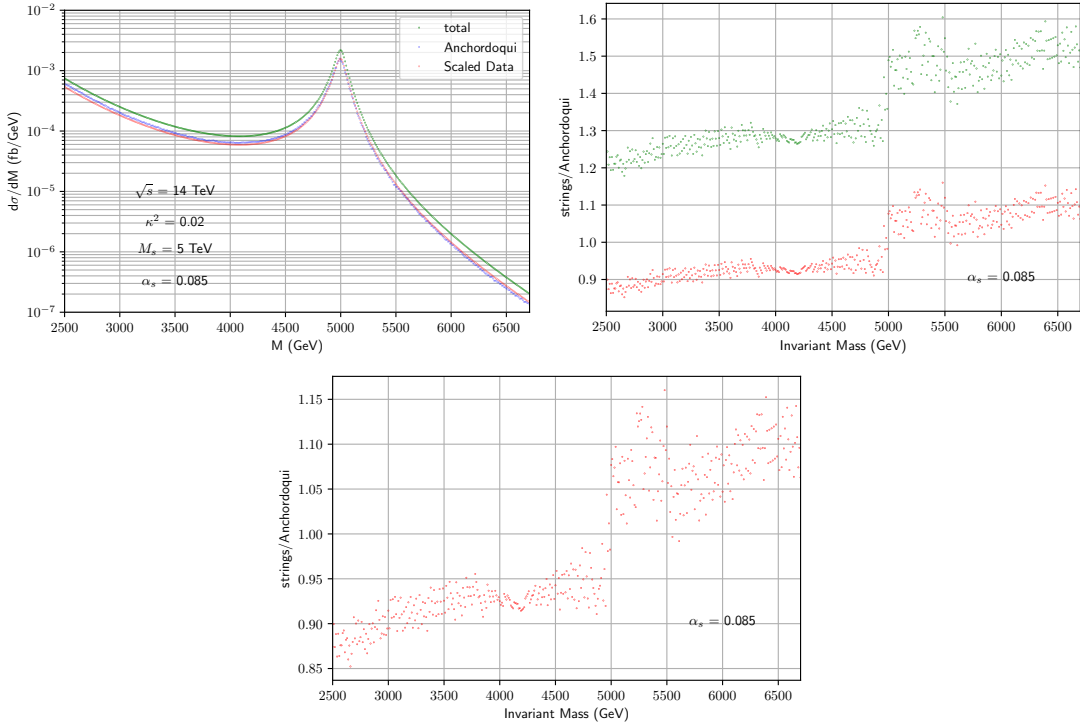


Figure 40:  $\alpha_s = 0.085$

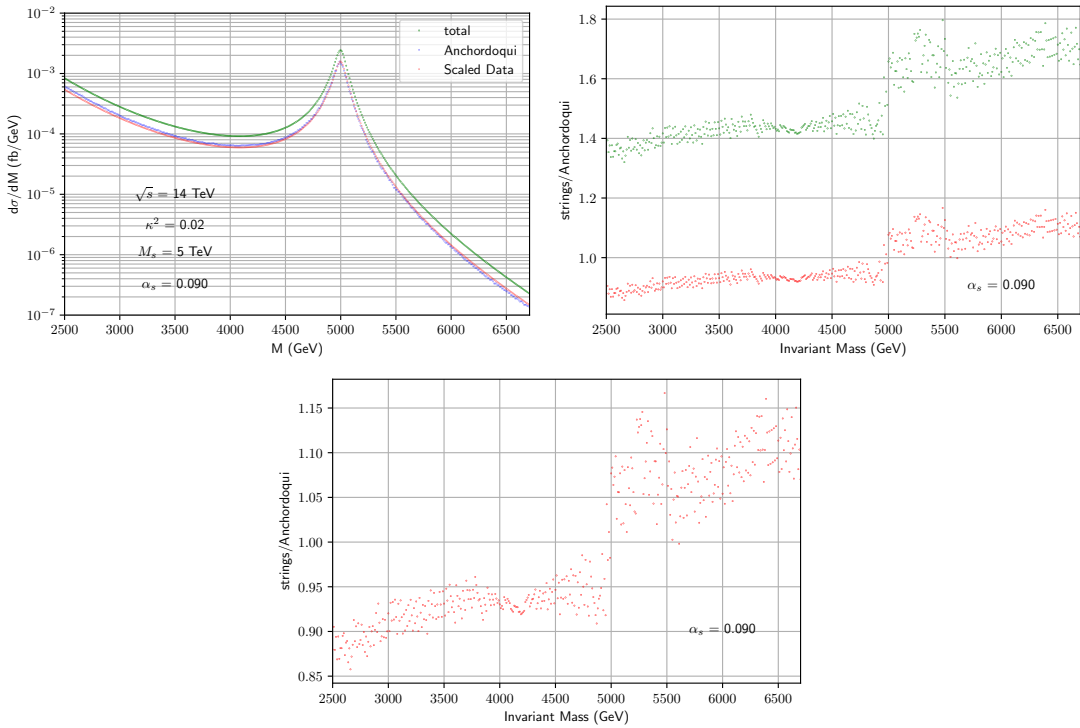


Figure 41:  $\alpha_s = 0.090$

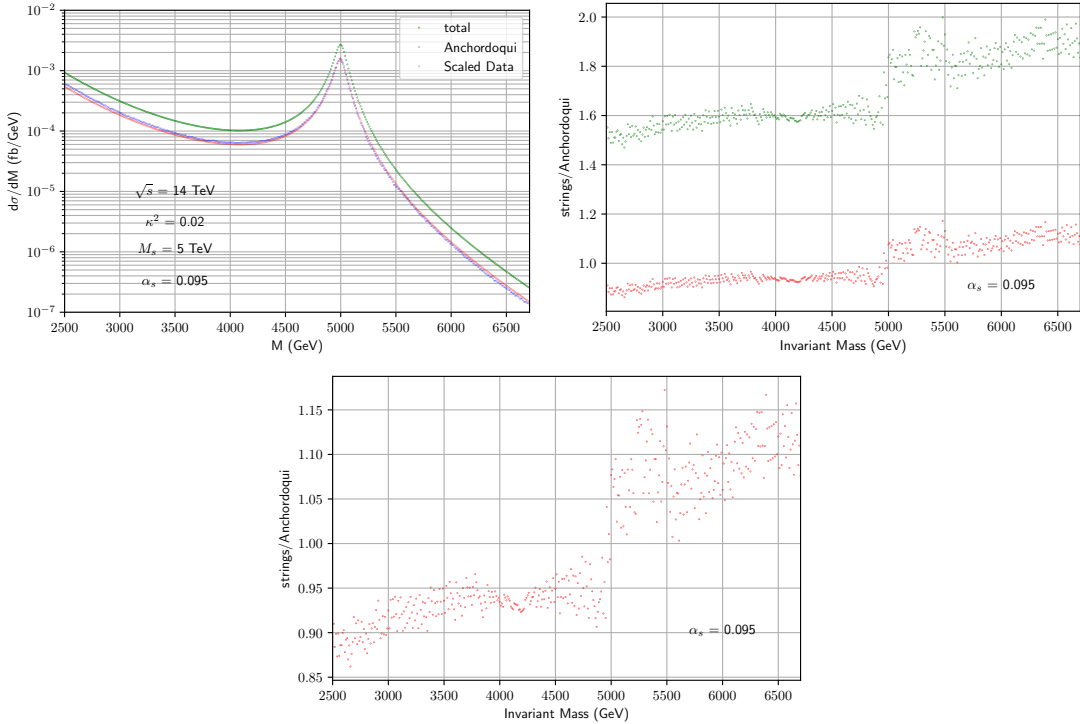


Figure 42:  $\alpha_s = 0.095$

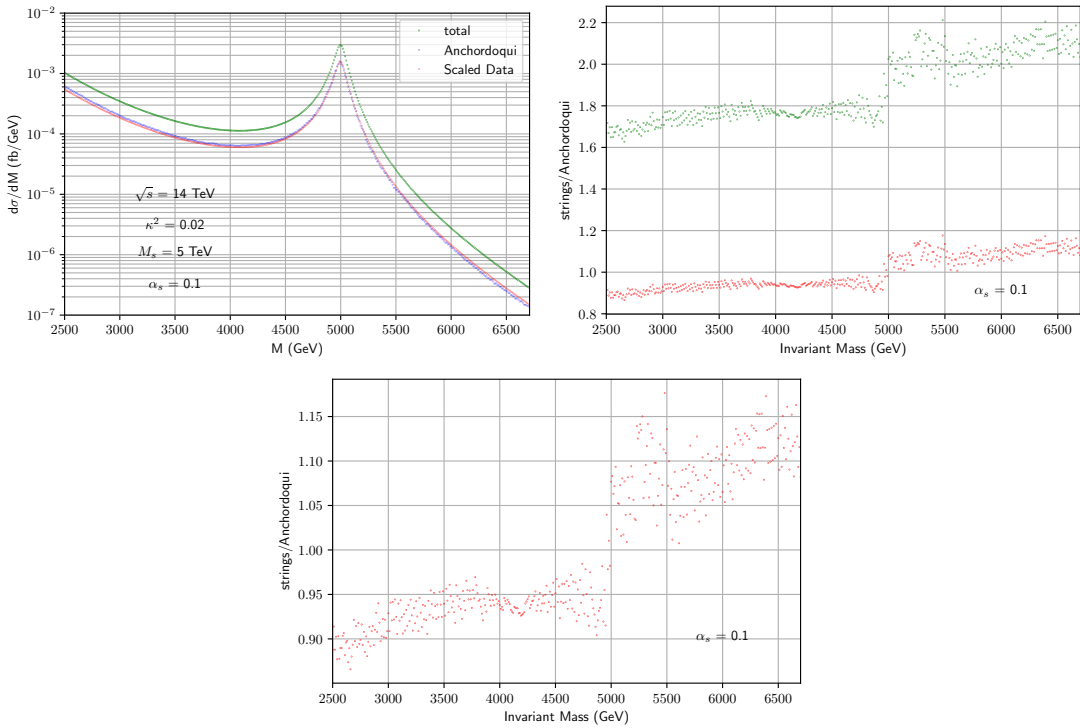


Figure 43:  $\alpha_s = 0.100$

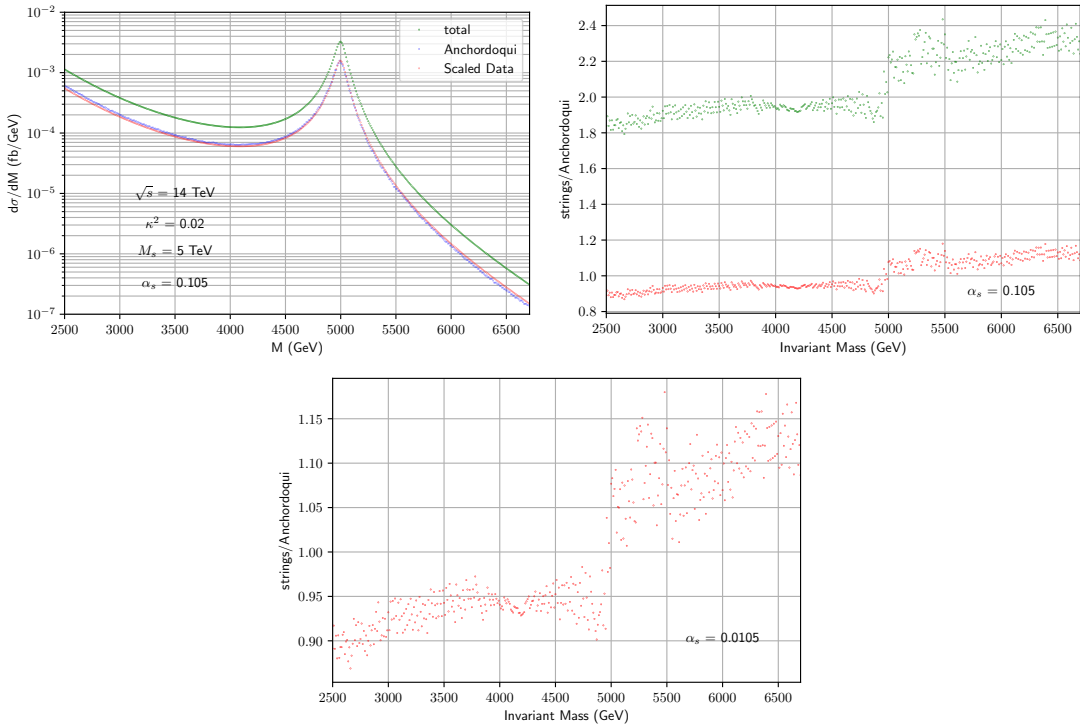


Figure 44:  $\alpha_s = 0.105$

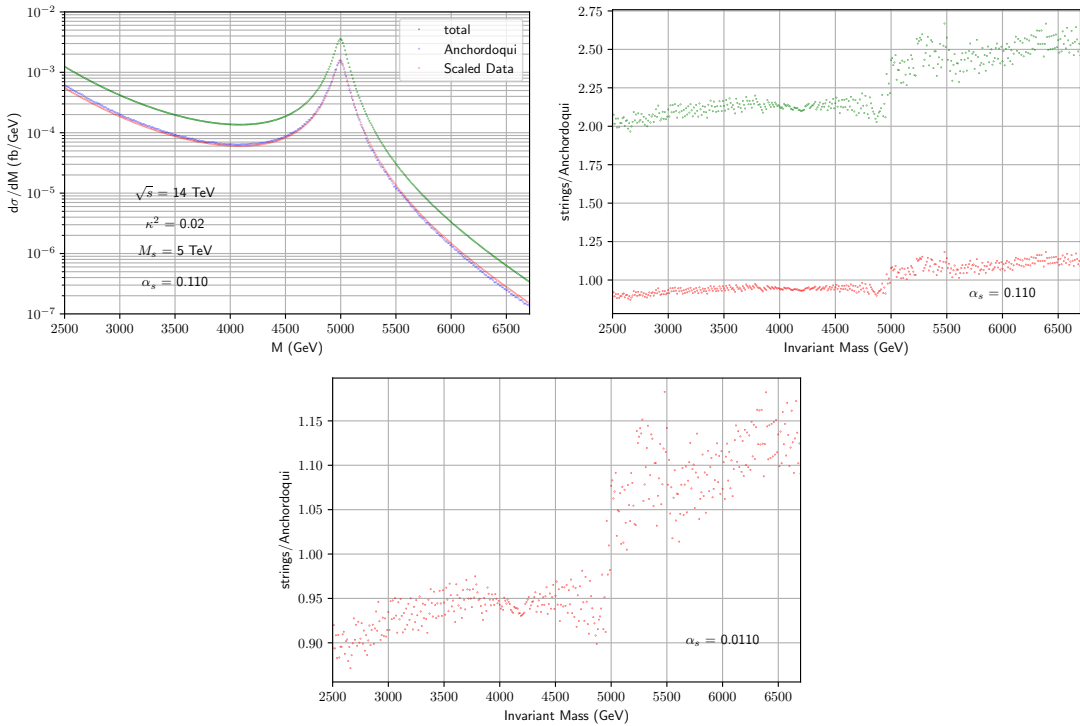


Figure 45:  $\alpha_s = 0.110$

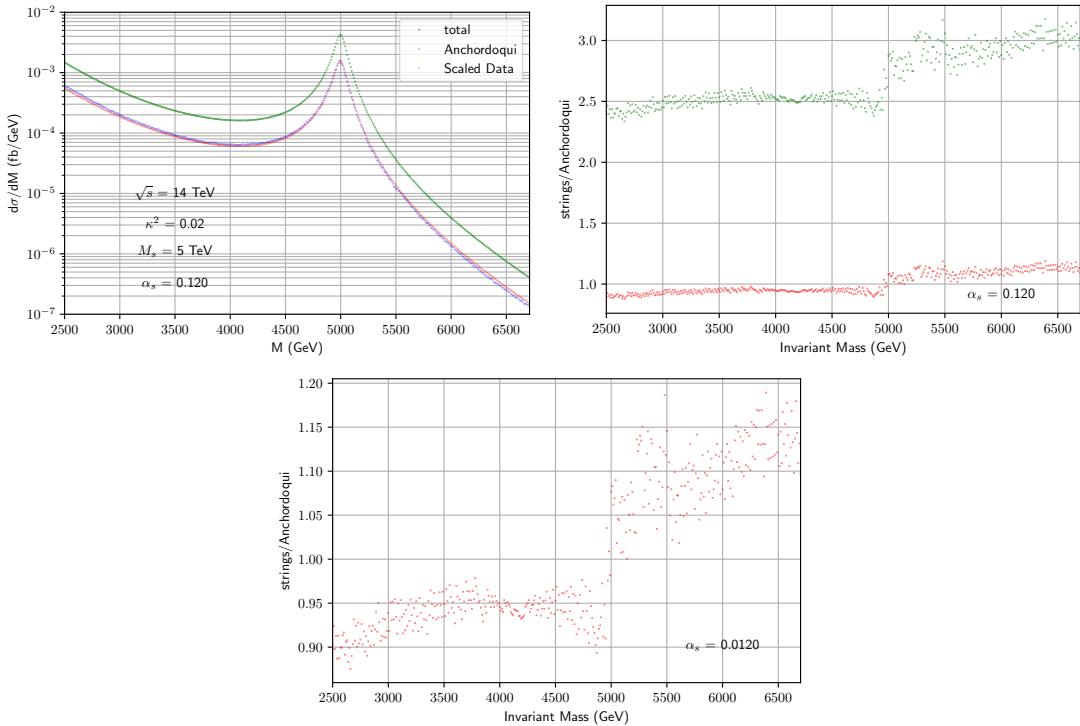


Figure 46:  $\alpha_s = 0.120$

## 9.2 Cross-section vs. $M_s$ Invariant Mass BOI Testing

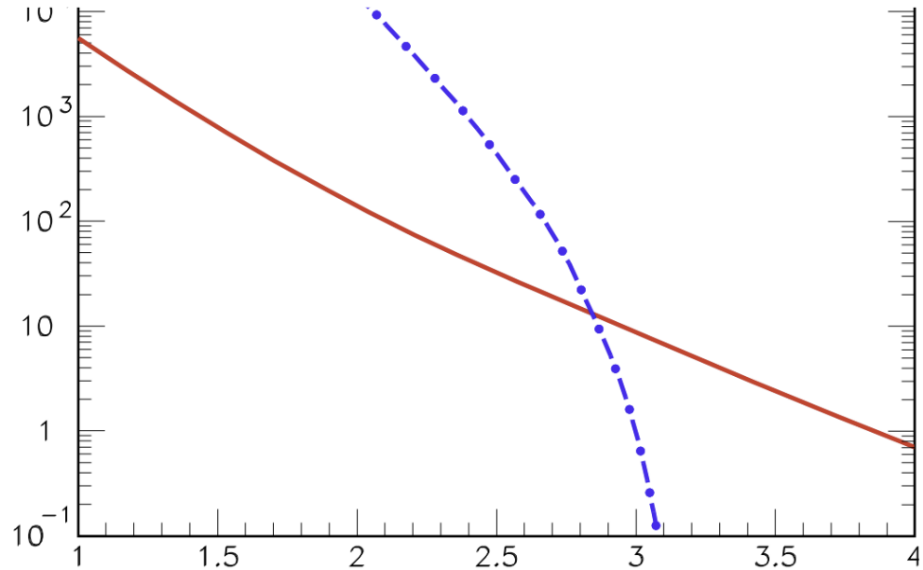


Figure 47: Plot from Anchordoqui et al, [9]

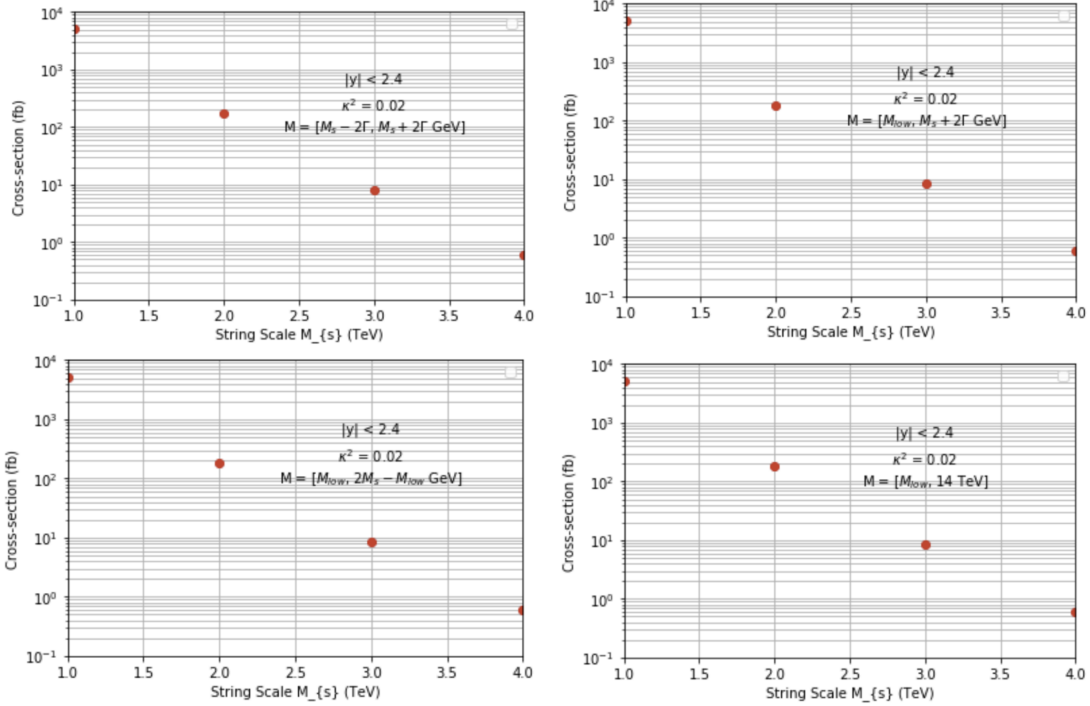


Figure 48: Different plots using different BOIs trying to match Fig 33 plot. (BOI directly on plot).

### 9.2.1 Finding $M_{cut}$

We plot the differential cross-section as a function of invariant mass  $M = [1, 14 \text{ TeV}]$  for  $M_s = 1, 1.5, 2, 2.5, 3, 3.5, 4 \text{ TeV}$  in steps of 0.5 TeV:

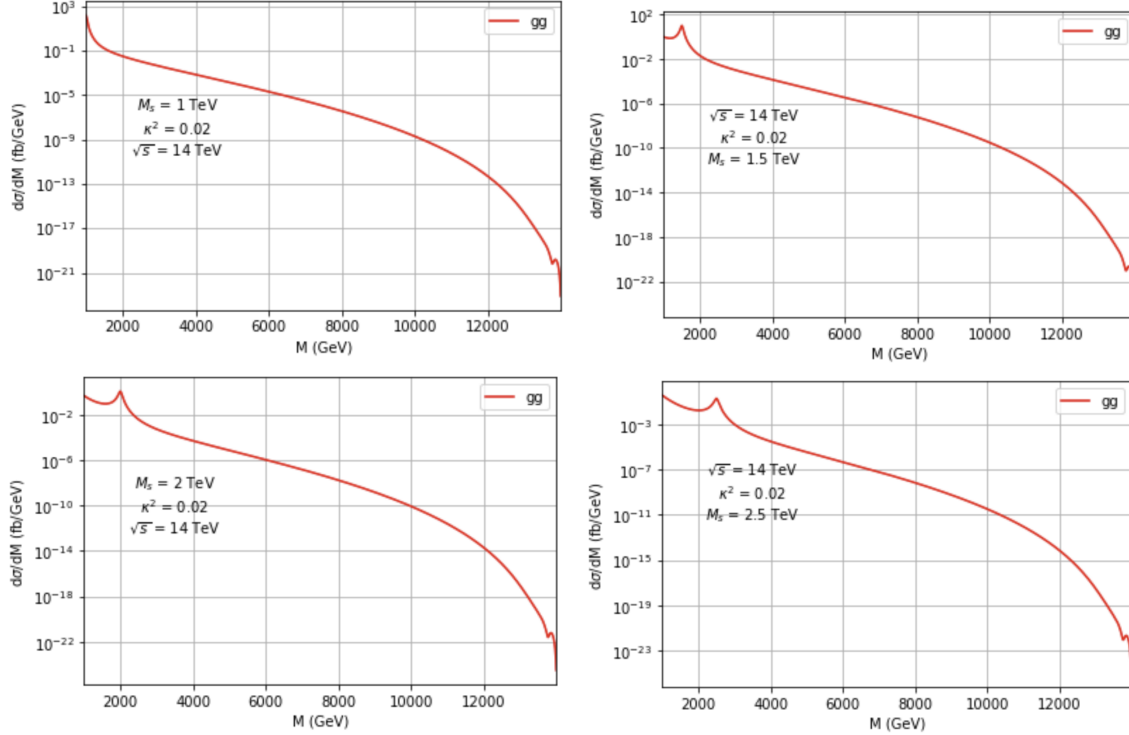


Figure 49: Breit Wigner curves for  $M_s = [1, 2.5] \text{ TeV}$

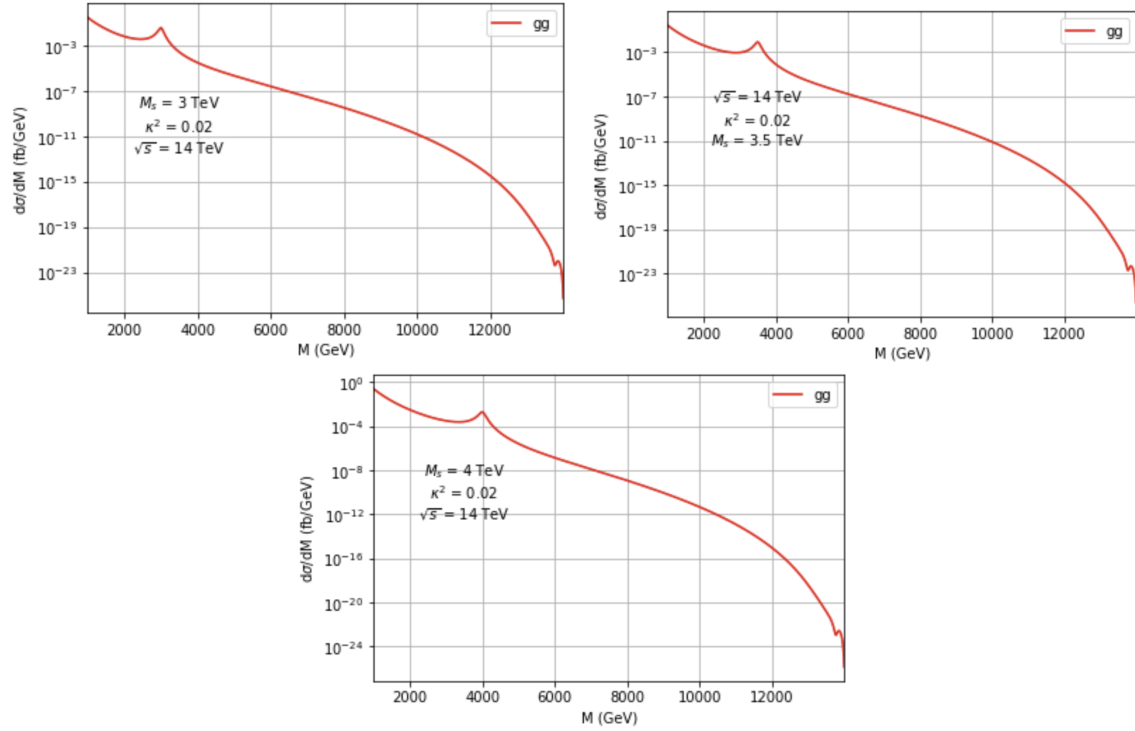


Figure 50: Breit Wigner curves for  $M_s = [3, 4]$  TeV

String Scale $M_s$ [TeV]	$M_{cut}$ [GeV]
1	NA
1.5	1170
2	1590
2.5	2010
3	2450
3.5	2890
4	3350

Table 4: String scale vs Minimum differential cross-section

### 9.3 Differential Cross-sections

#### 9.3.1 $M_s = [7, 9]$ TeV

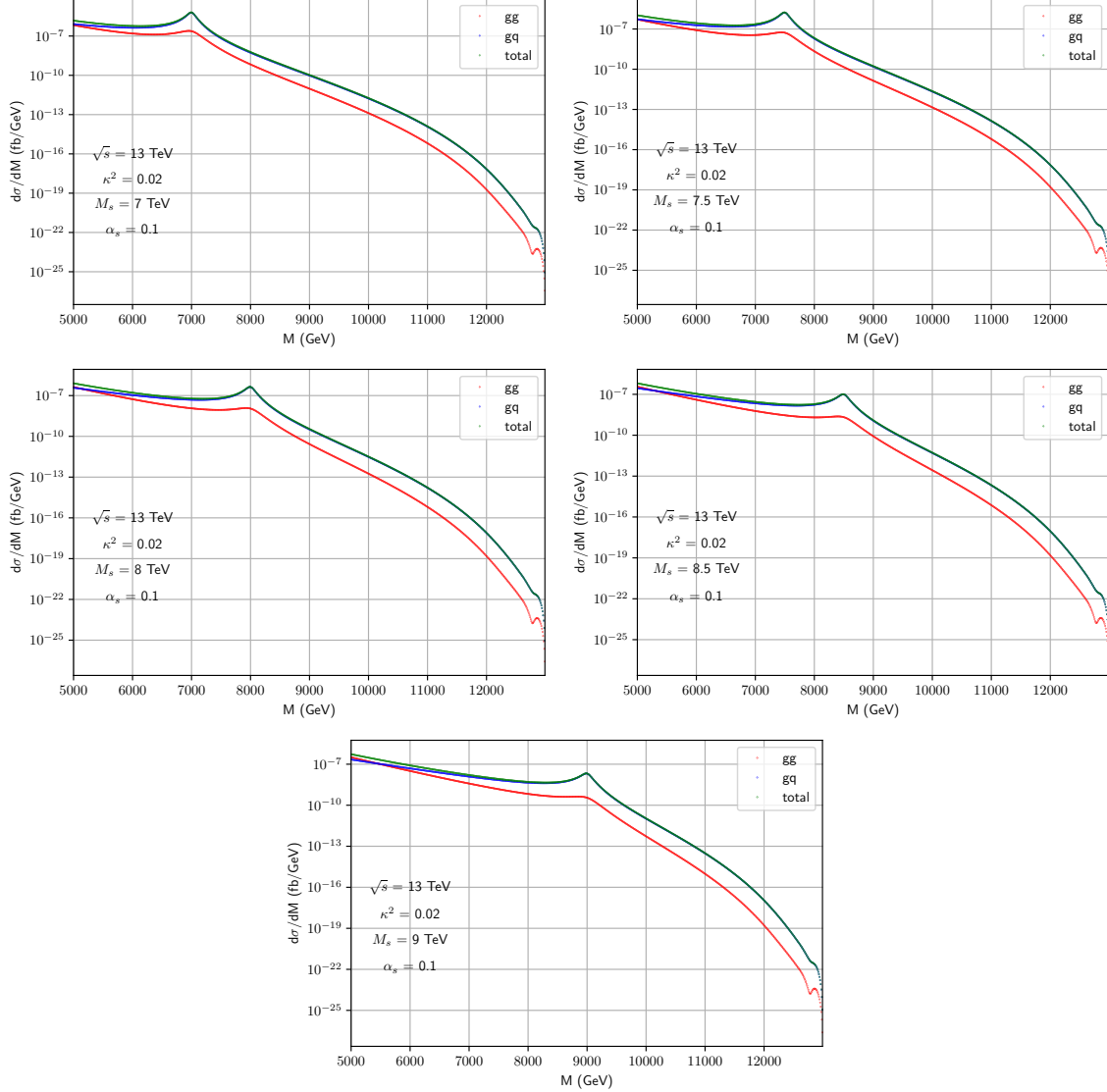


Figure 51: Differential cross-section curves for  $M_s = [7, 9]$  TeV,  $\sqrt{s} = 13$  TeV. Note that there is a typo in these plots:  $\alpha_s$  is the running coupling, not 0.1.

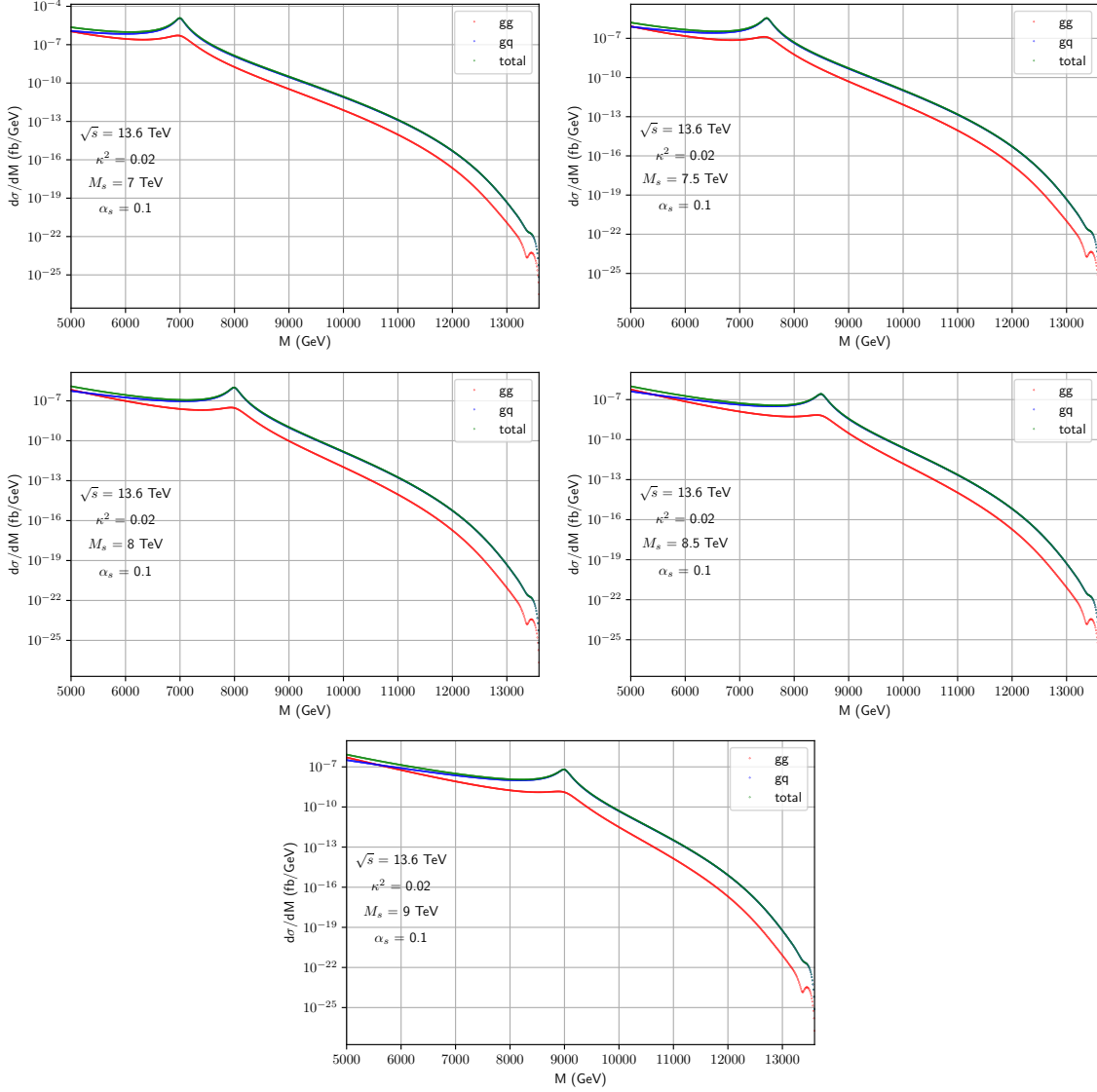


Figure 52: Differential cross-section curves for  $M_s = [7, 9]$  TeV,  $\sqrt{s} = 13.6$  TeV. Note that there is a typo in these plots:  $\alpha_s$  is the running coupling, not 0.1.

String Scale $M_s$ [TeV]	$M_{cut}, \sqrt{s} = 13$ TeV [TeV]	$M_{cut}, \sqrt{s} = 13.6$ TeV [TeV]
7	6.04	6.09
7.5	6.60	6.60
8	7.19	7.13
8.5	7.74	7.67
9	8.30	8.22

Table 5: Lower mass cuts for each  $M_s$ ,  $\sqrt{s}$

### 9.3.2 $M_s = [5, 7]$ TeV

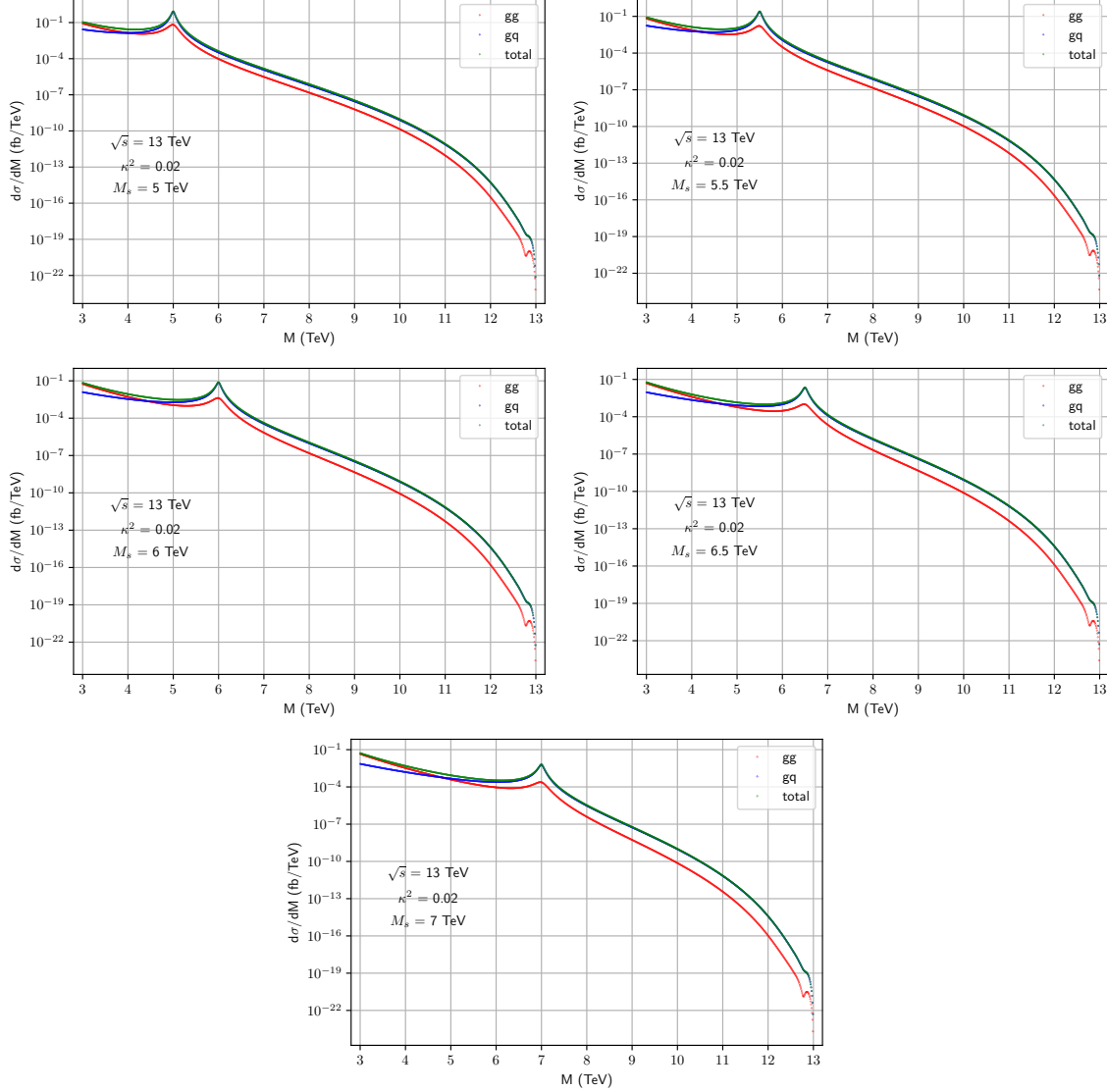


Figure 53: Differential cross-section curves for  $M_s = [5, 7]$  TeV,  $\sqrt{s} = 13$  TeV

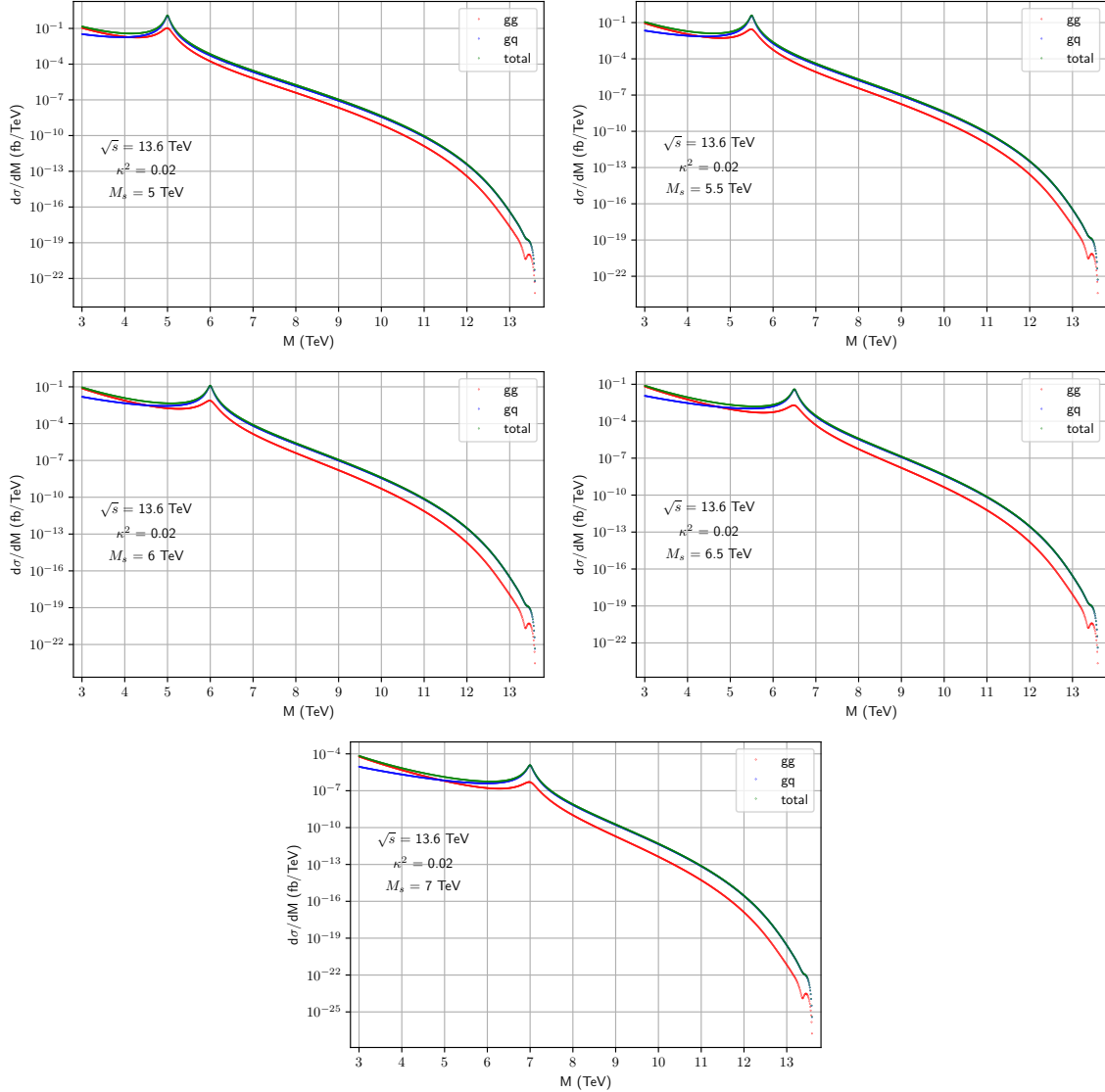


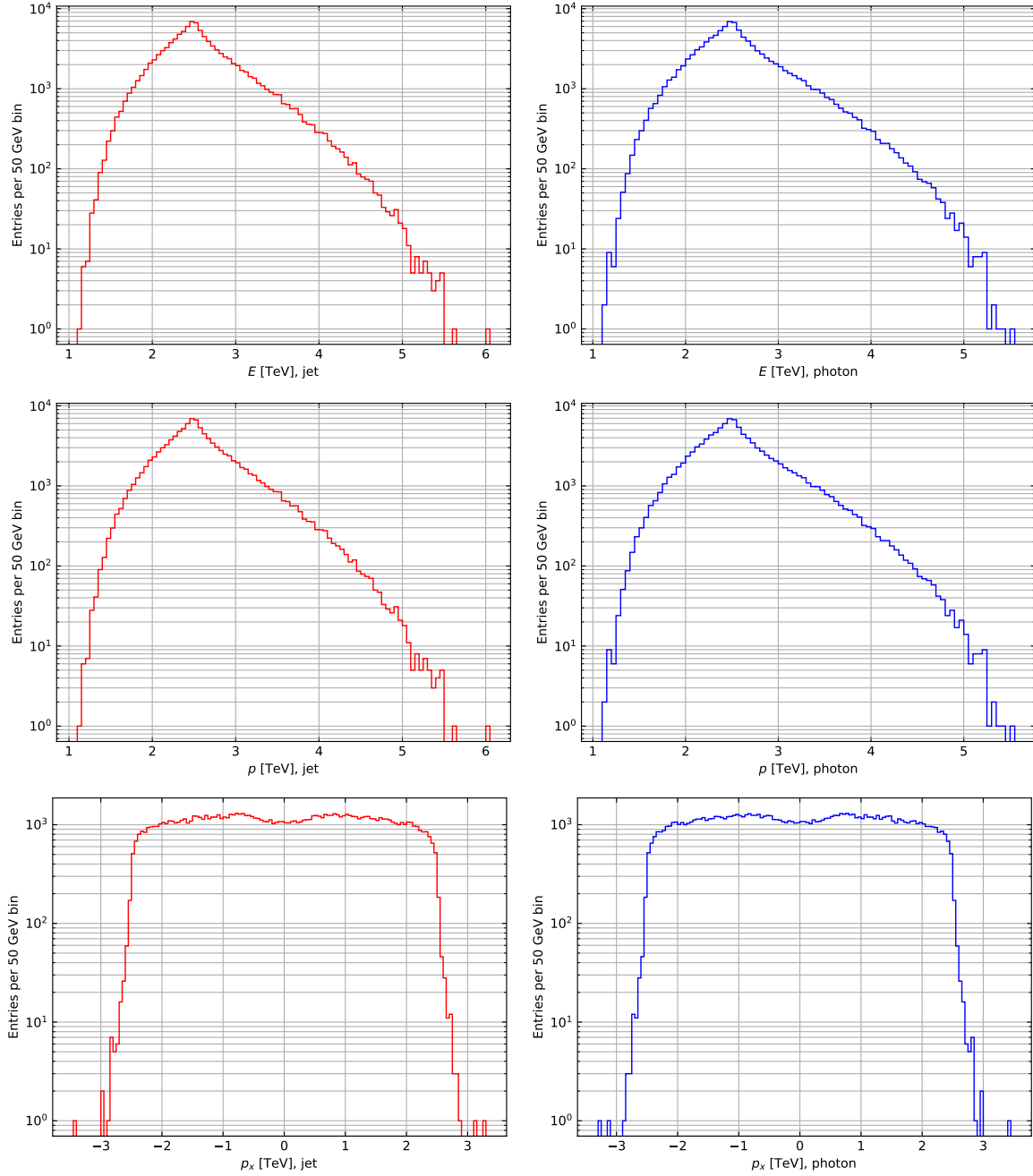
Figure 54: Differential cross-section curves for  $M_s = [5, 7]$  TeV,  $\sqrt{s} = 13.6$  TeV

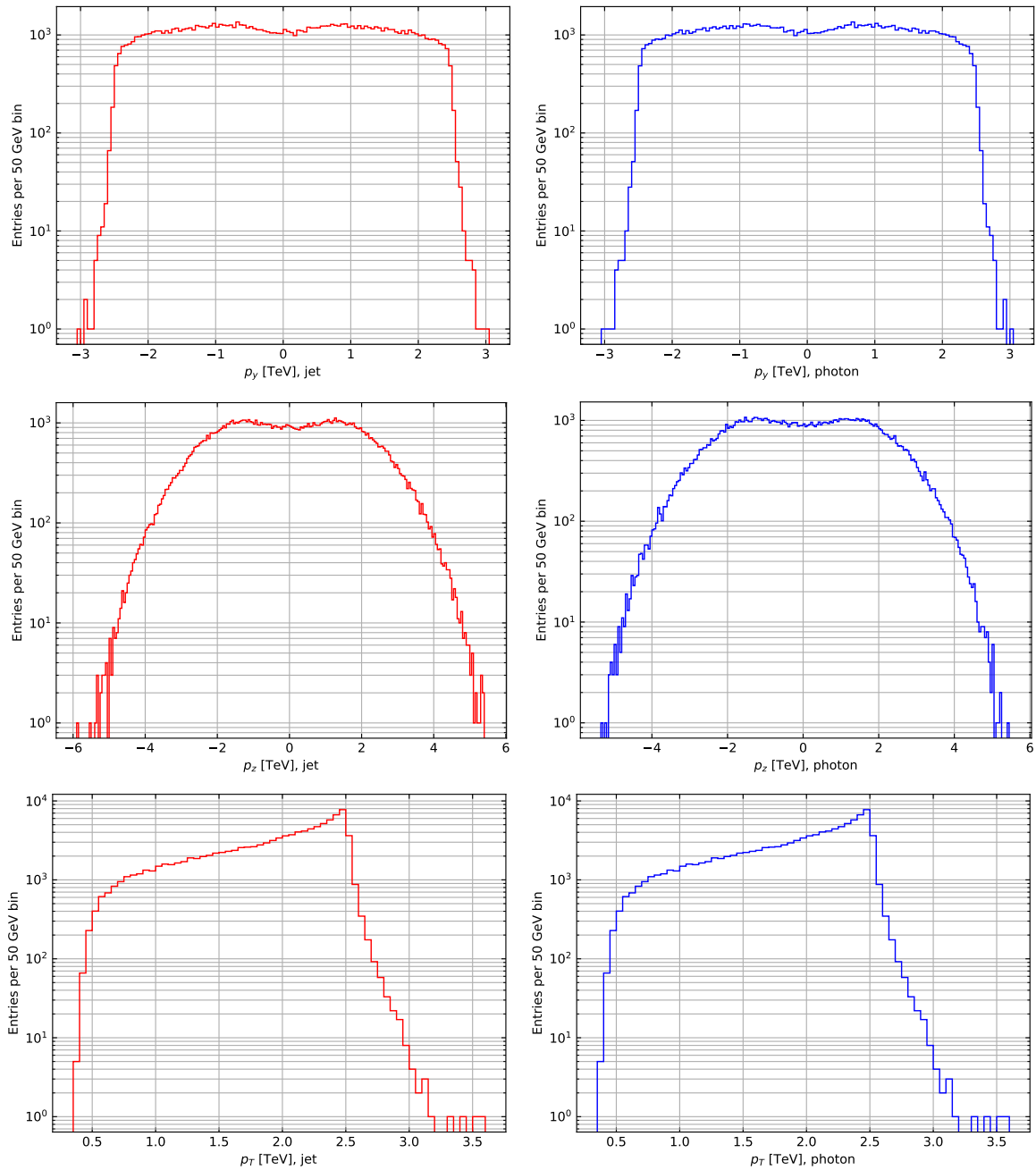
String Scale	$M_{cut}$ for 13 TeV	$M_{cut}$ for 13.6 TeV
5	4.17	4.15
5.5	4.64	4.61
6	5.12	5.09
6.5	5.61	5.58
7	6.12	6.08

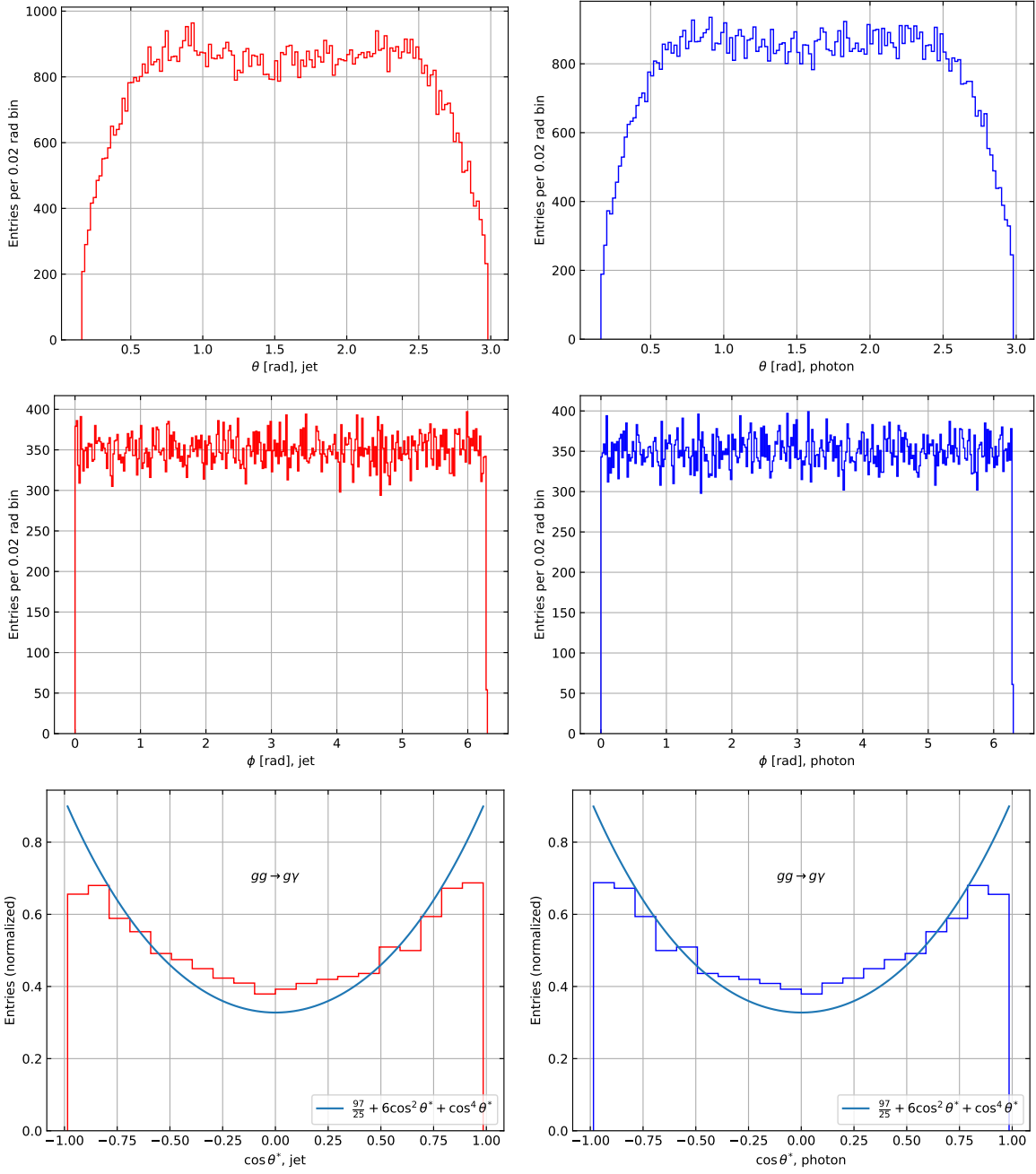
Table 6: Lower mass cuts for each  $M_s$ ,  $\sqrt{s}$

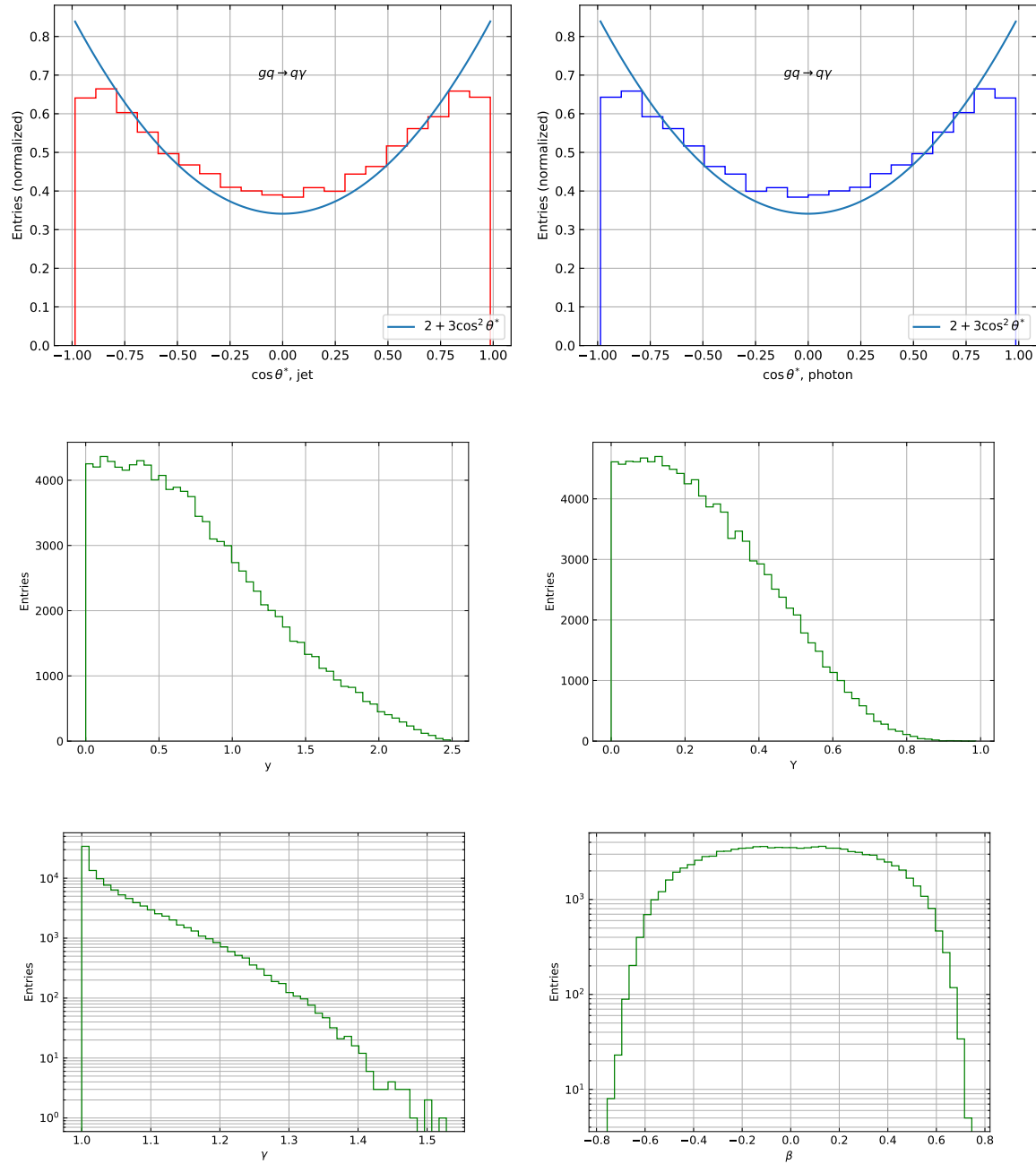
## 9.4 Kinematic Data Histograms

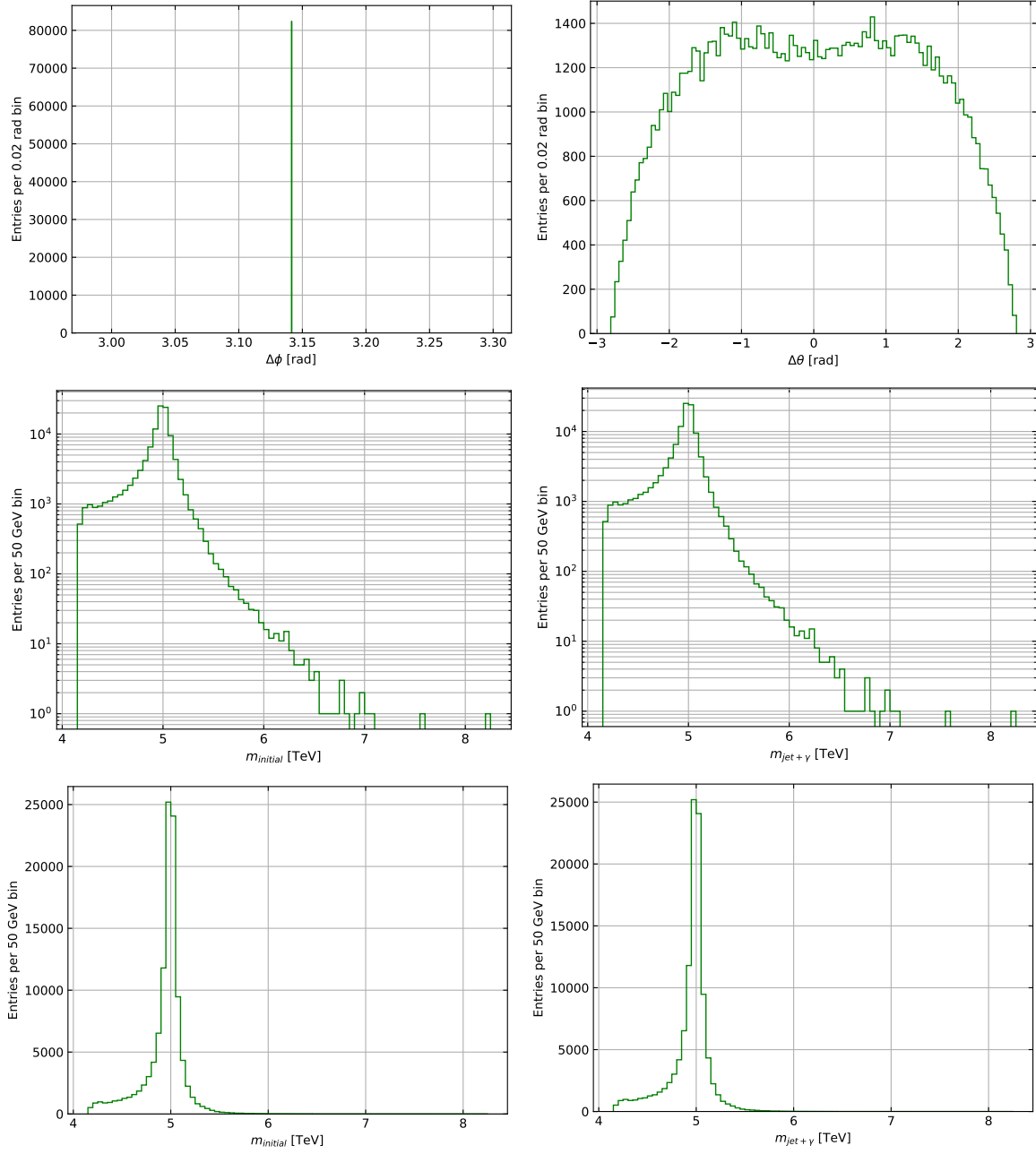
9.4.1  $\sqrt{s} = 13 \text{ TeV}, M_s = 5 \text{ TeV}$



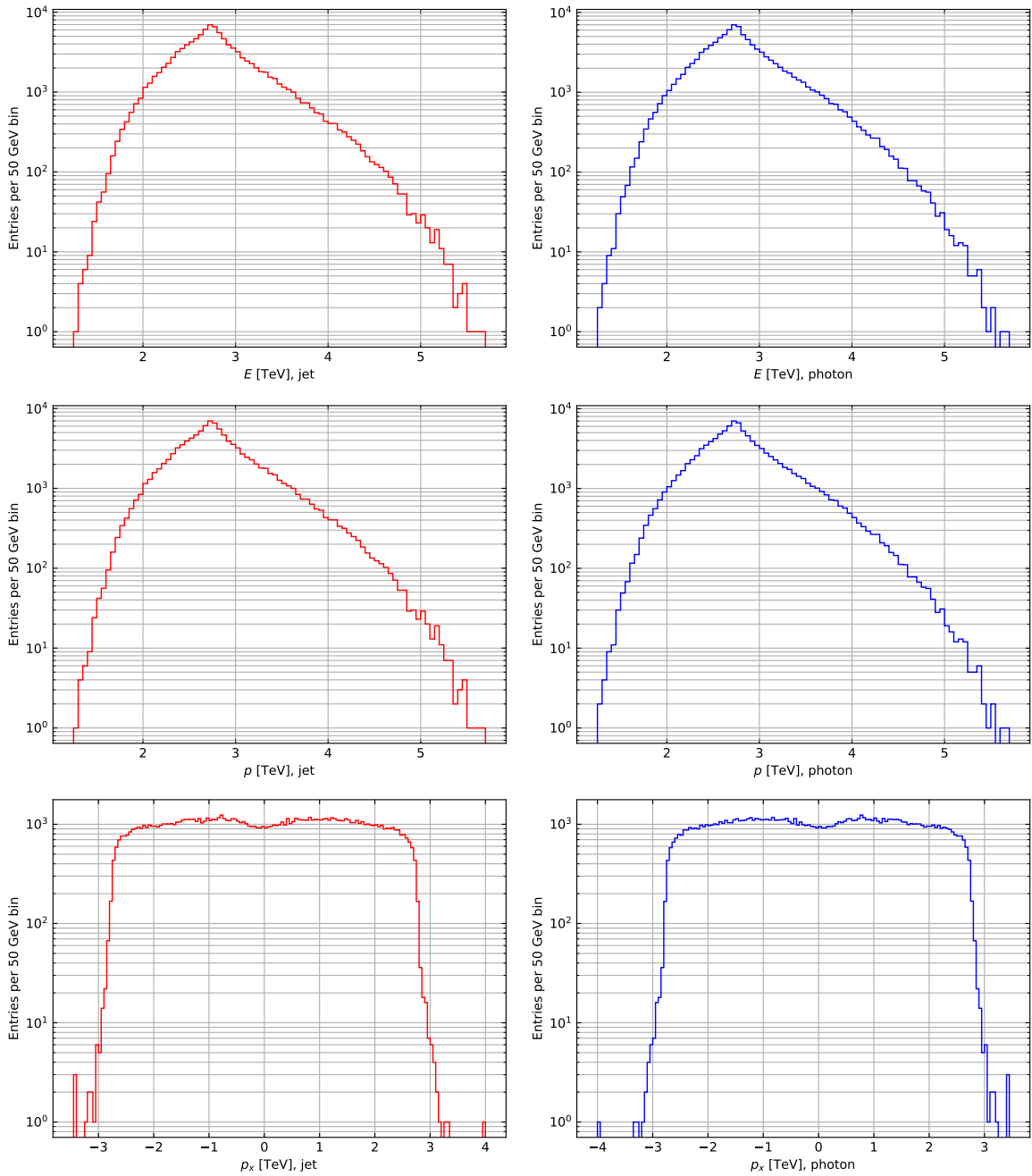


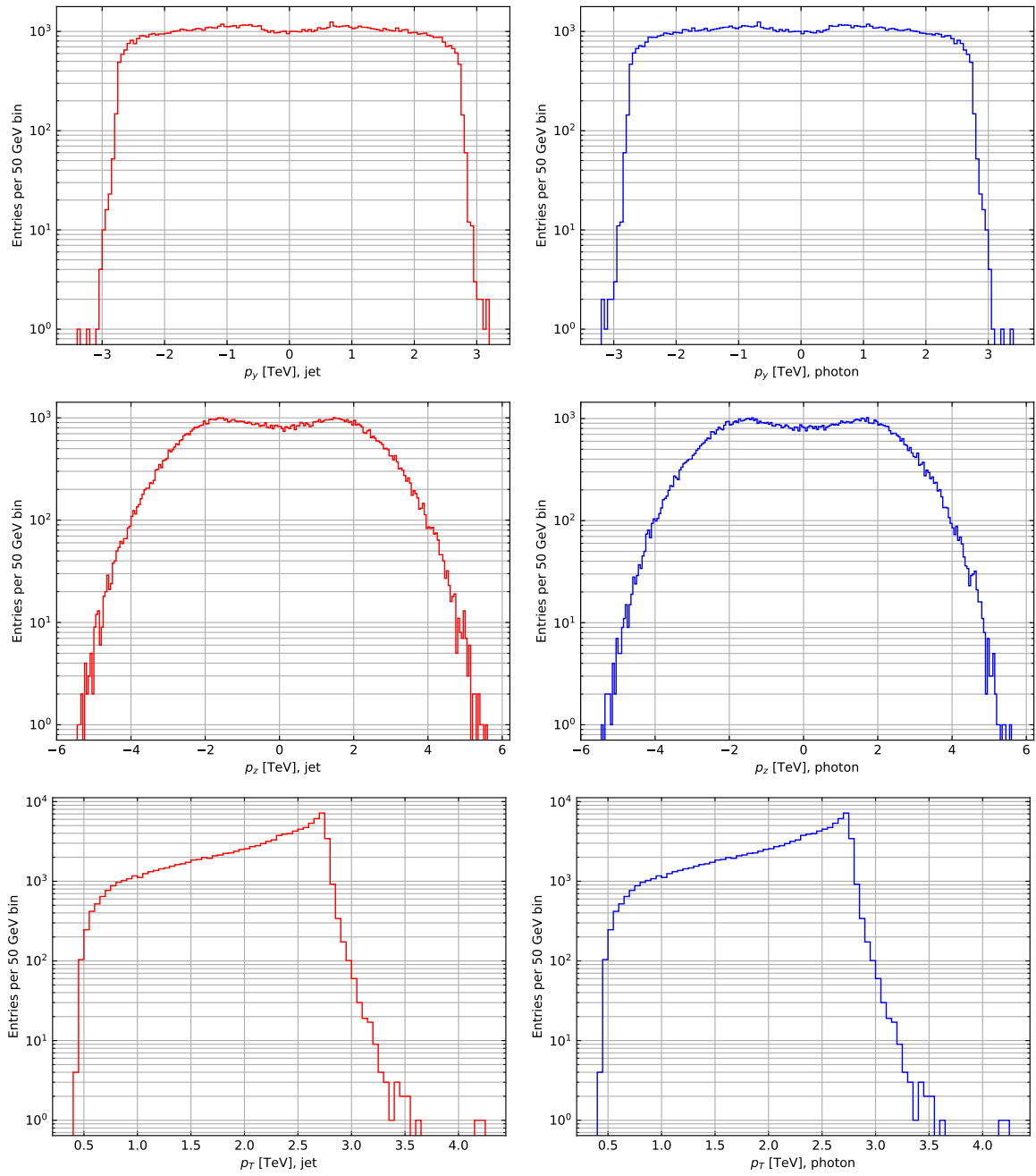


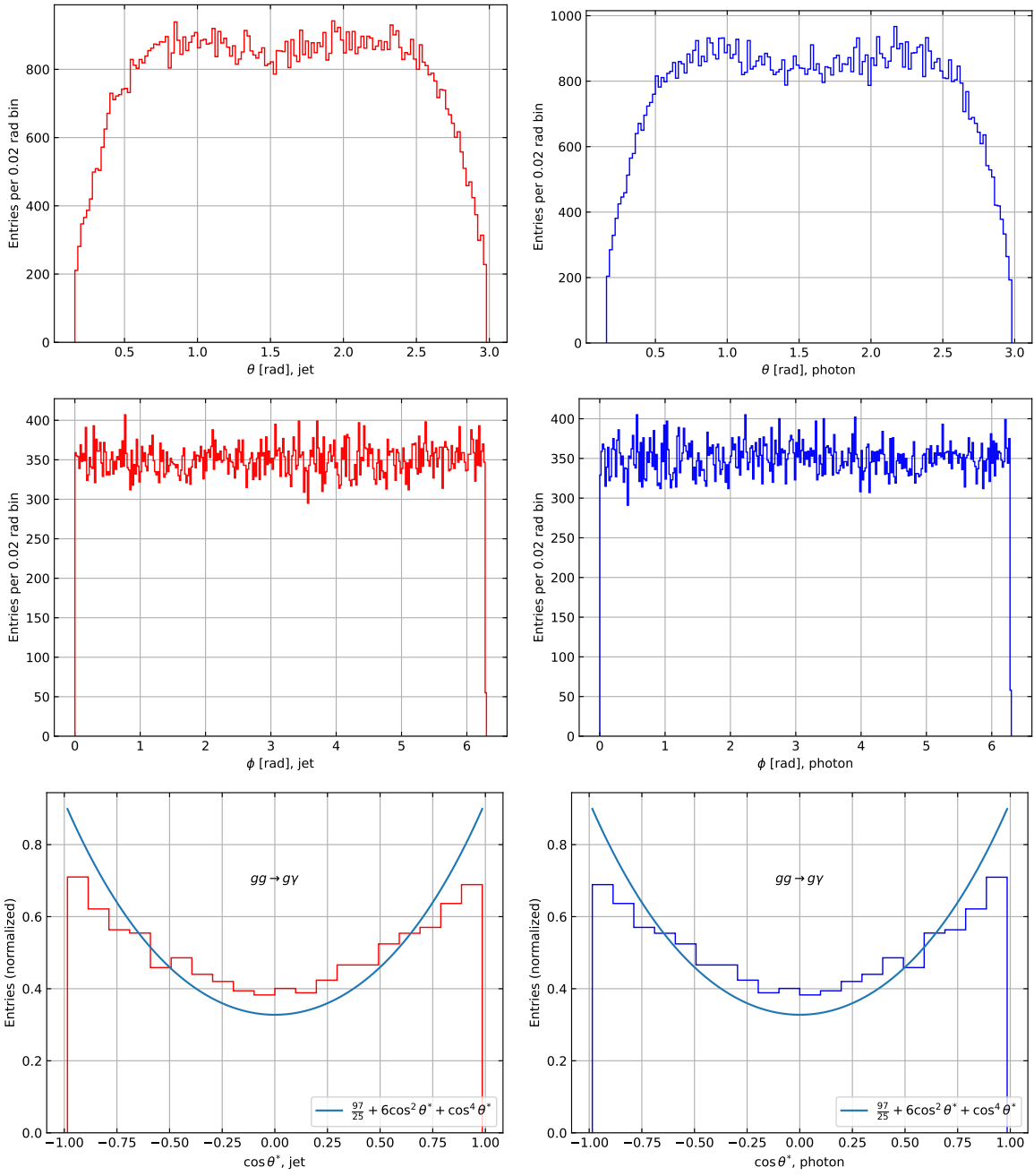


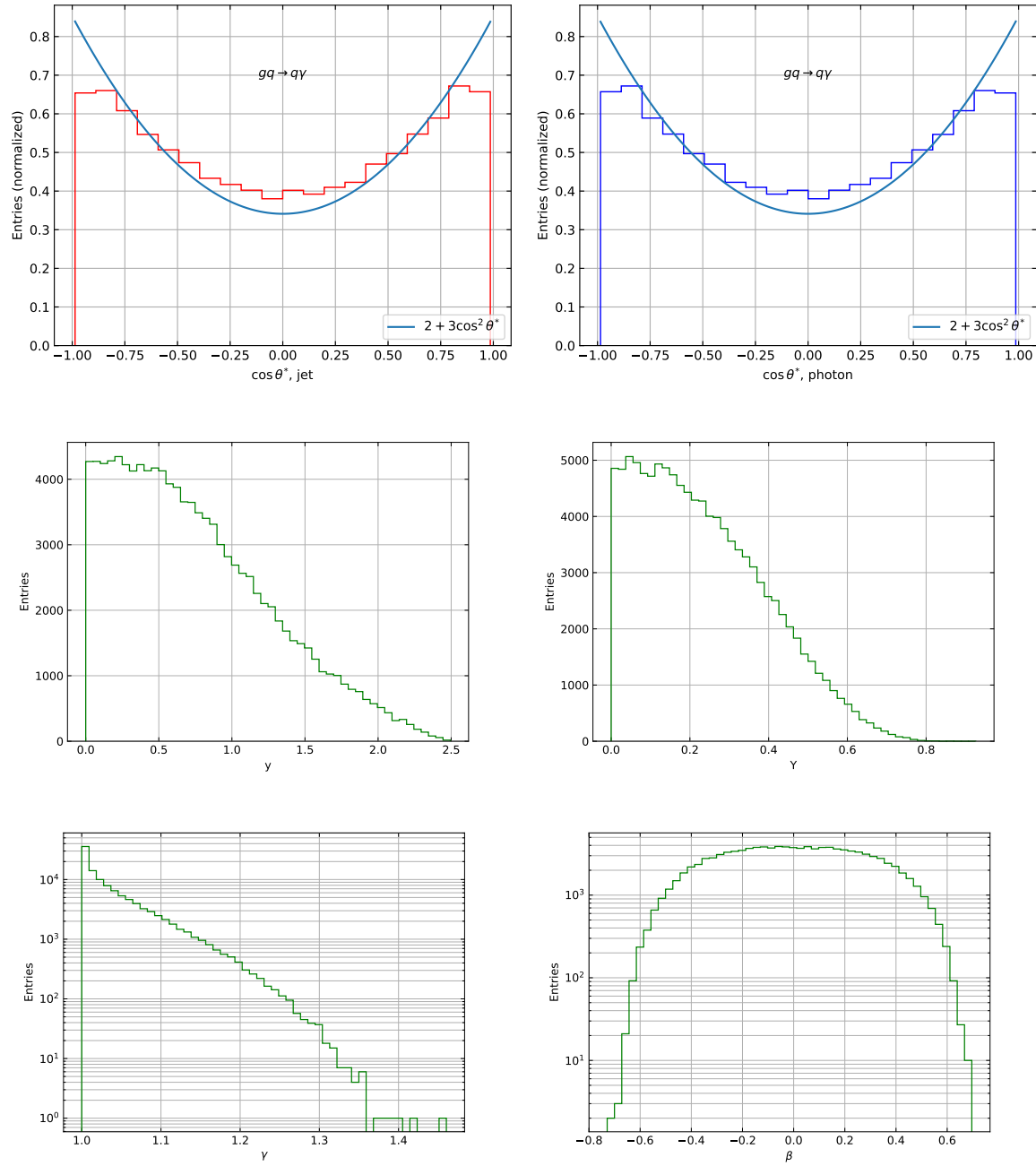


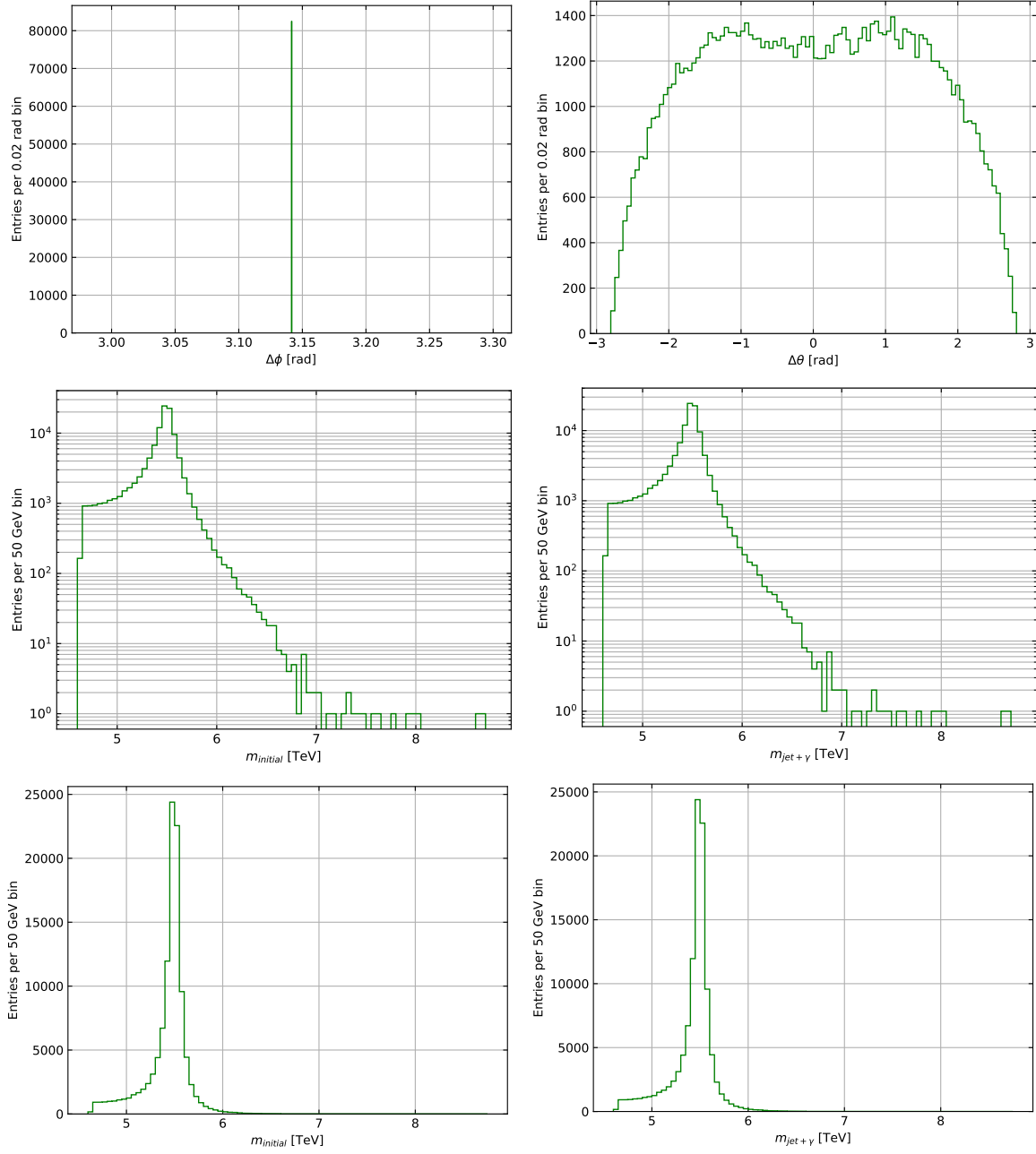
#### 9.4.2 $\sqrt{s} = 13$ TeV, $M_s = 5.5$ TeV



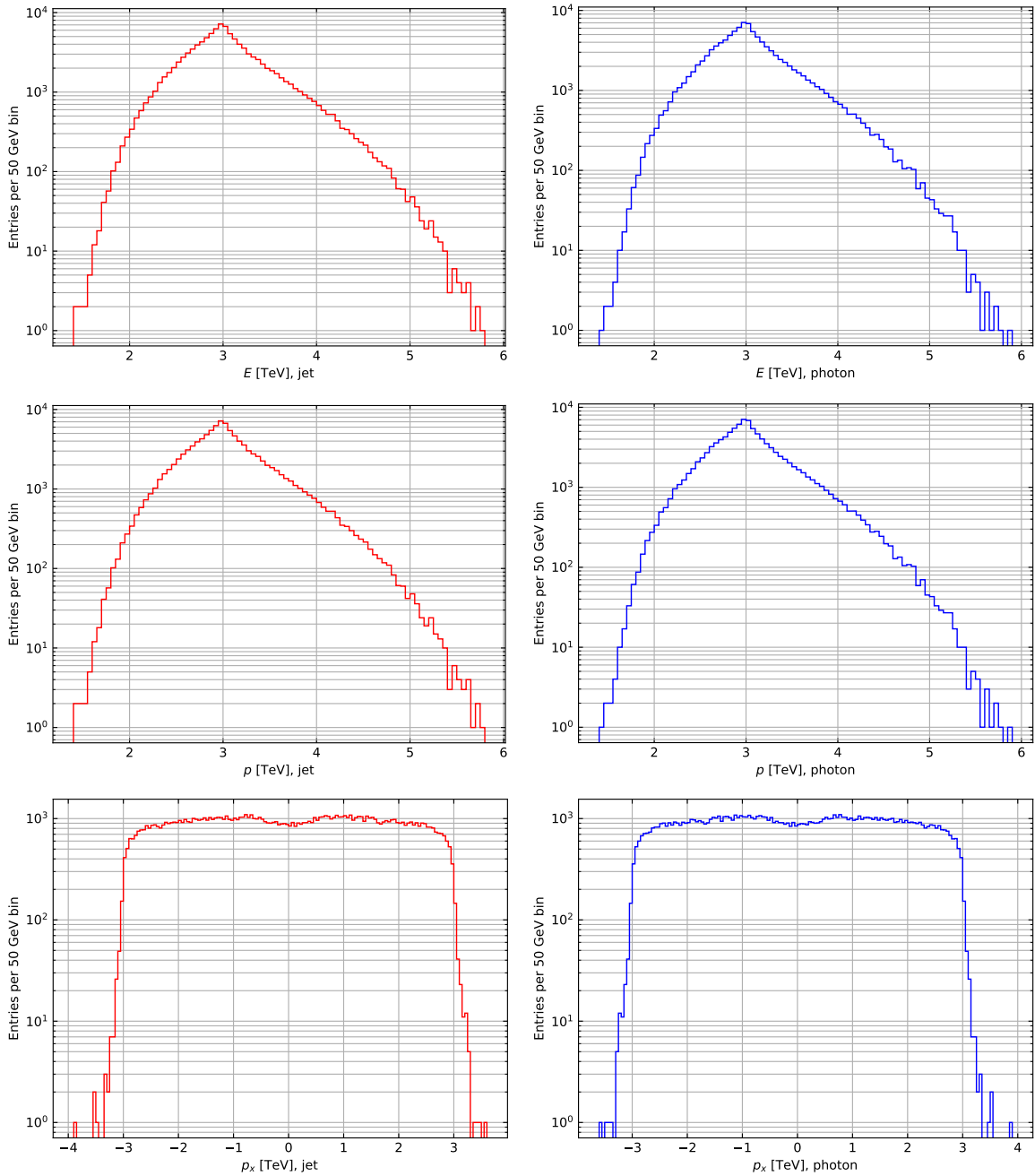


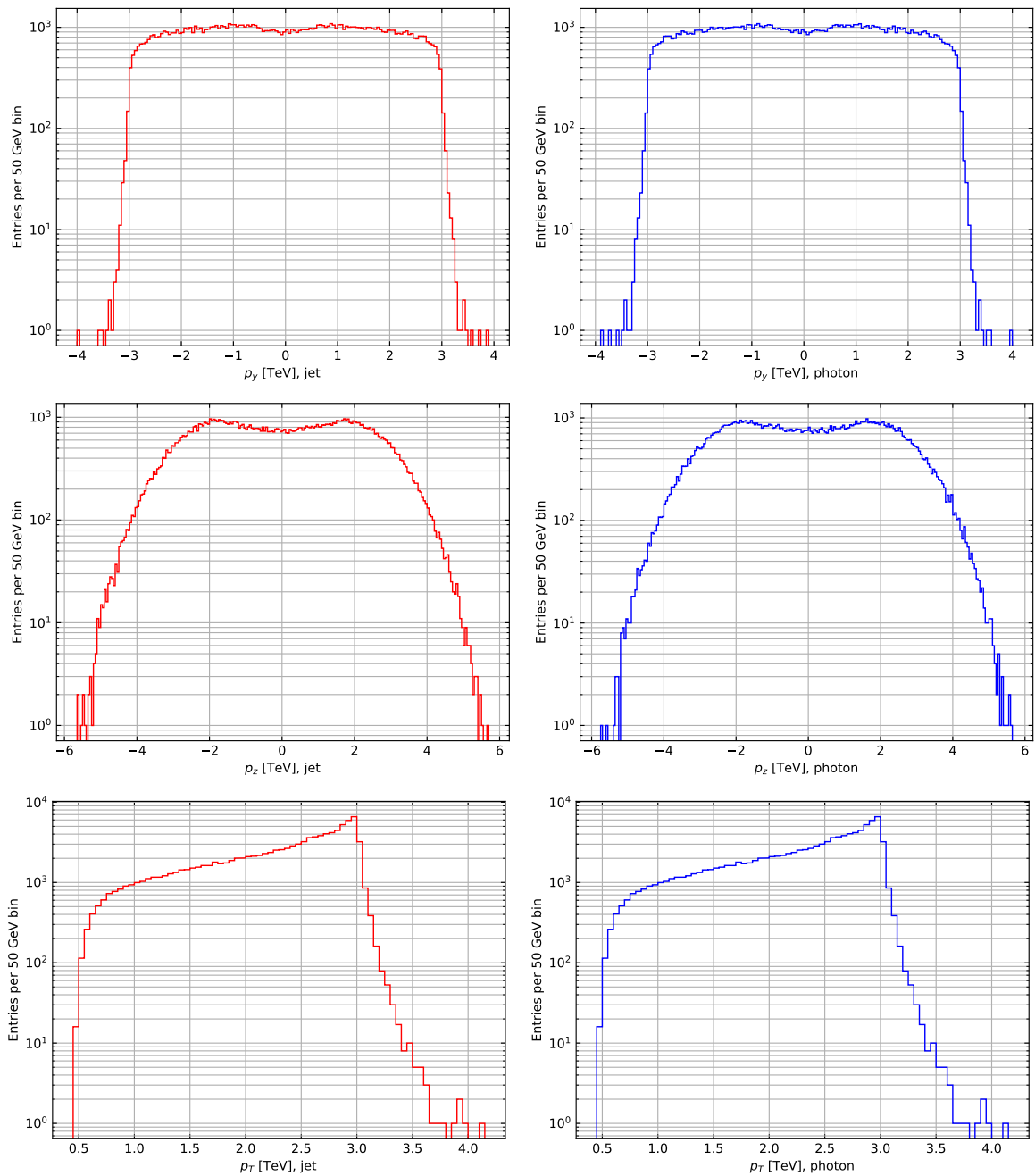


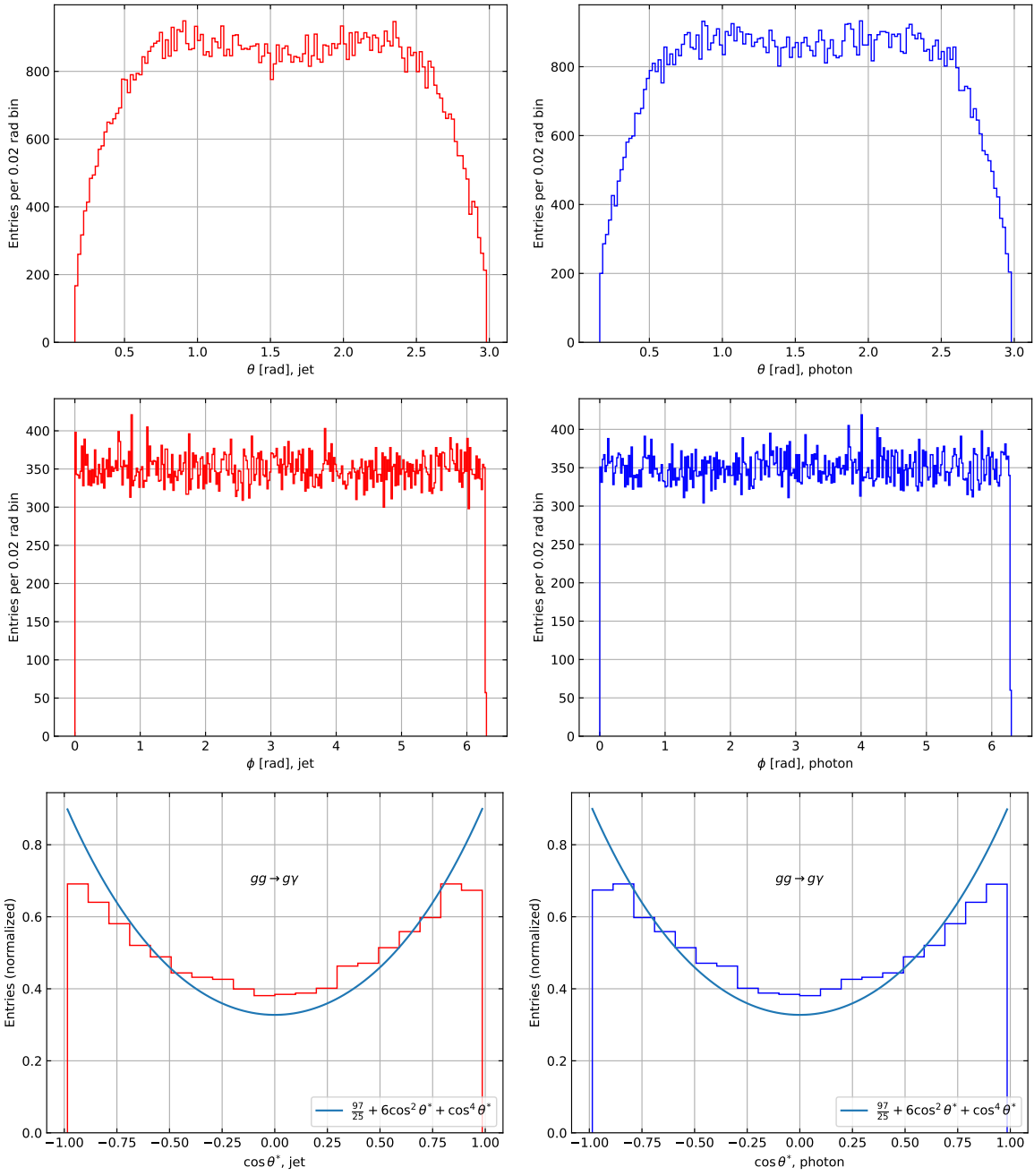


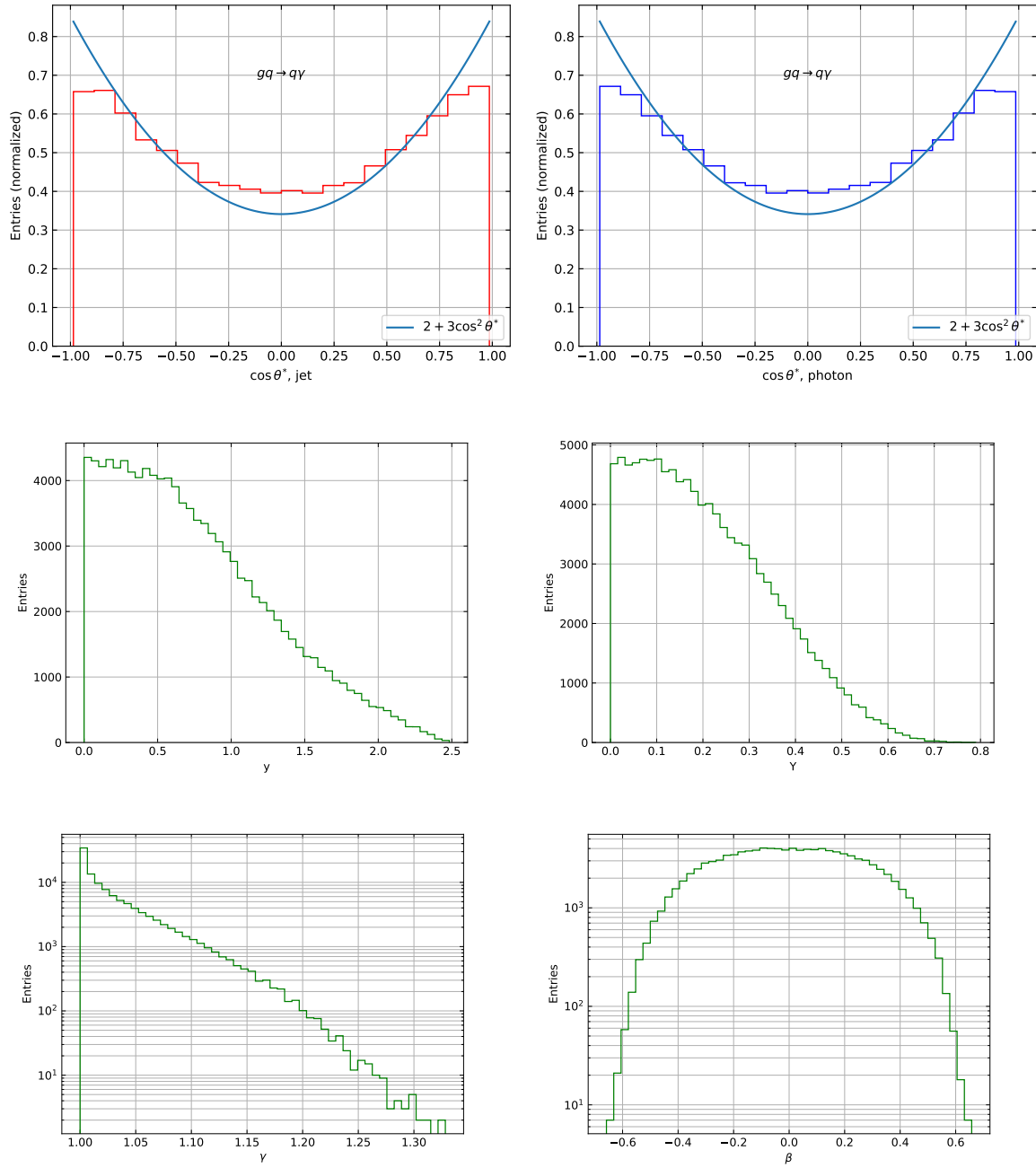


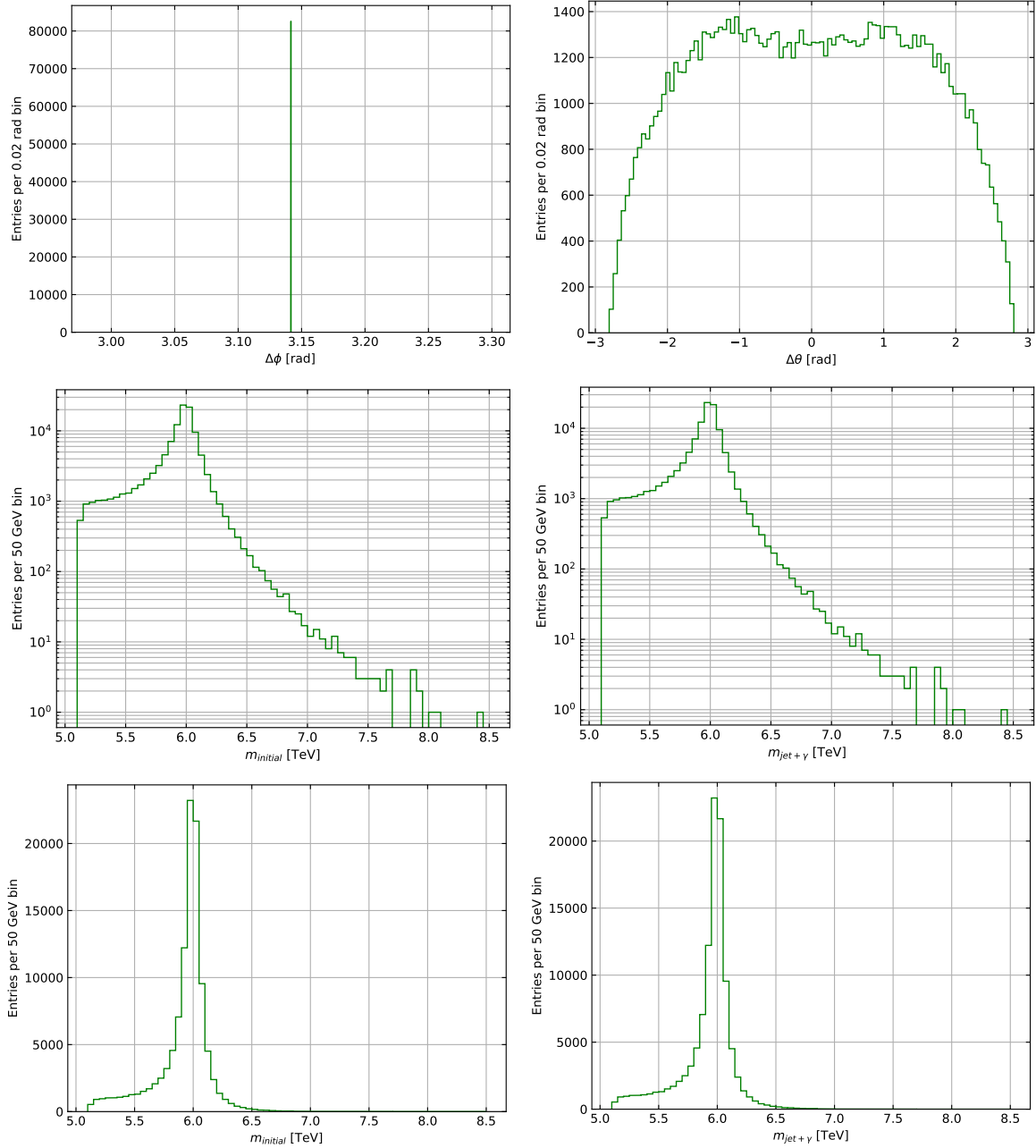
### 9.4.3 $\sqrt{s} = 13$ TeV, $M_s = 6$ TeV



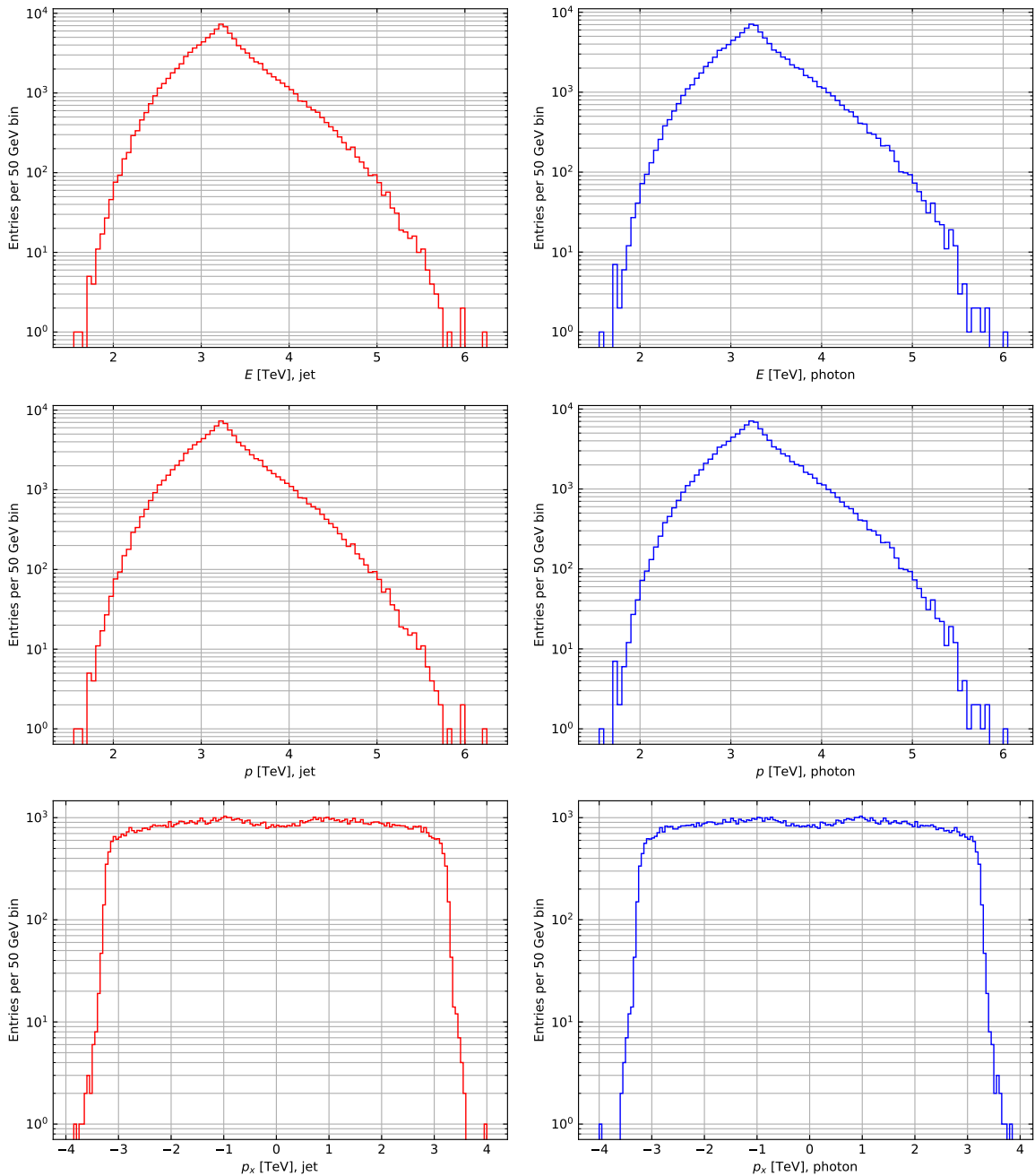


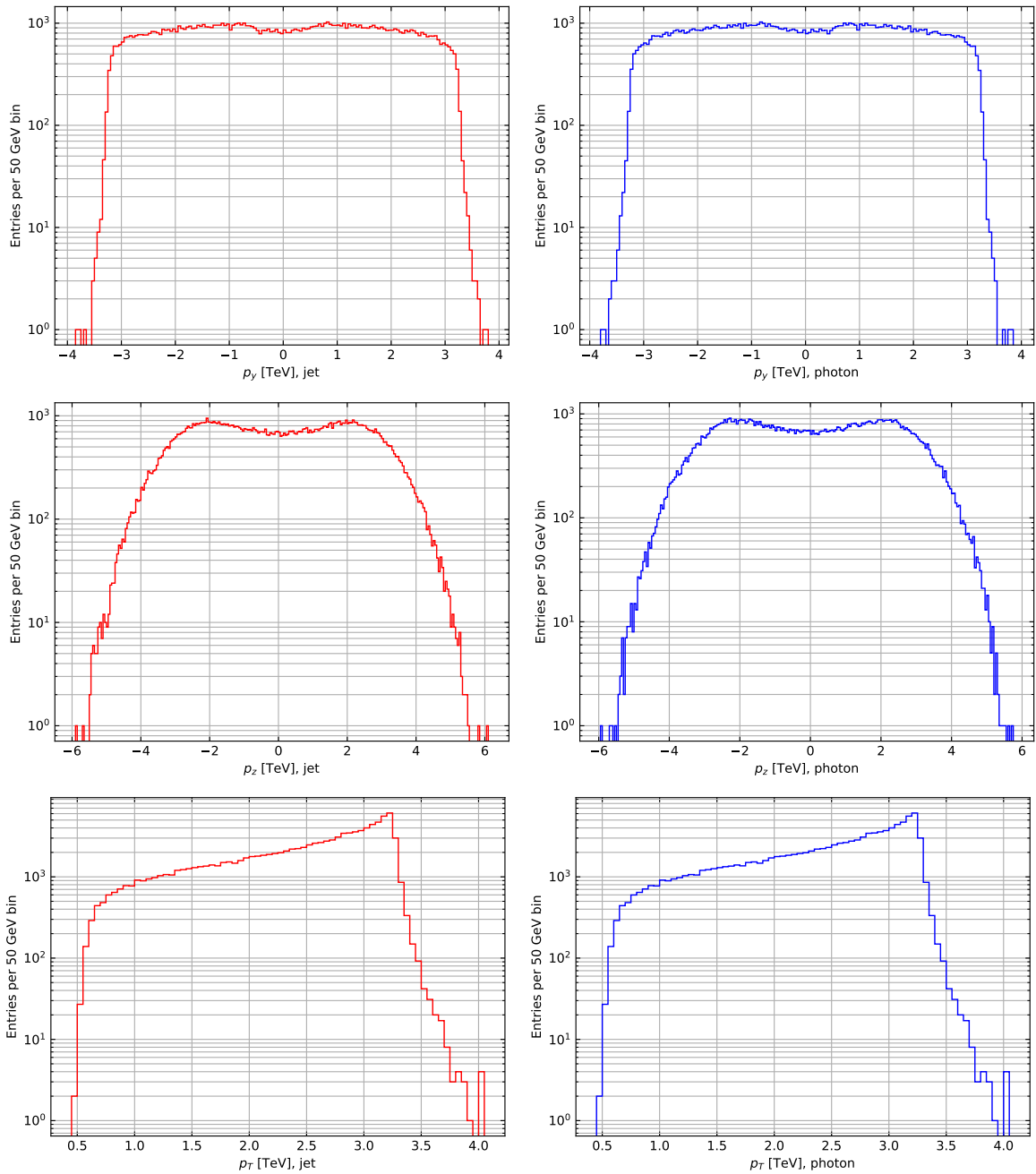


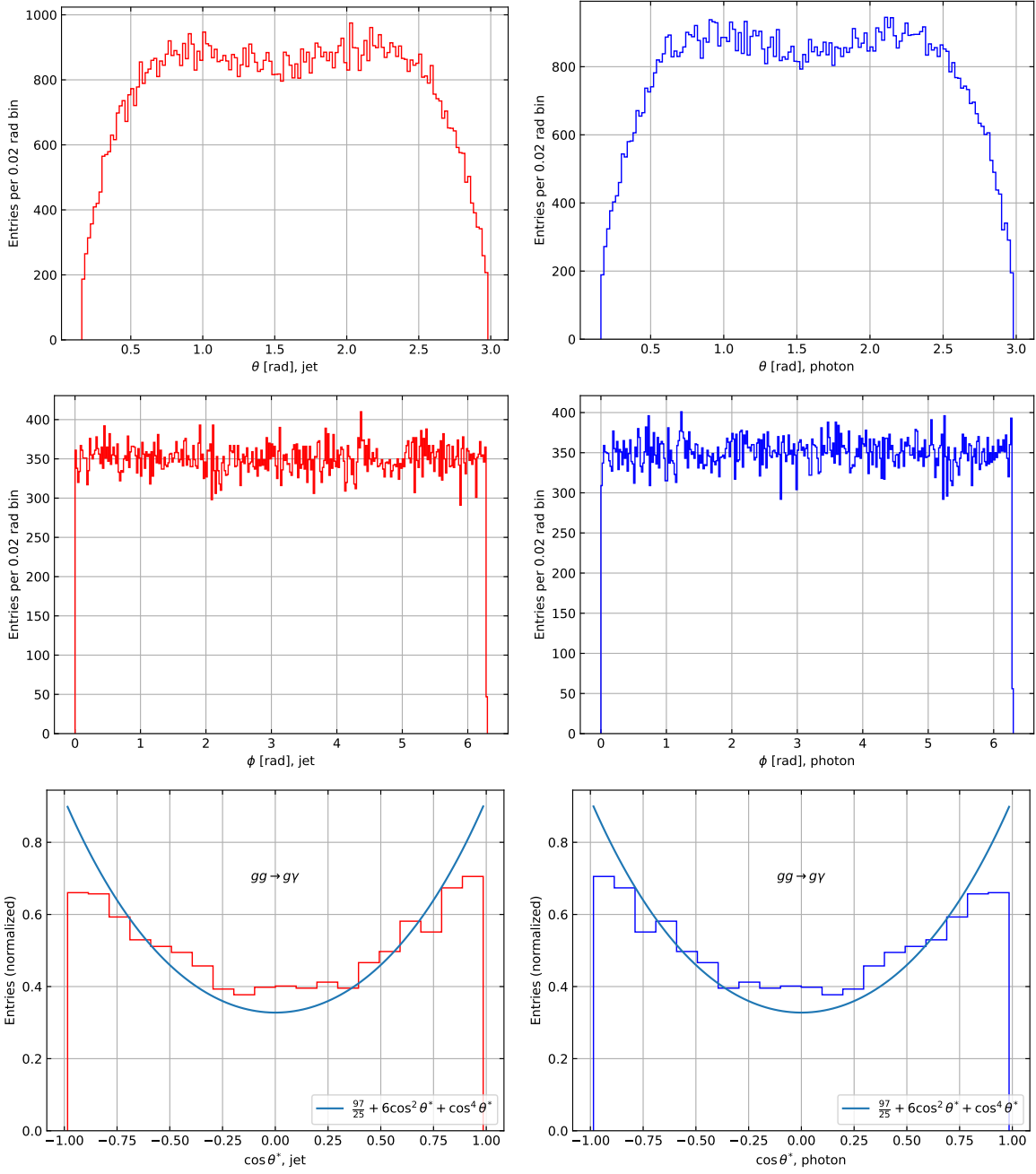


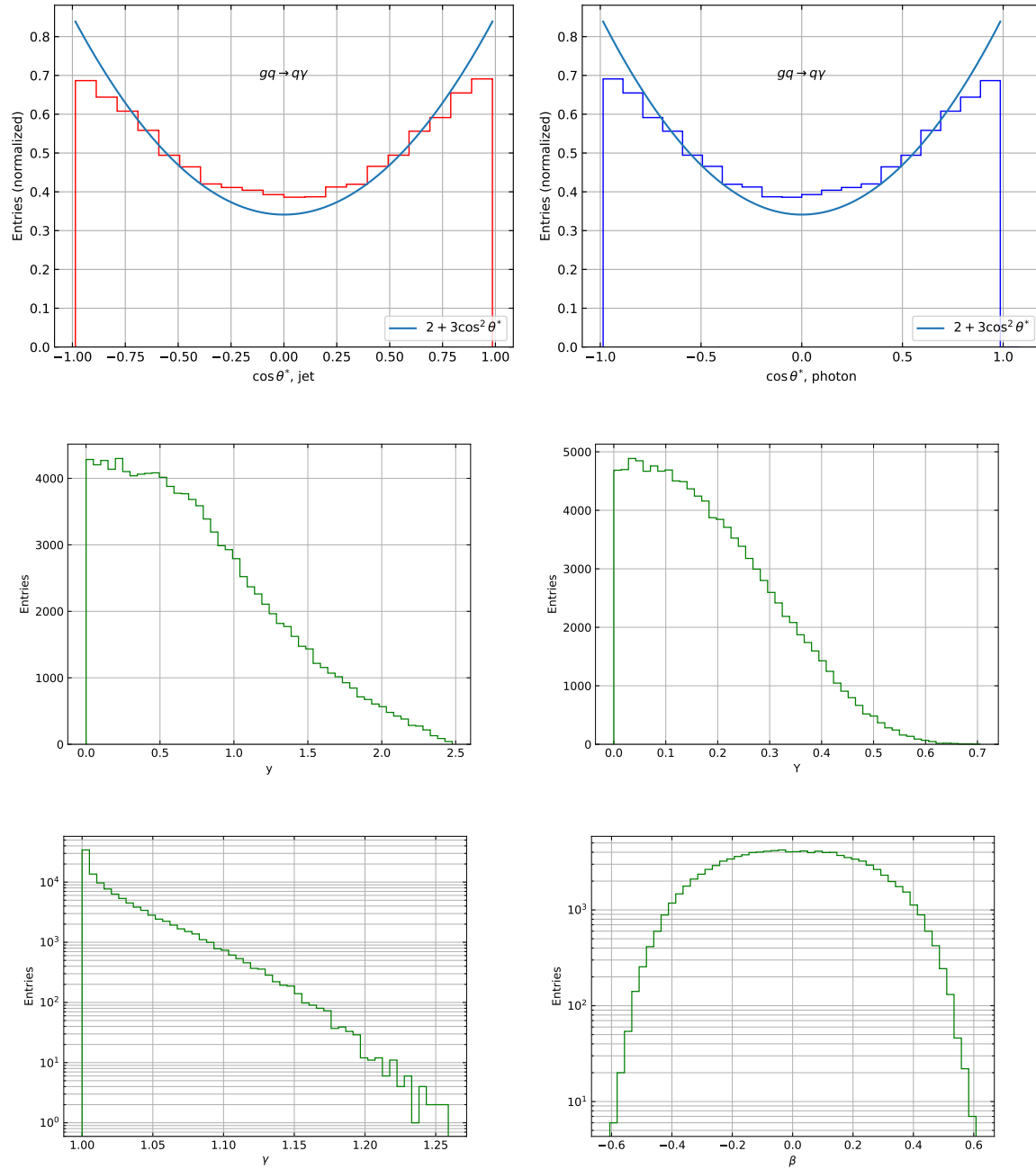


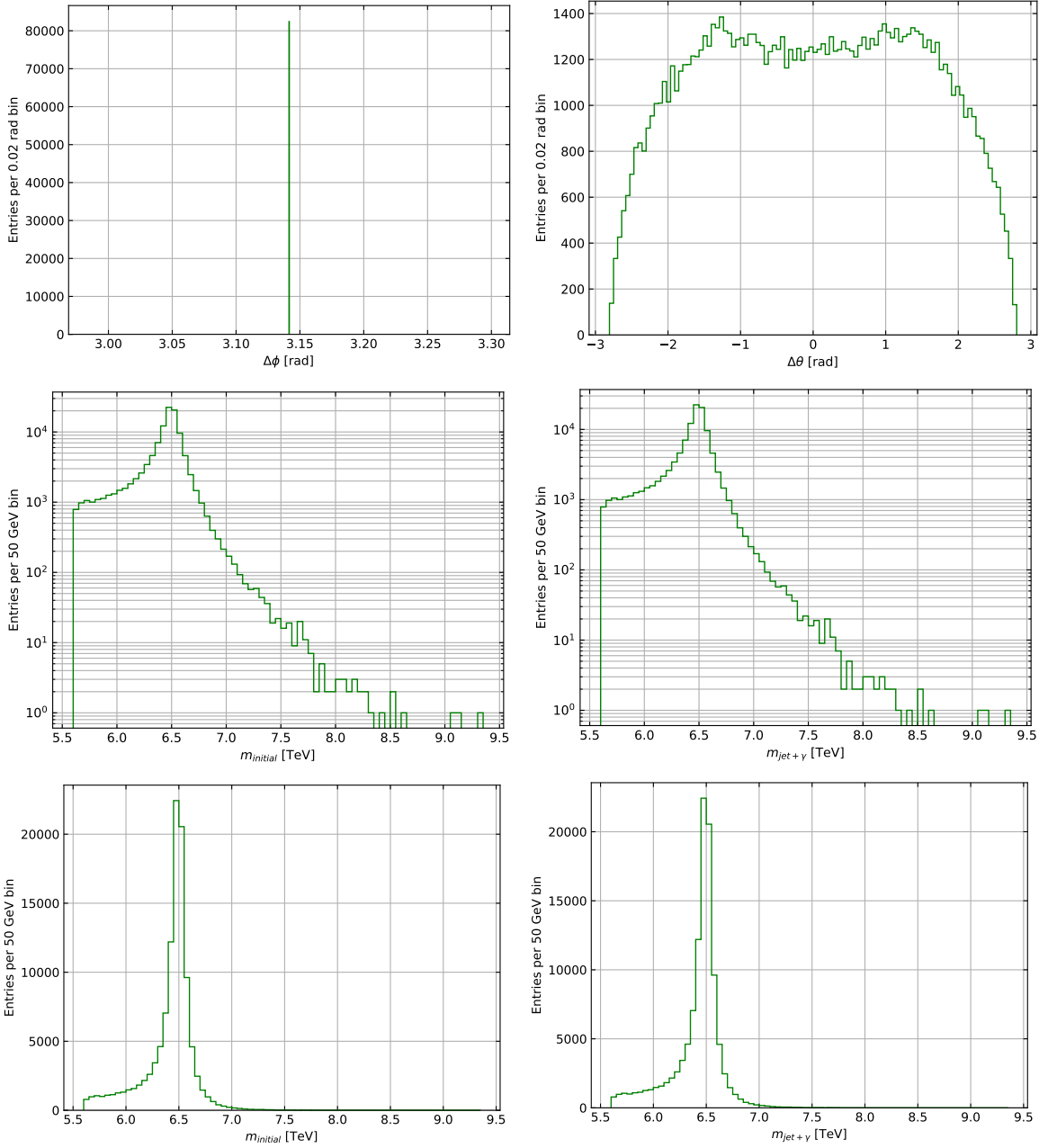
#### 9.4.4 $\sqrt{s} = 13$ TeV, $M_s = 6.5$ TeV



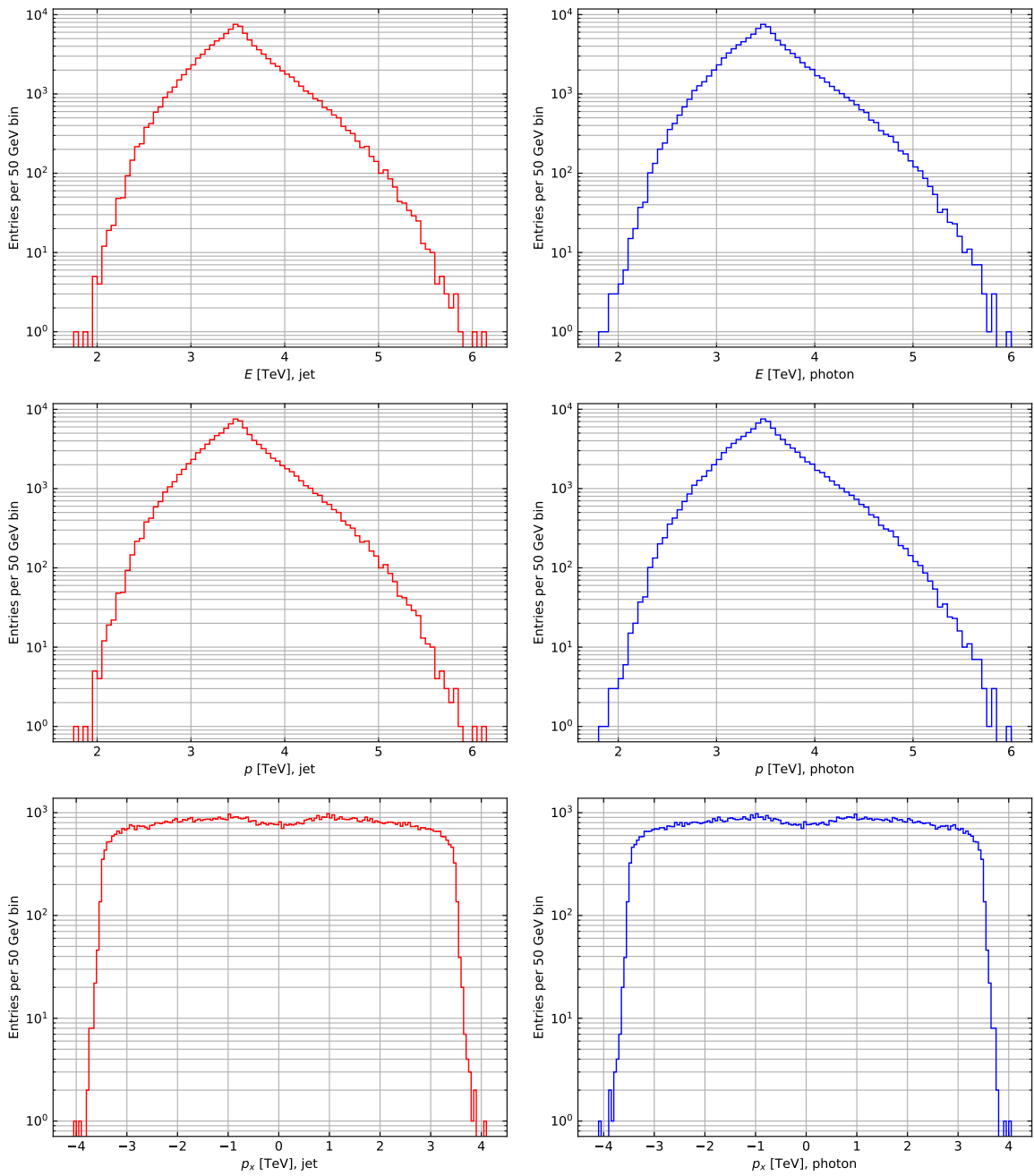


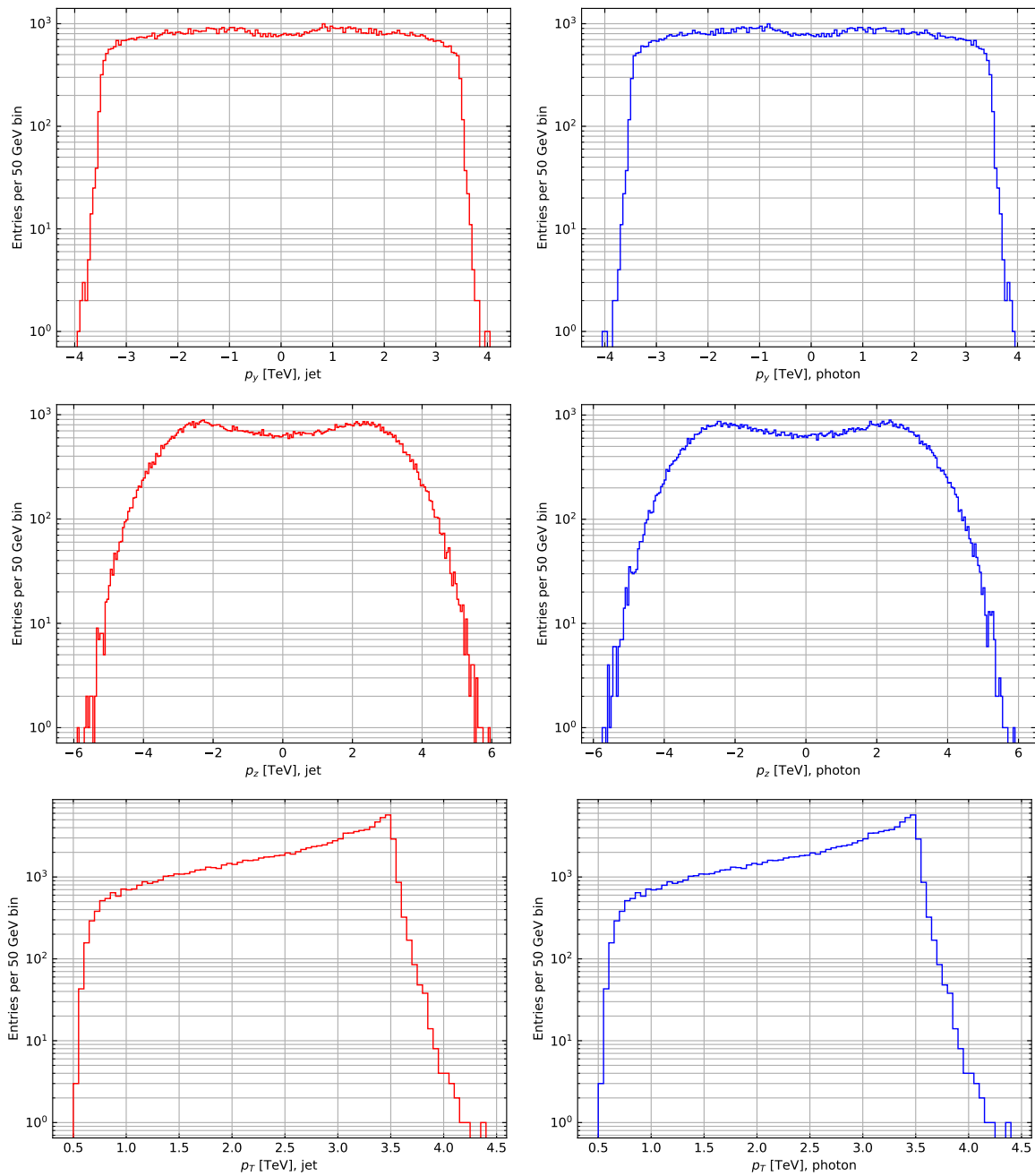


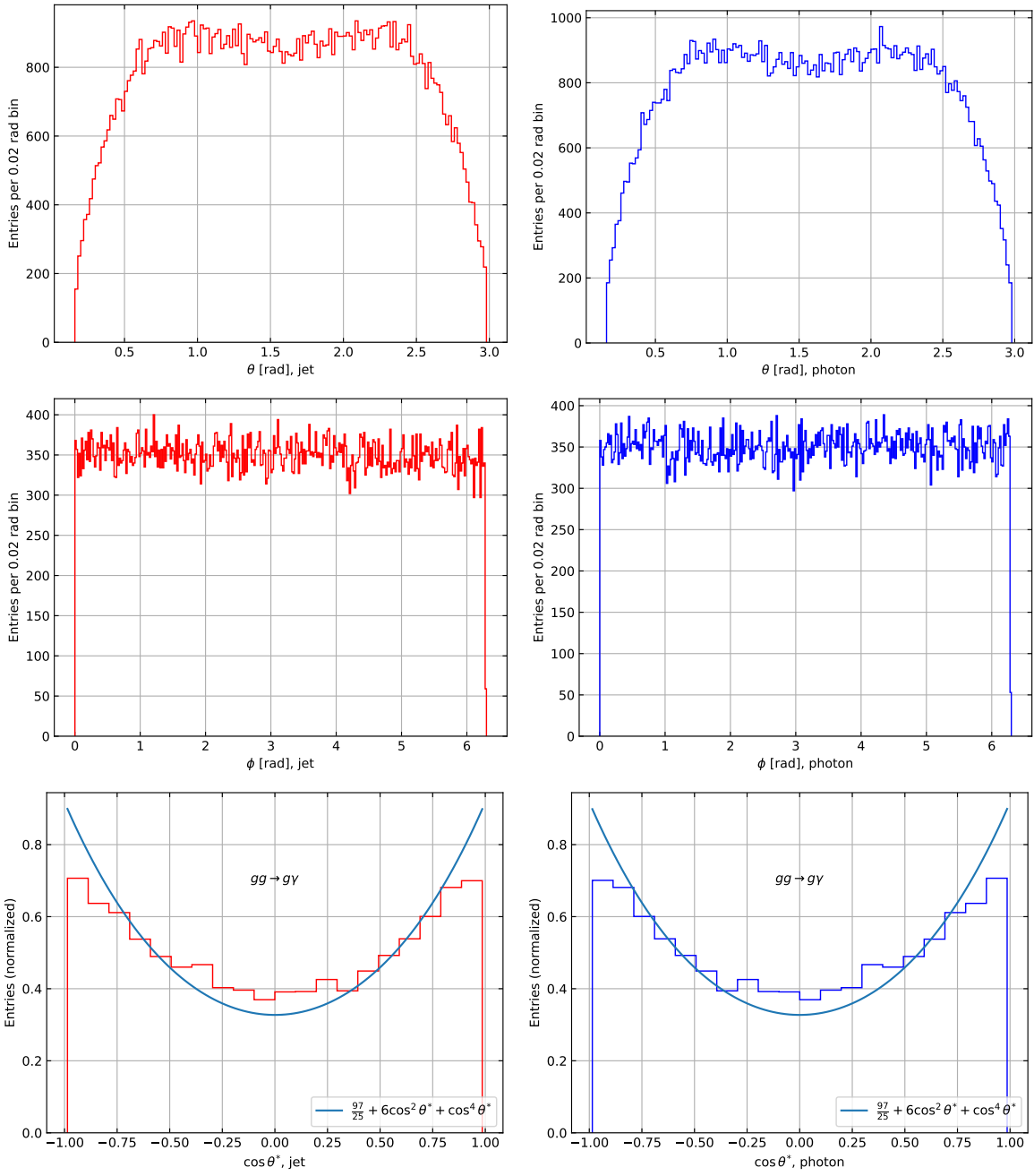


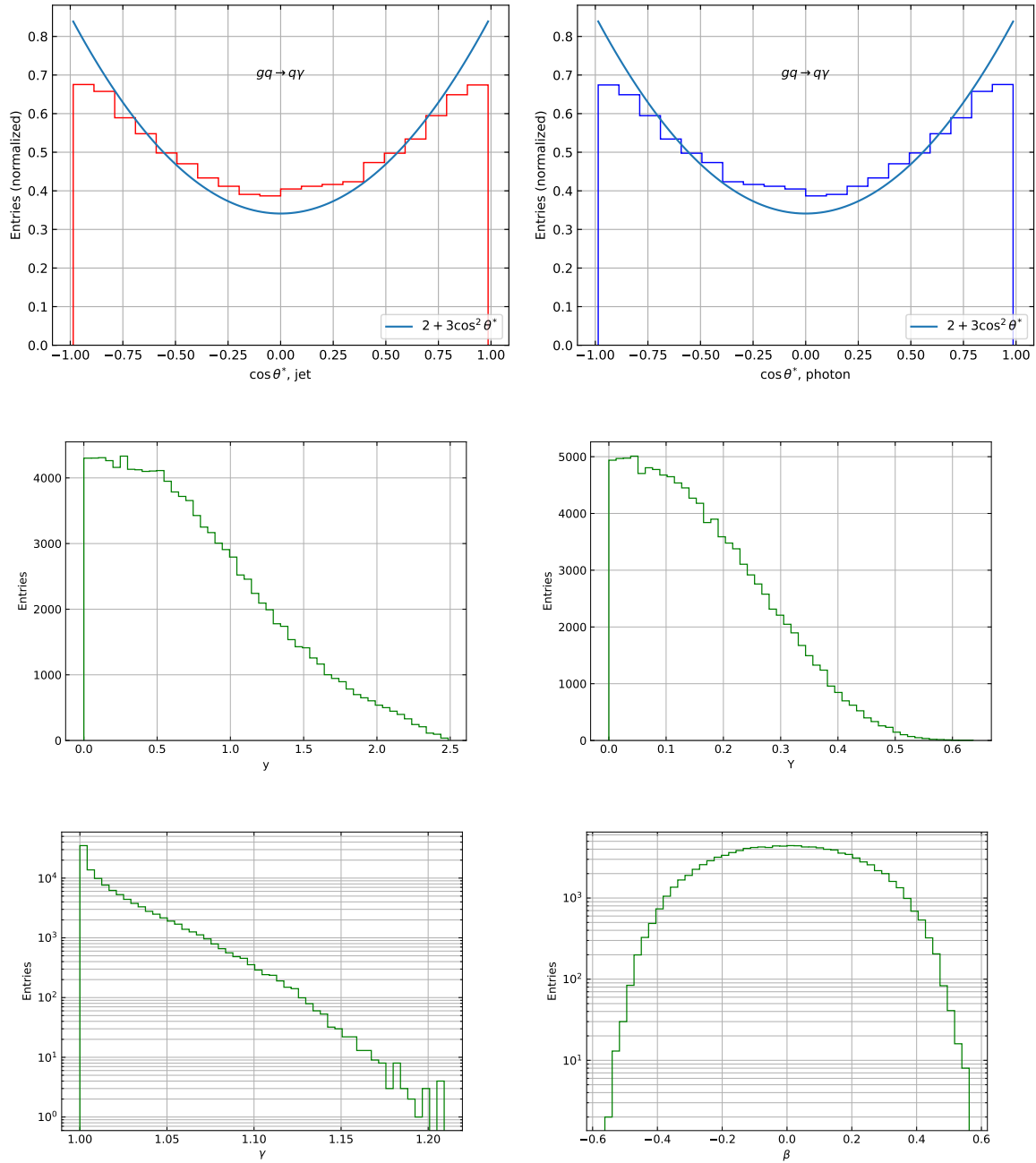


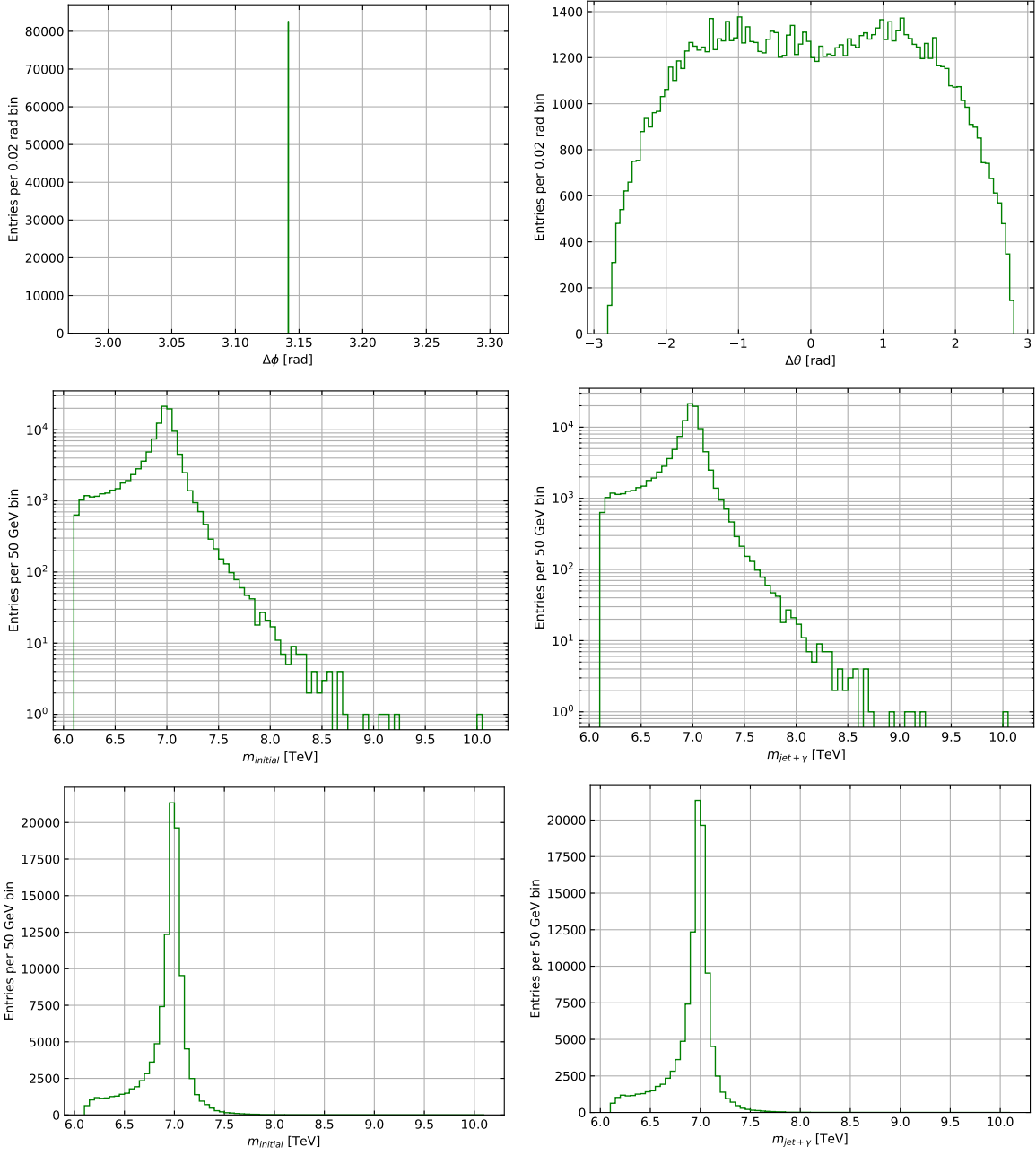
#### 9.4.5 $\sqrt{s} = 13$ TeV, $M_s = 7$ TeV



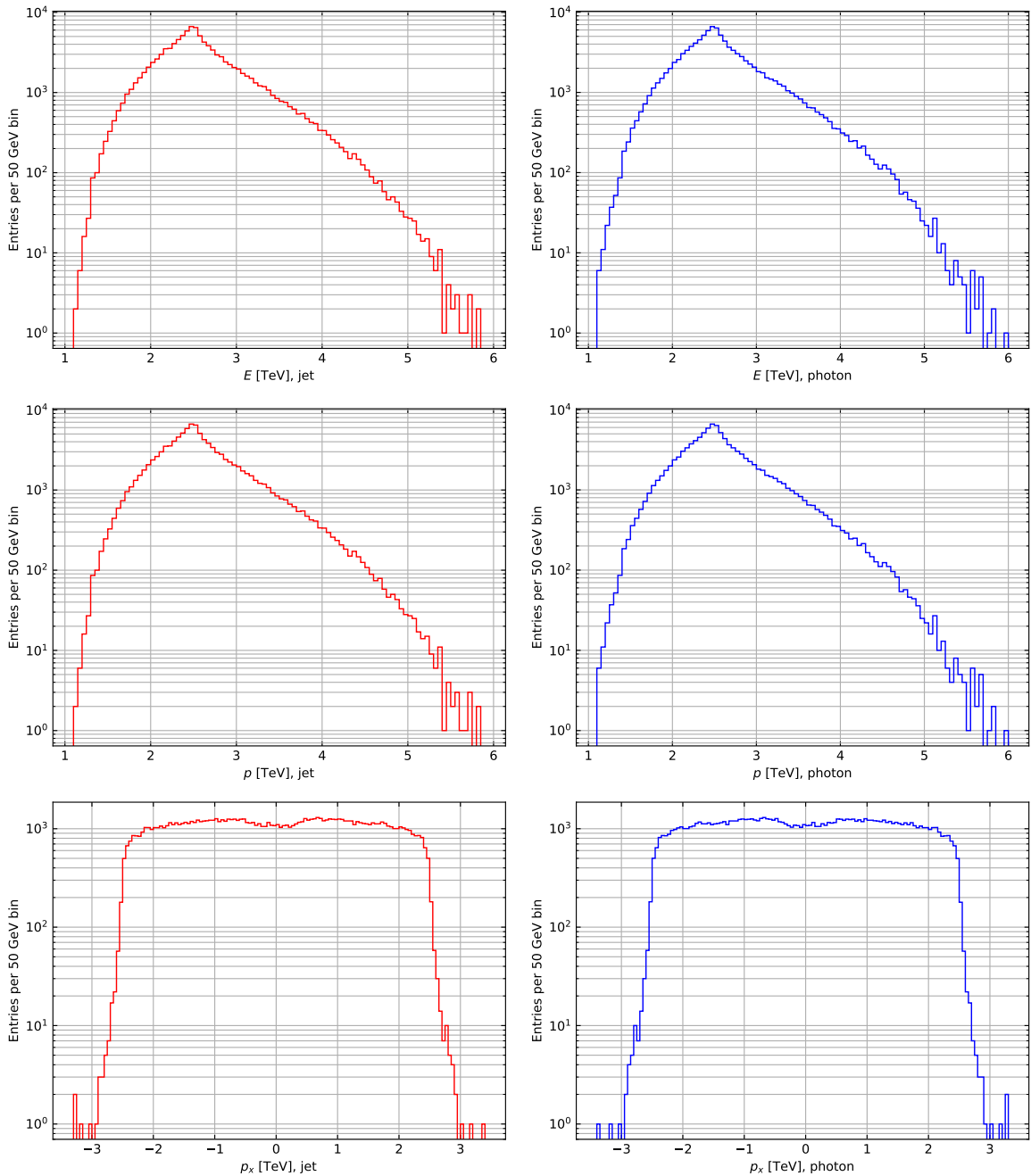


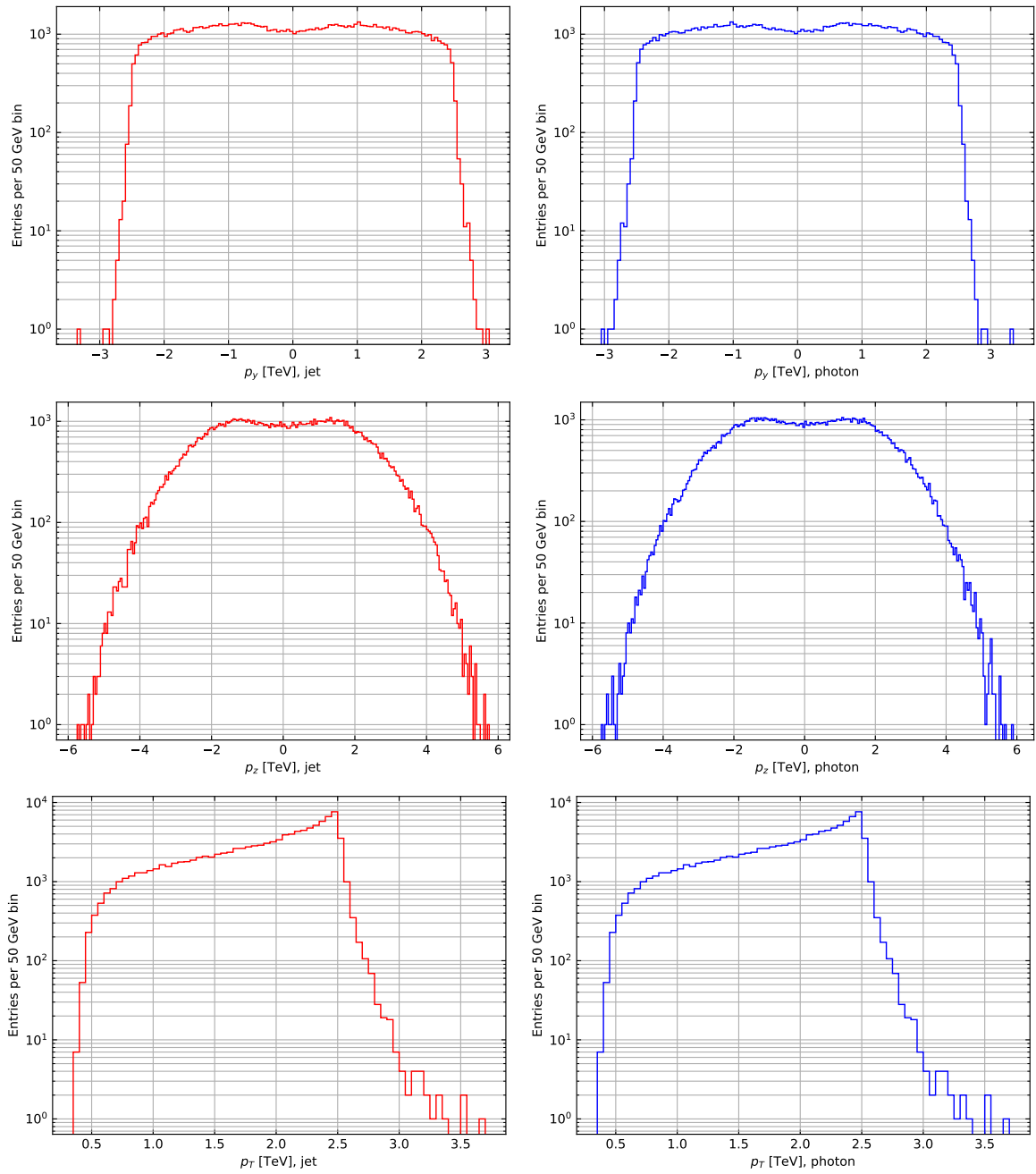


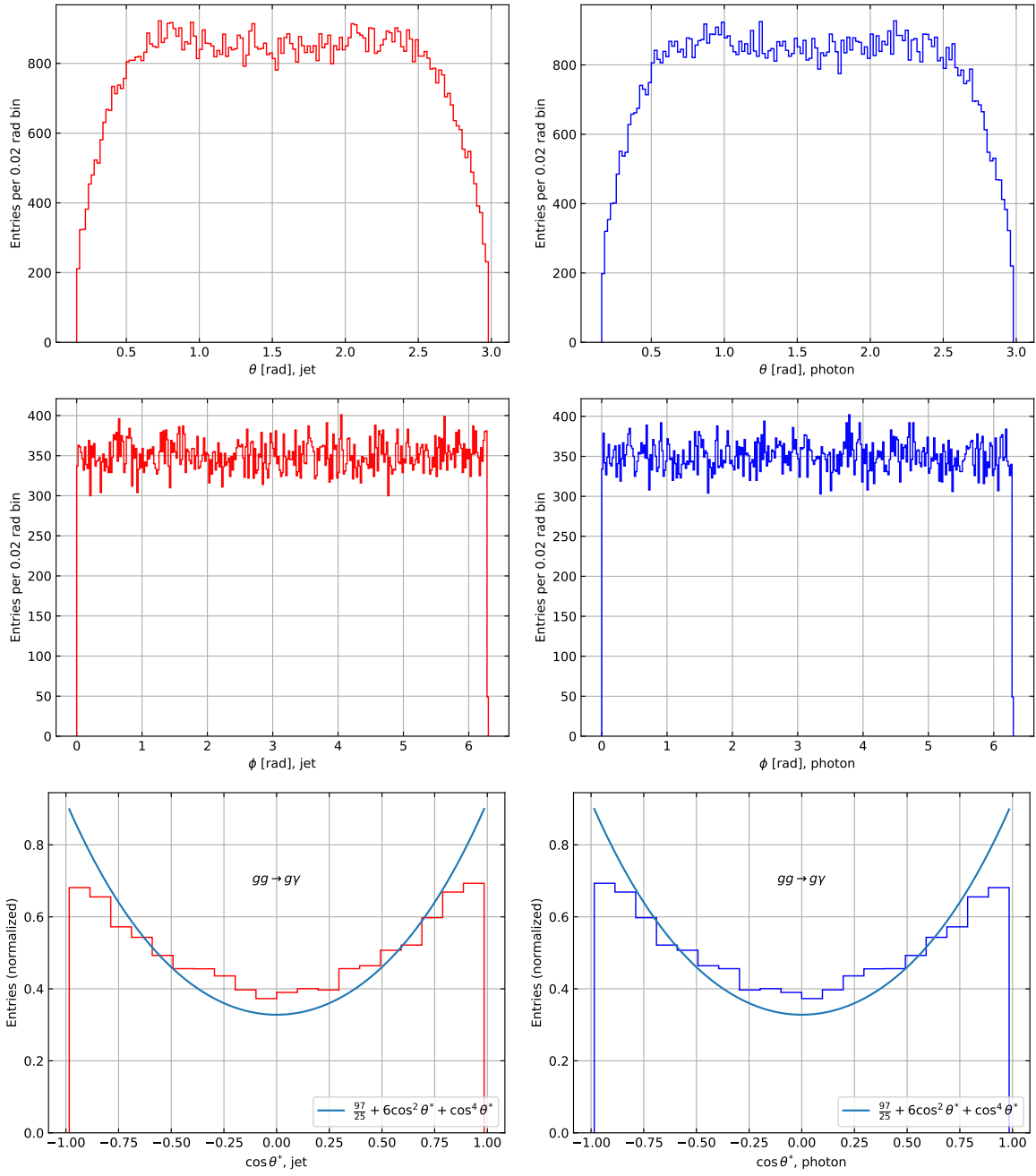


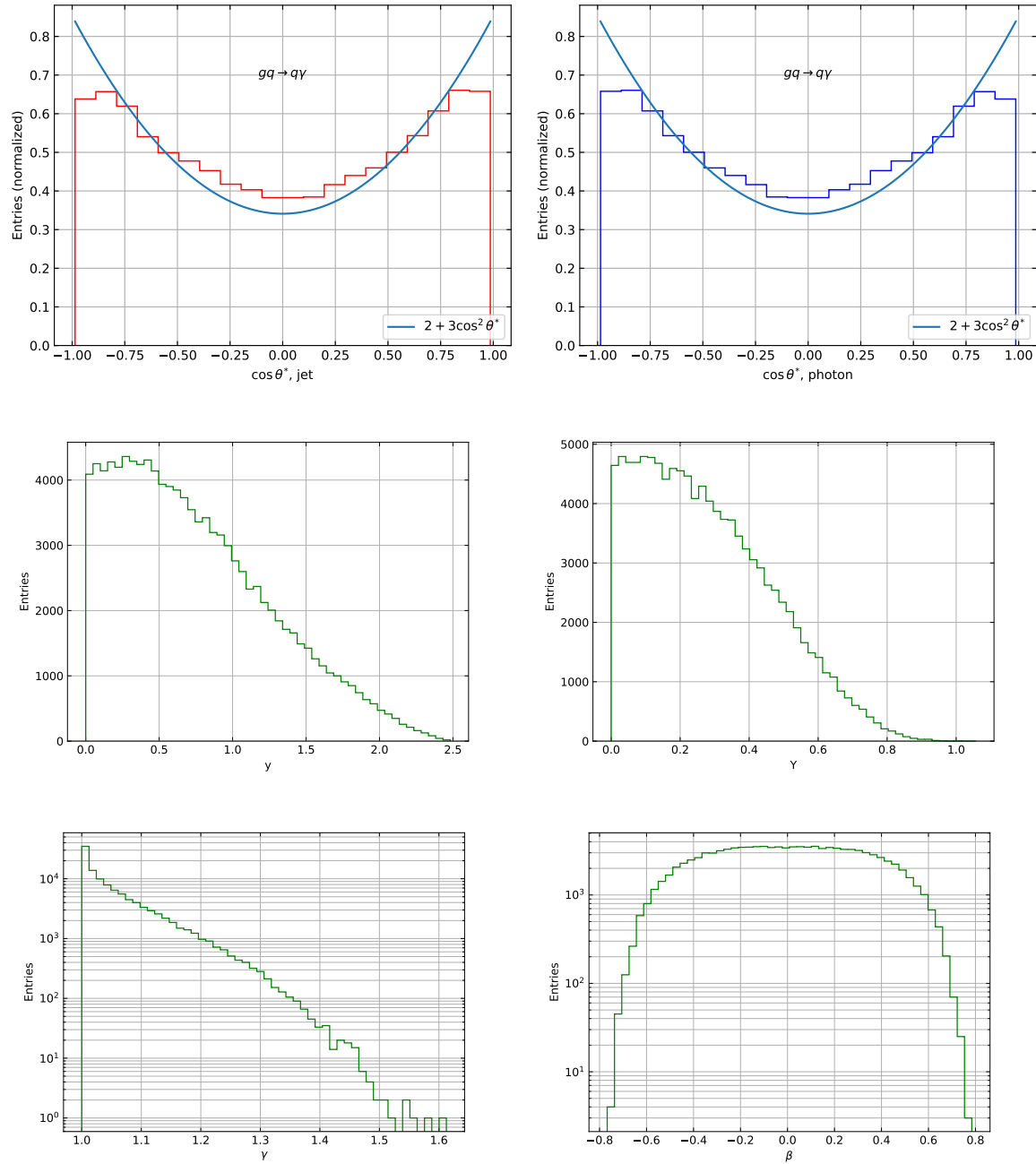


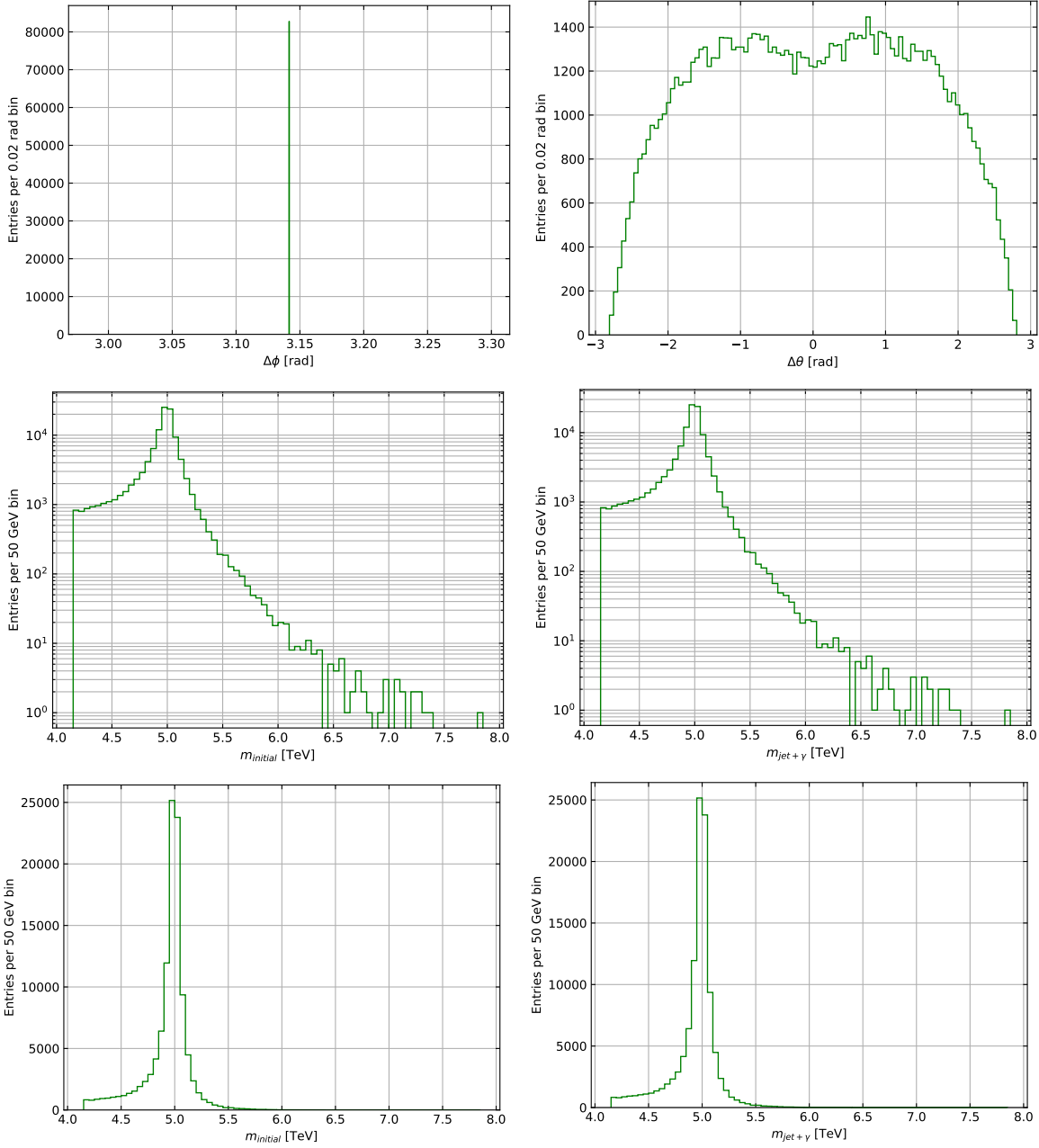
#### 9.4.6 $\sqrt{s} = 13.6$ TeV, $M_s = 5$ TeV



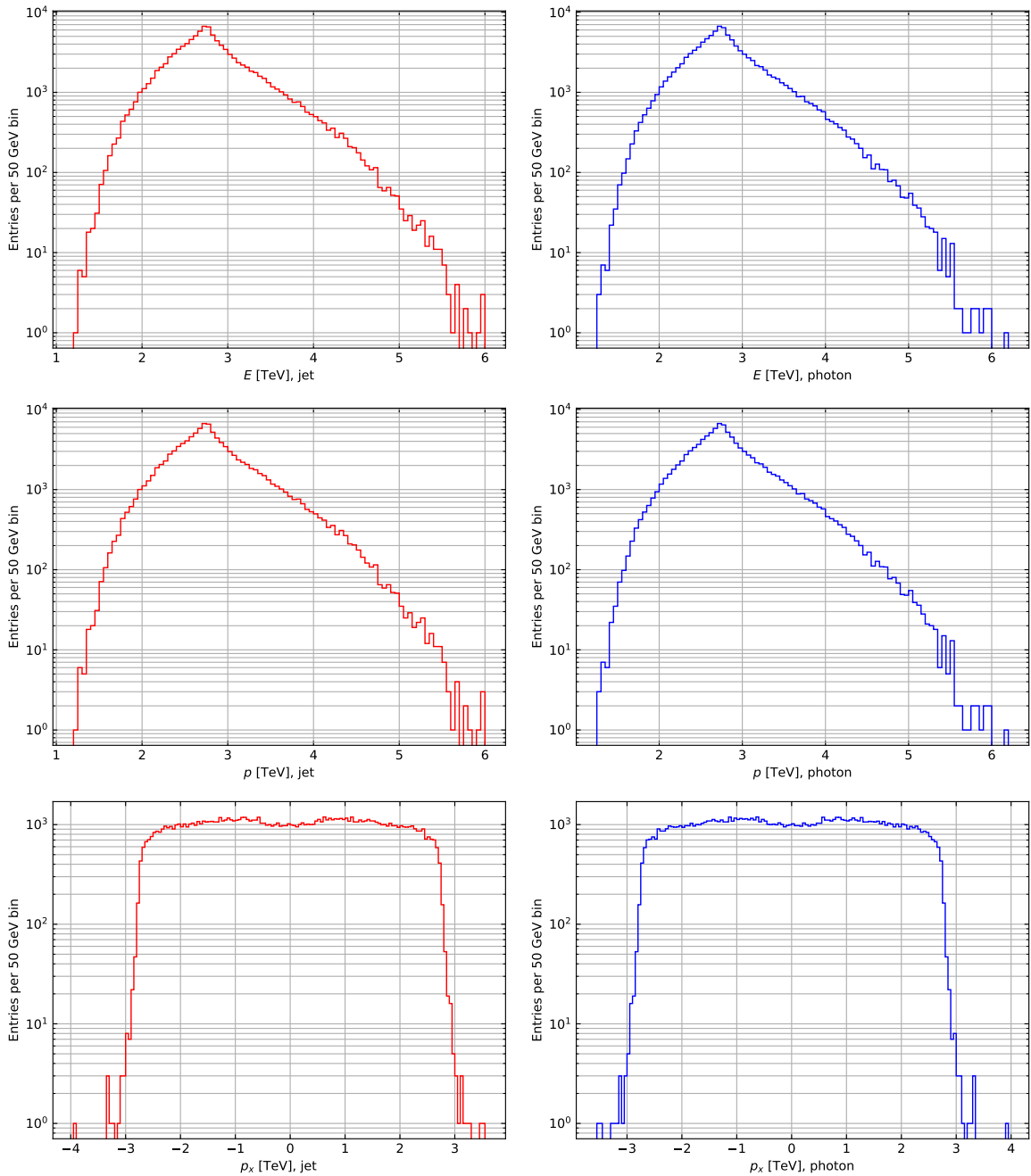


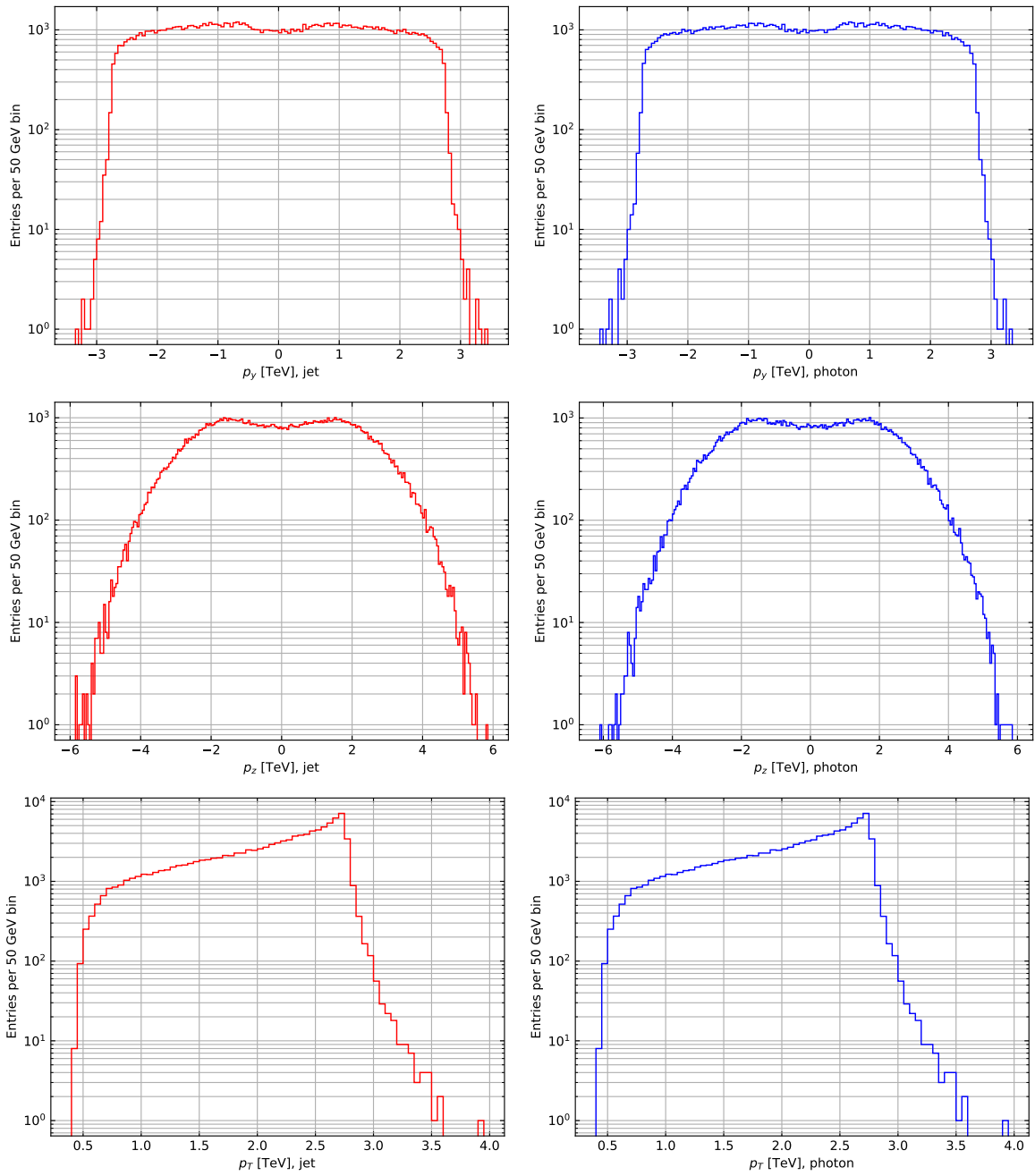


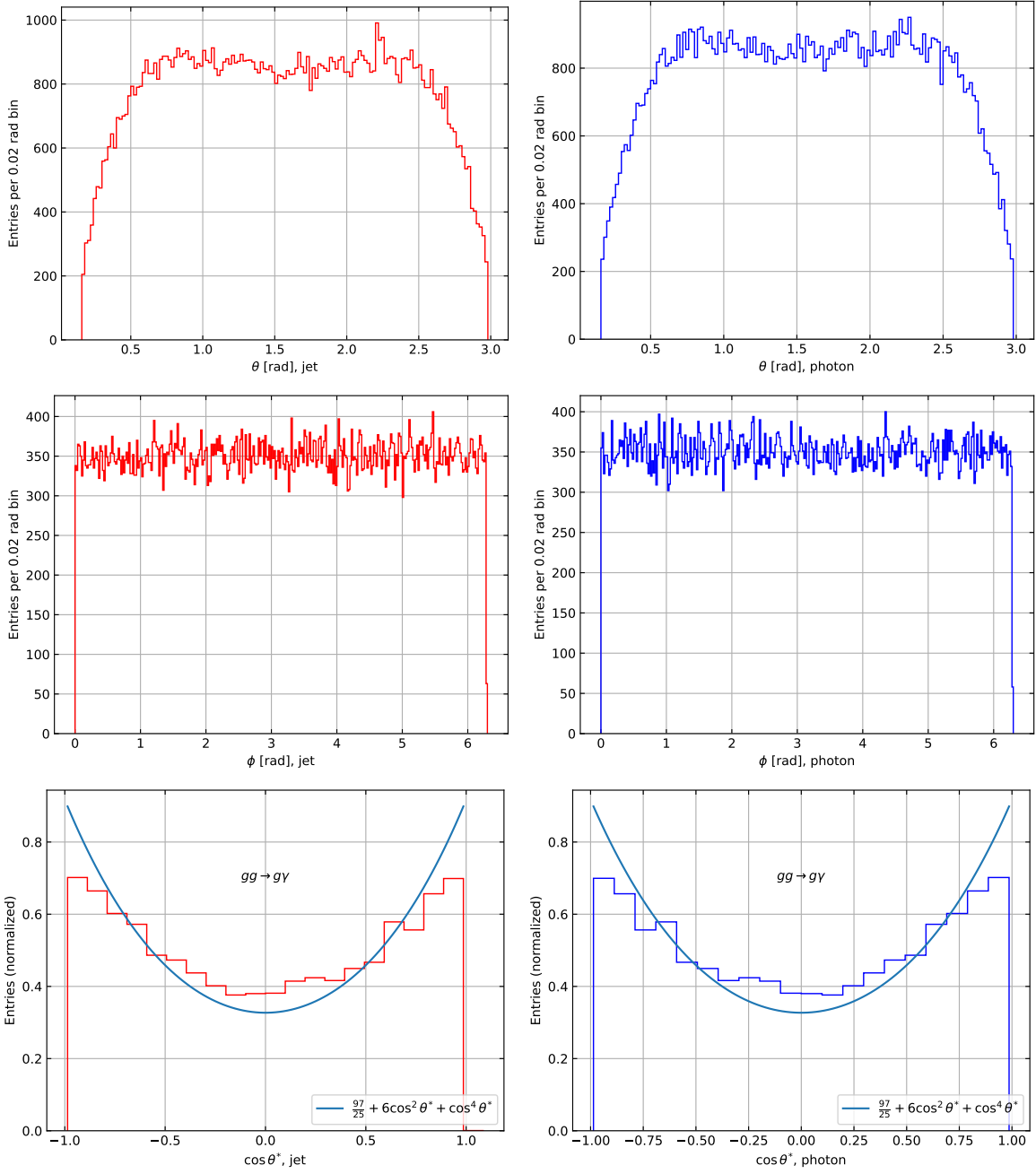


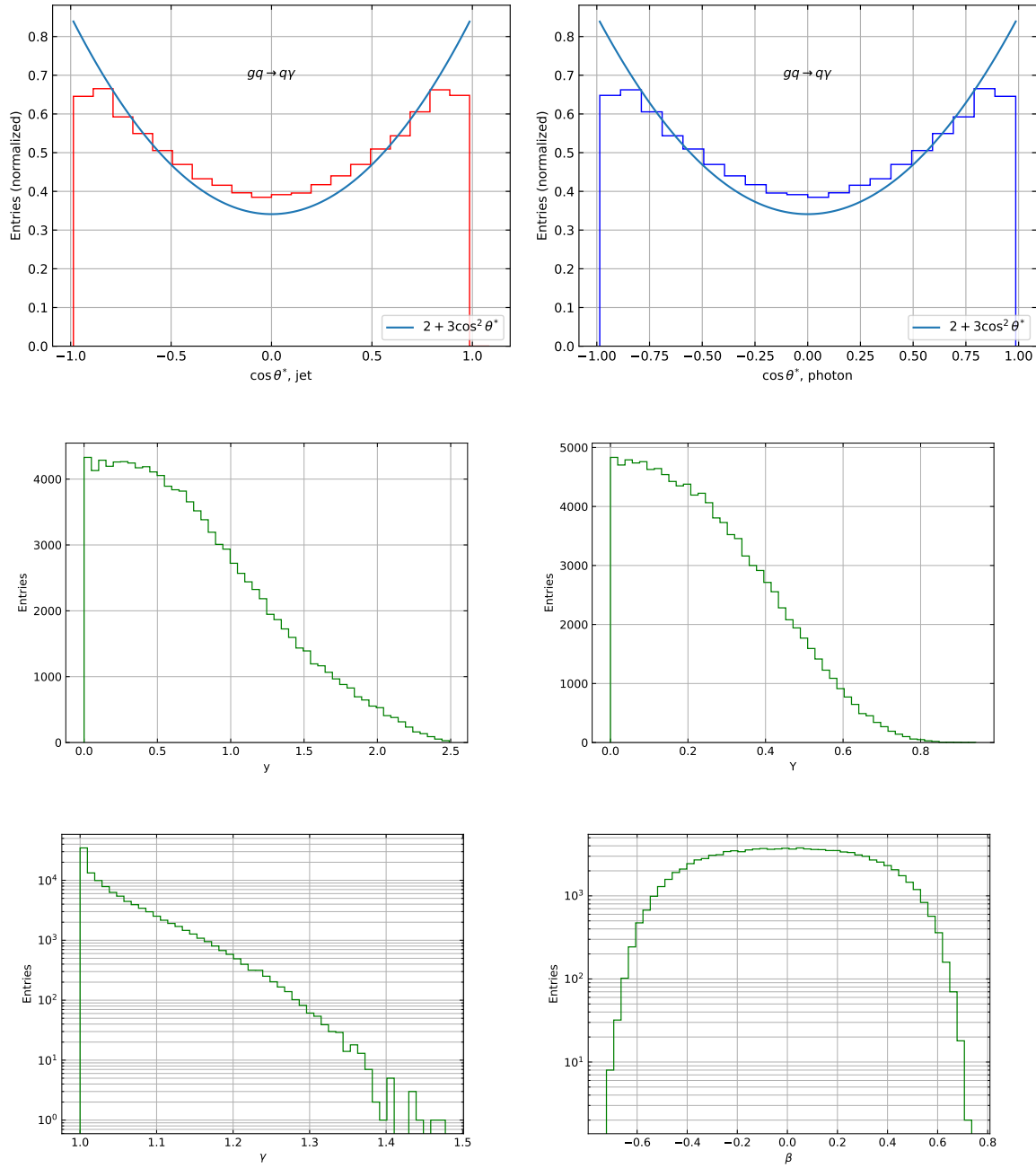


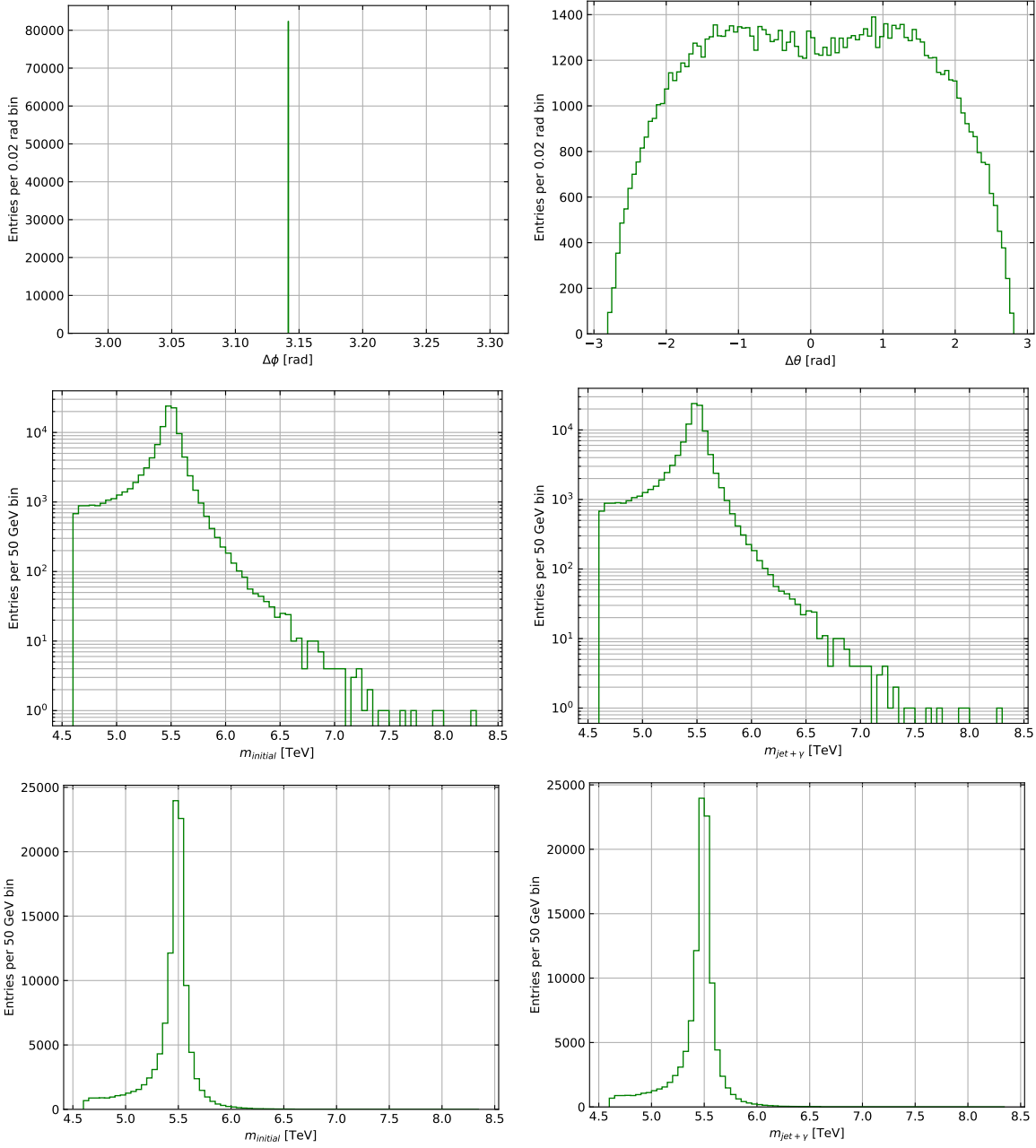
#### 9.4.7 $\sqrt{s} = 13.6$ TeV, $M_s = 5.5$ TeV



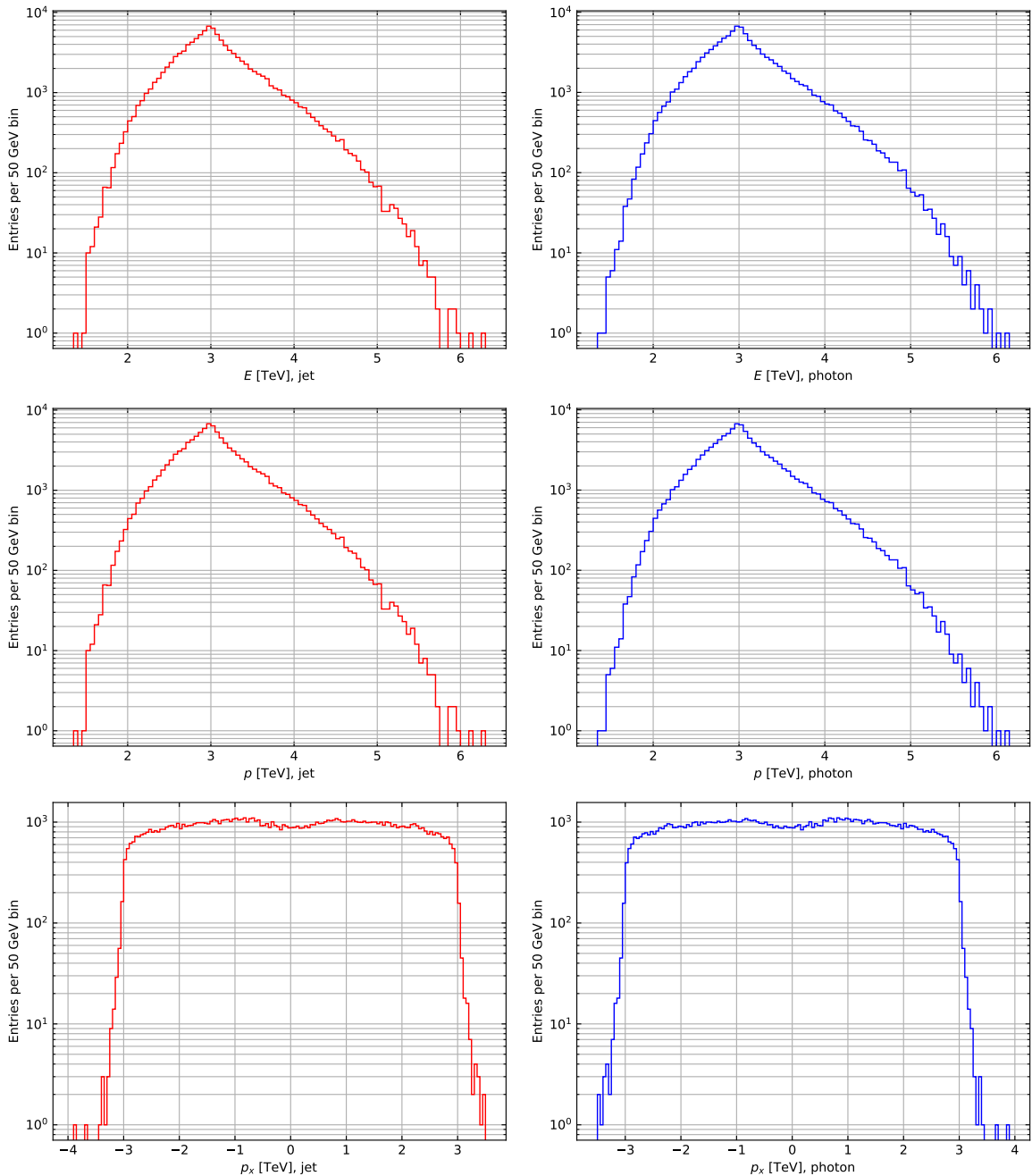


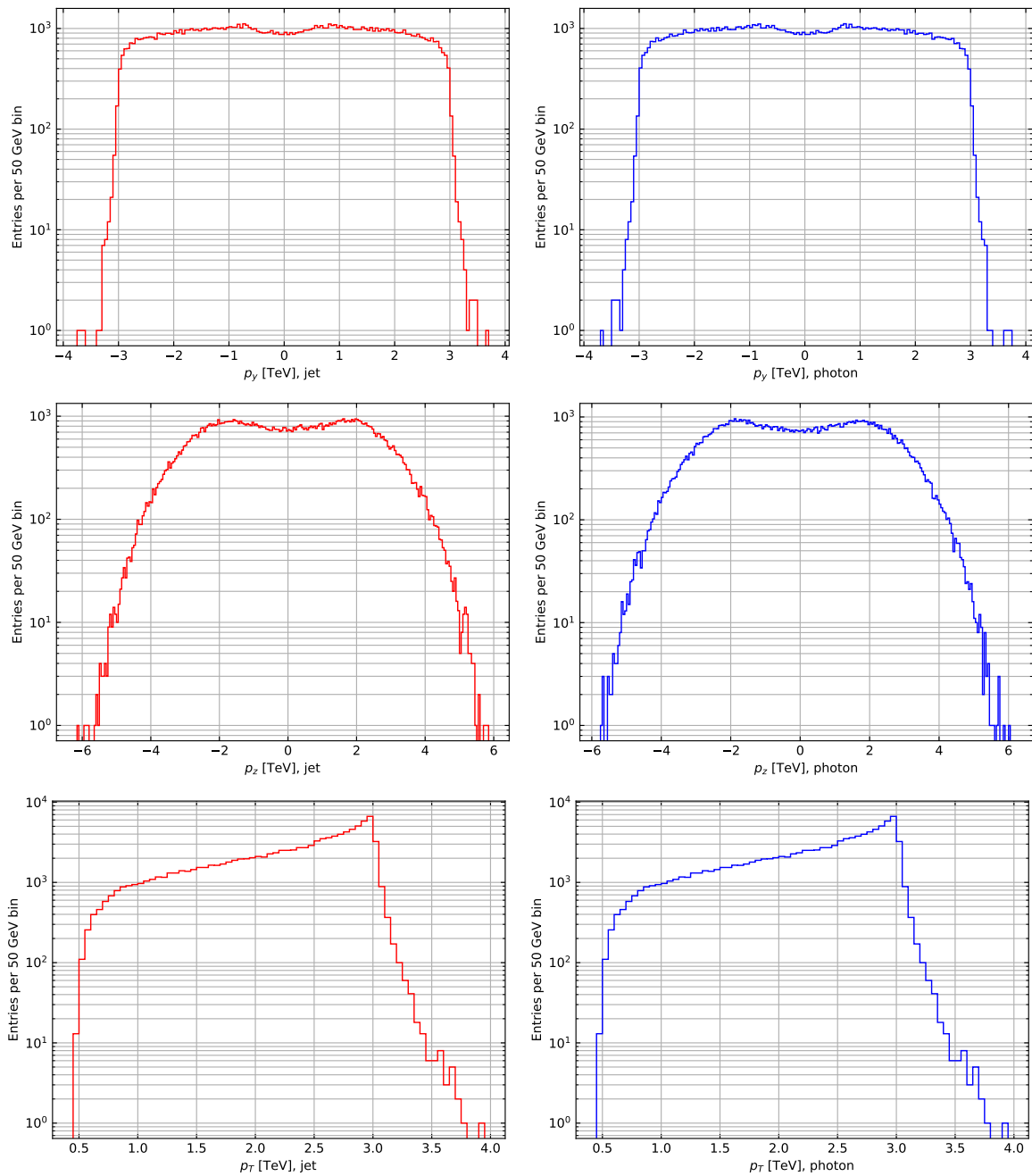


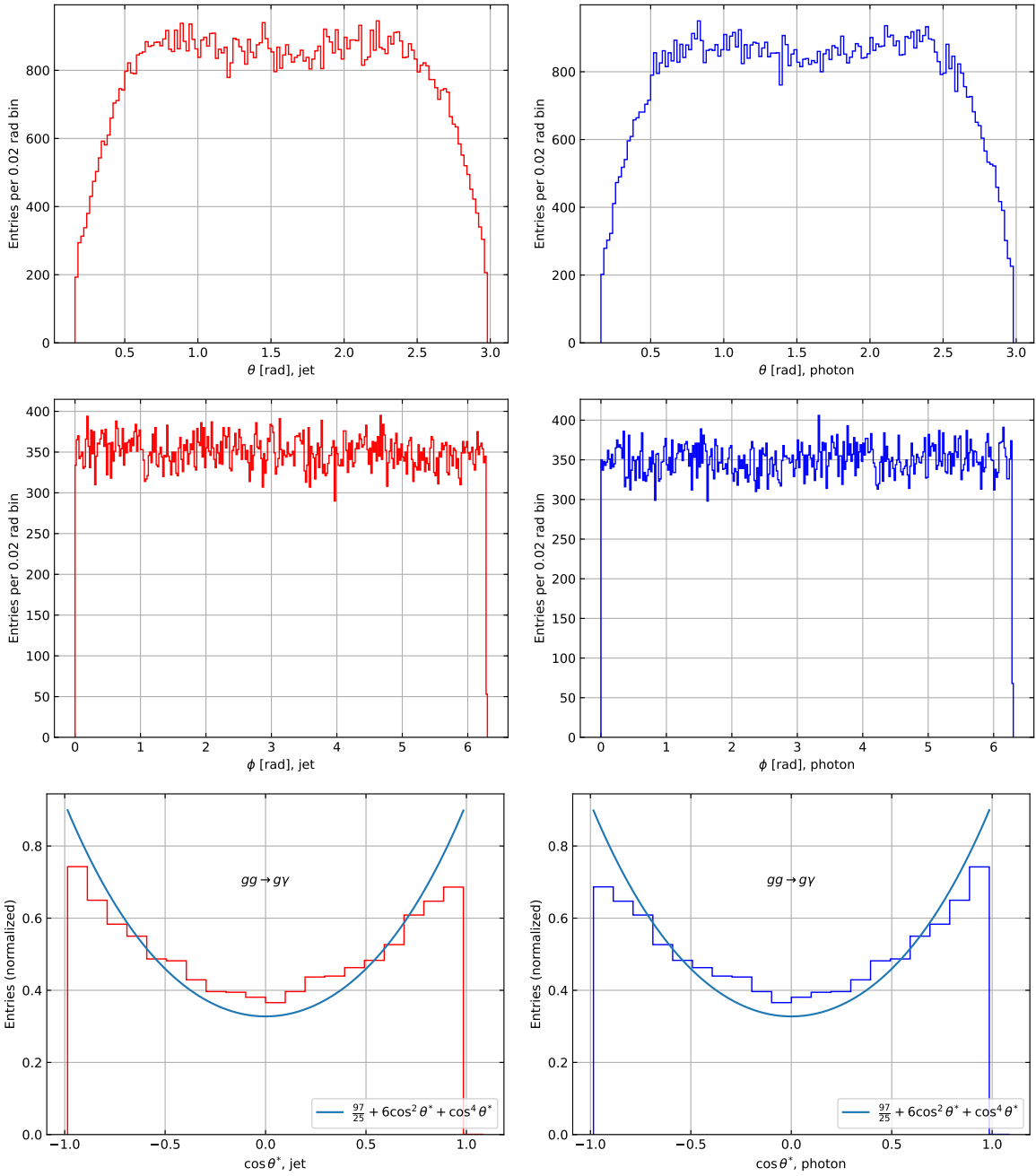


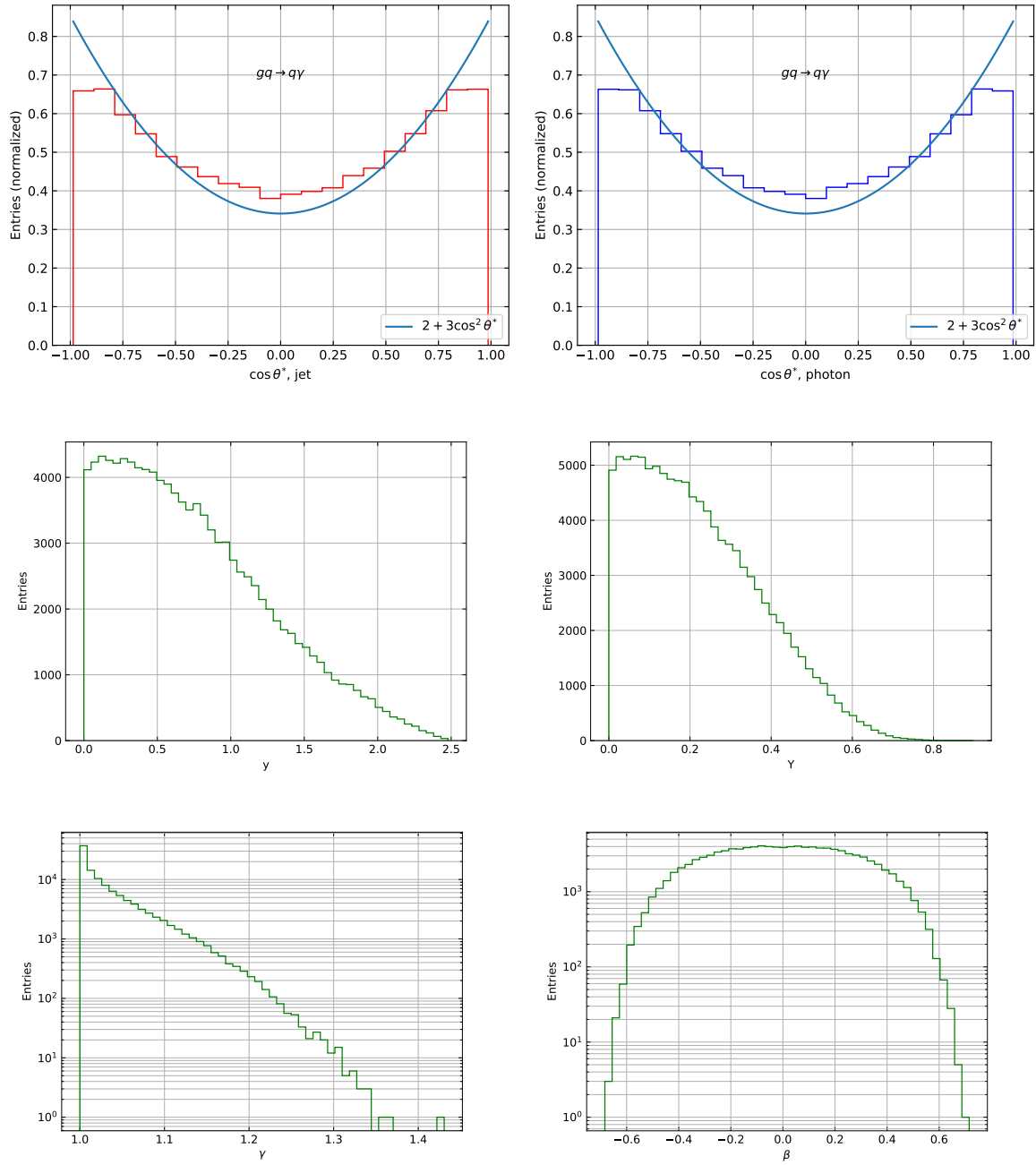


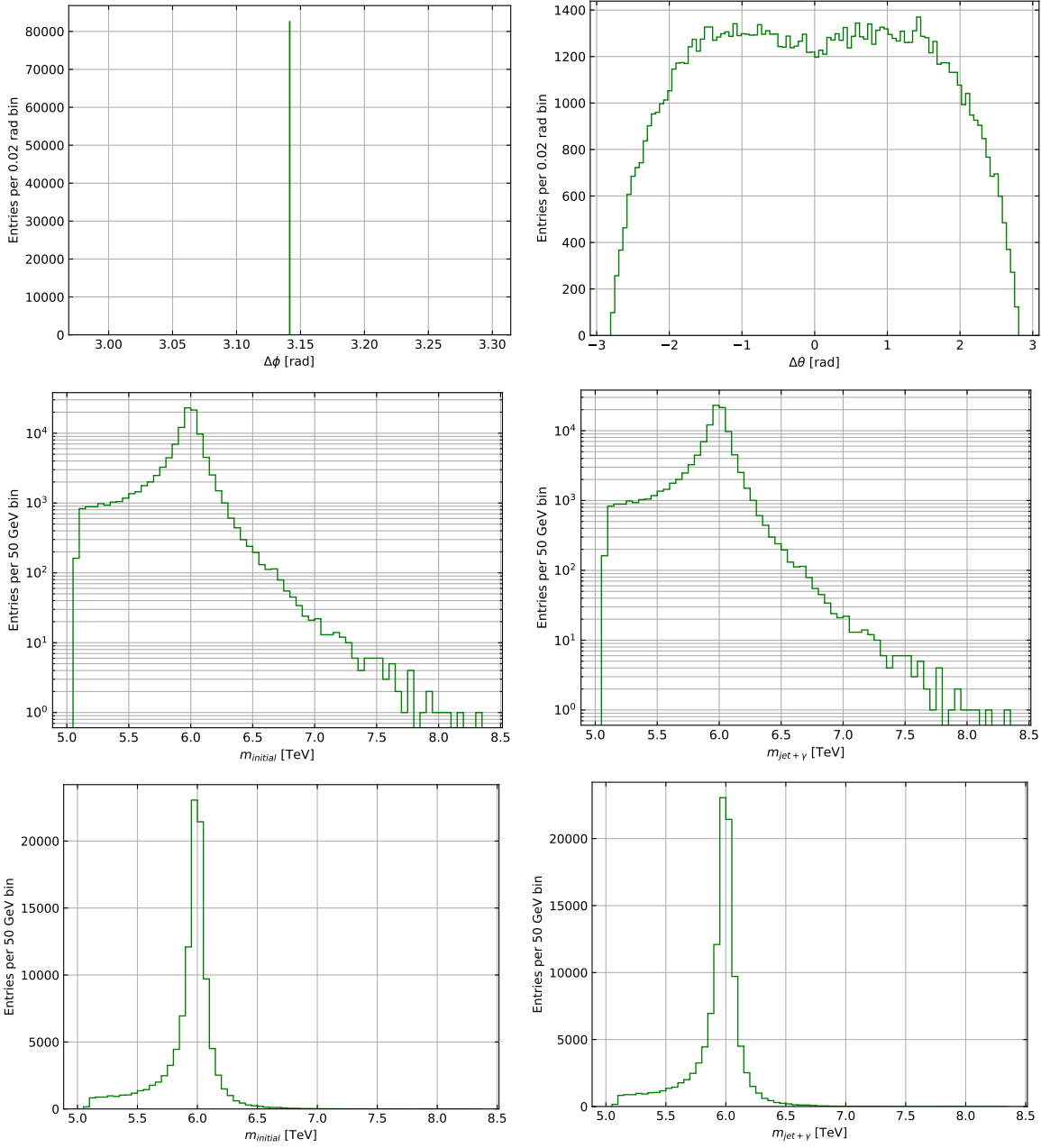
#### 9.4.8 $\sqrt{s} = 13.6$ TeV, $M_s = 6$ TeV



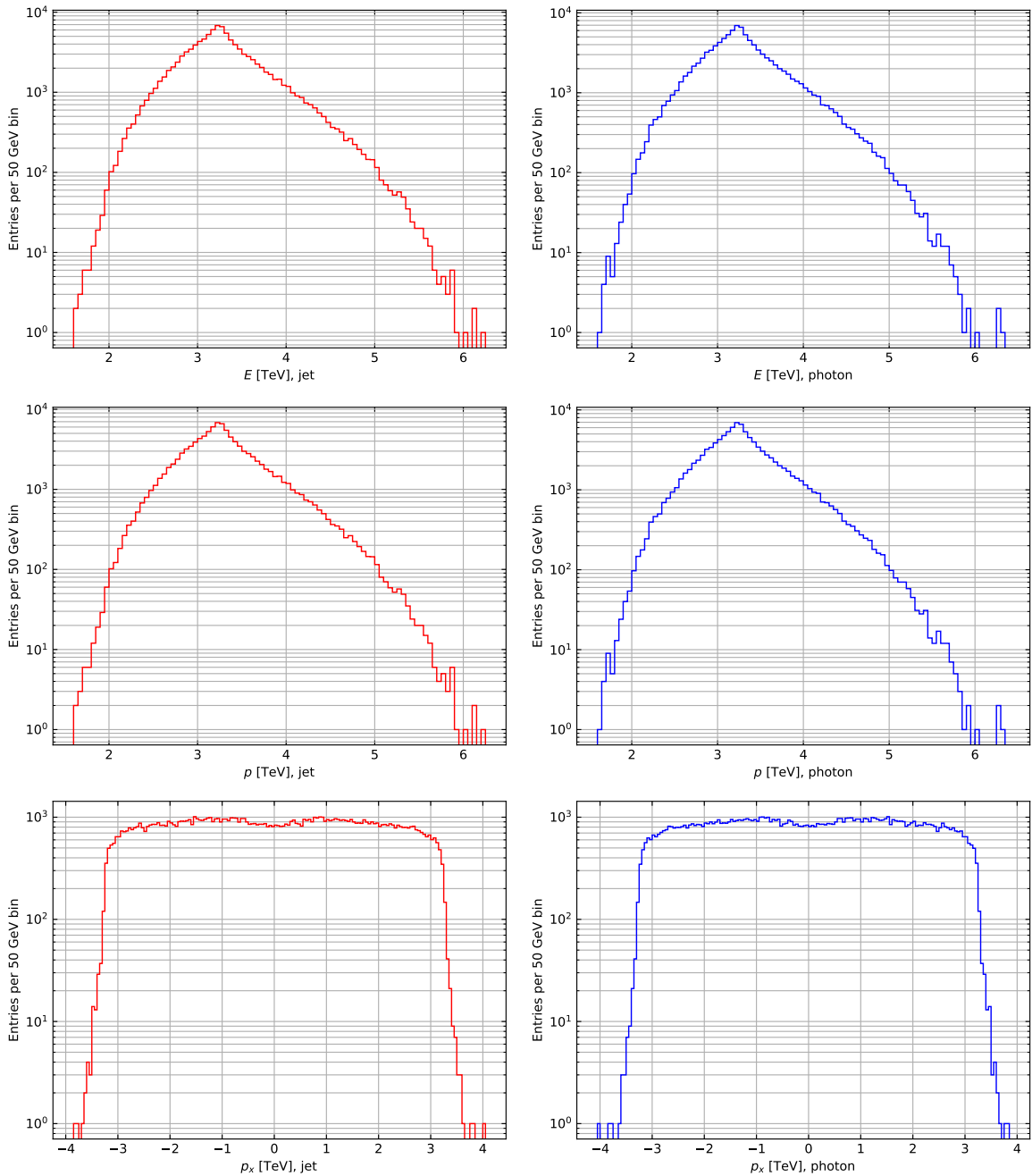


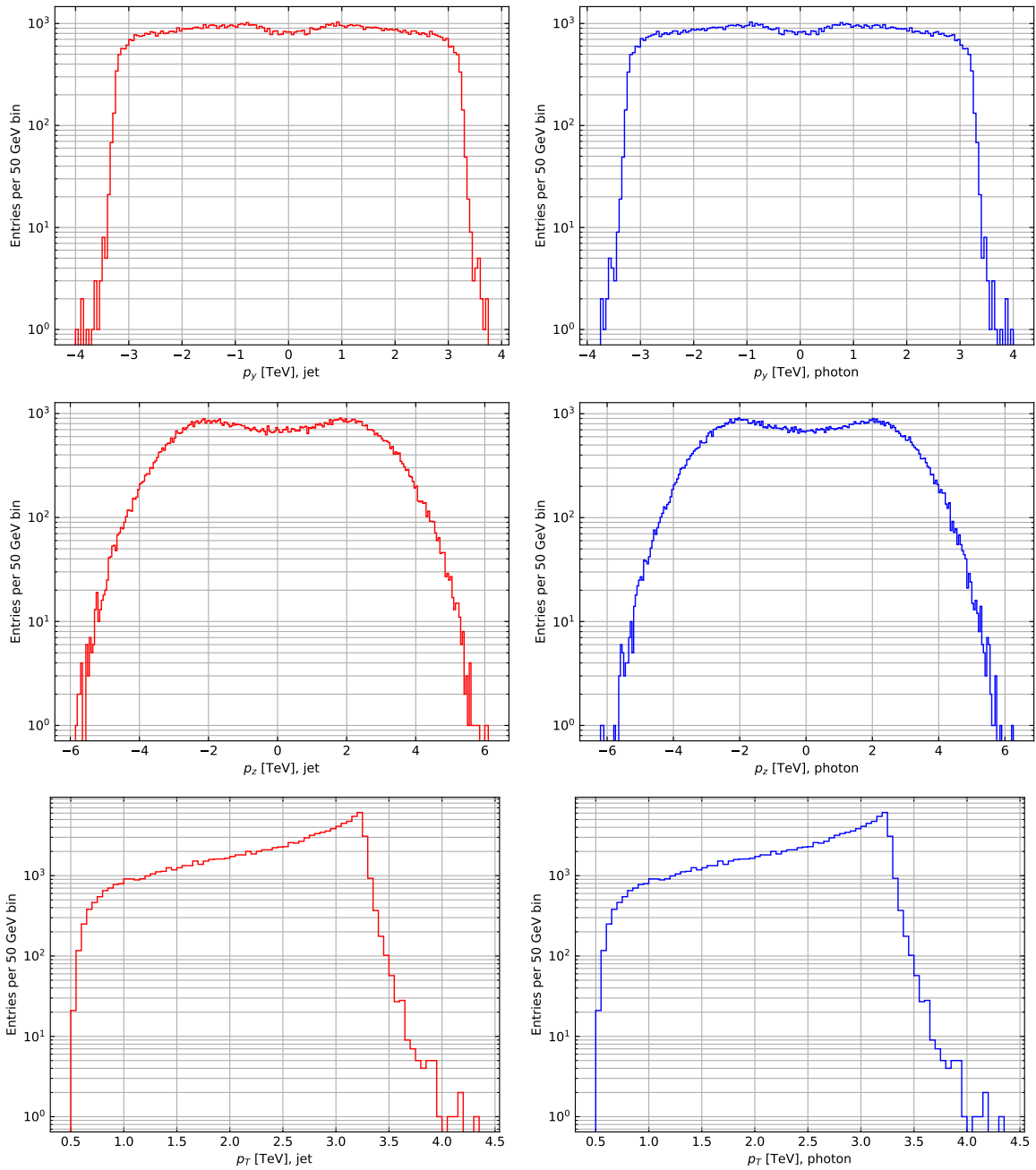


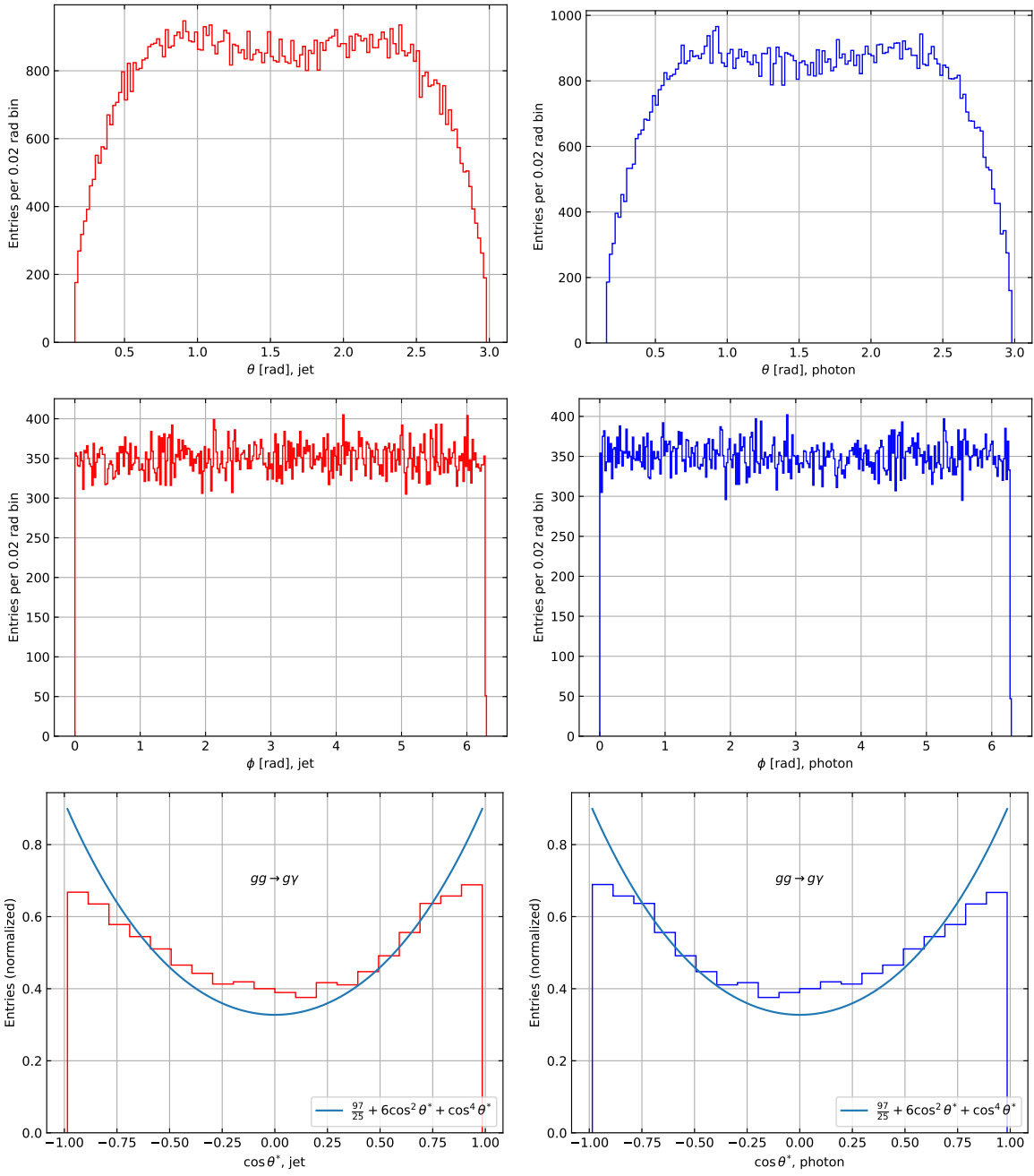


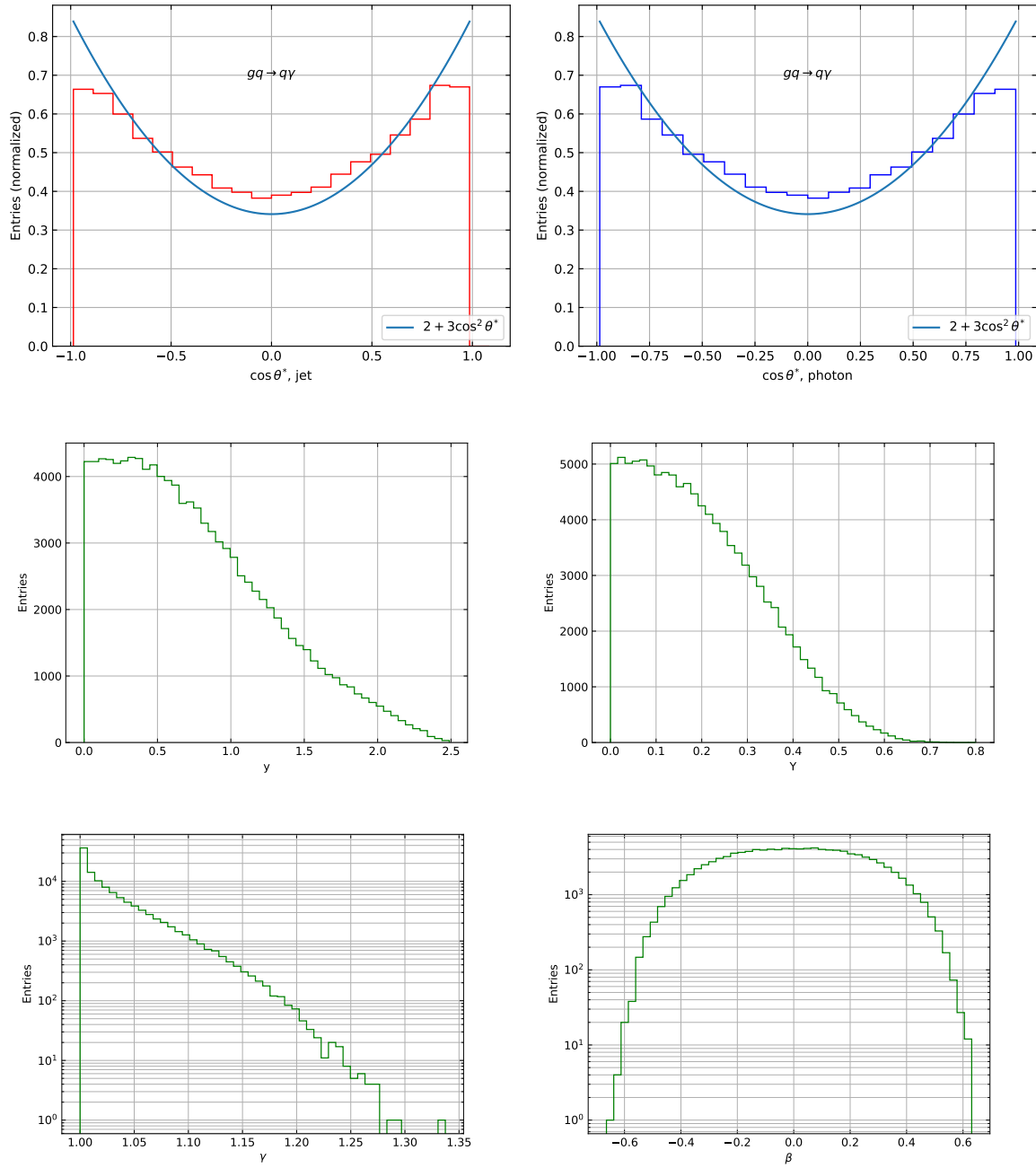


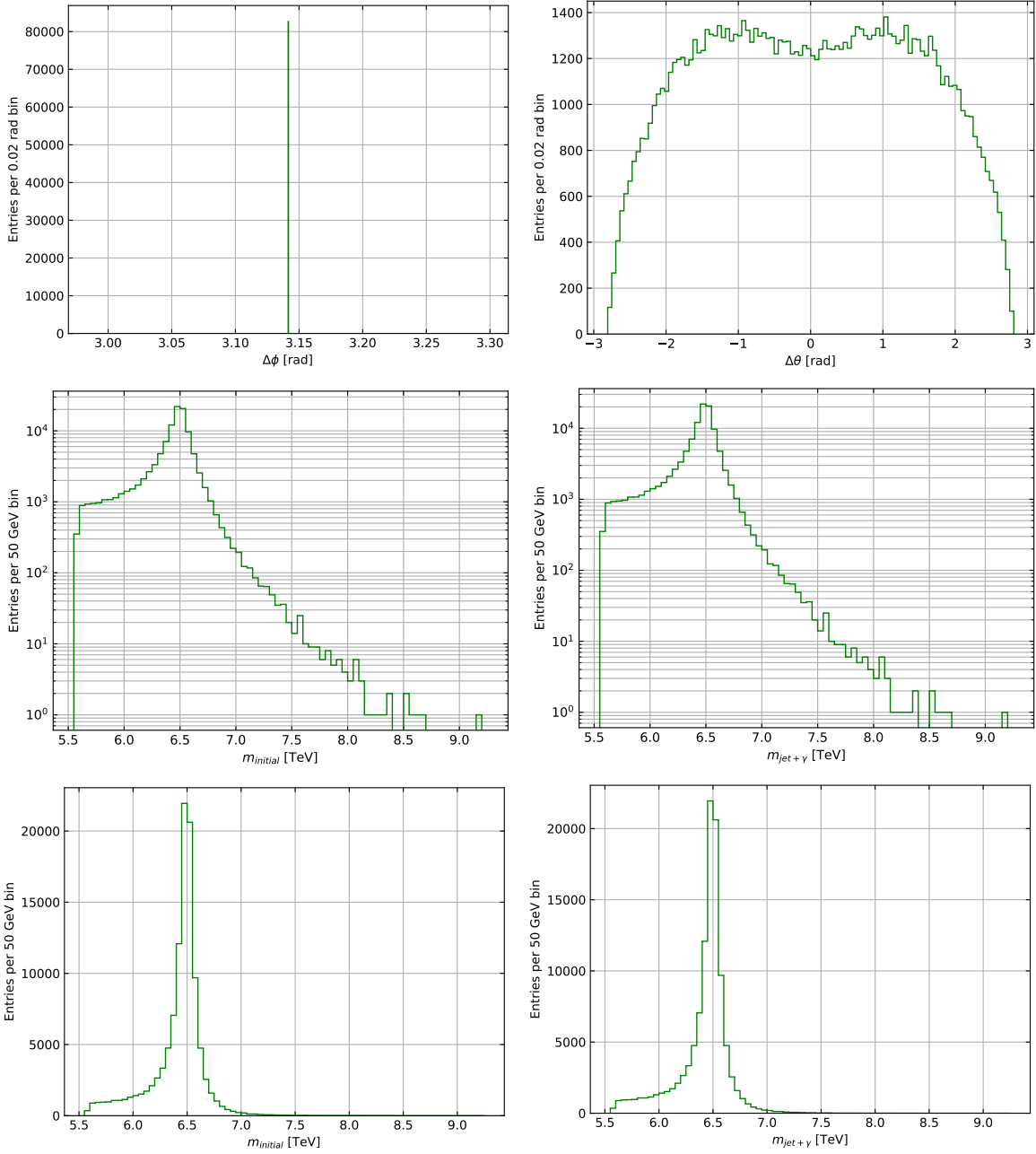
#### 9.4.9 $\sqrt{s} = 13.6$ TeV, $M_s = 6.5$ TeV



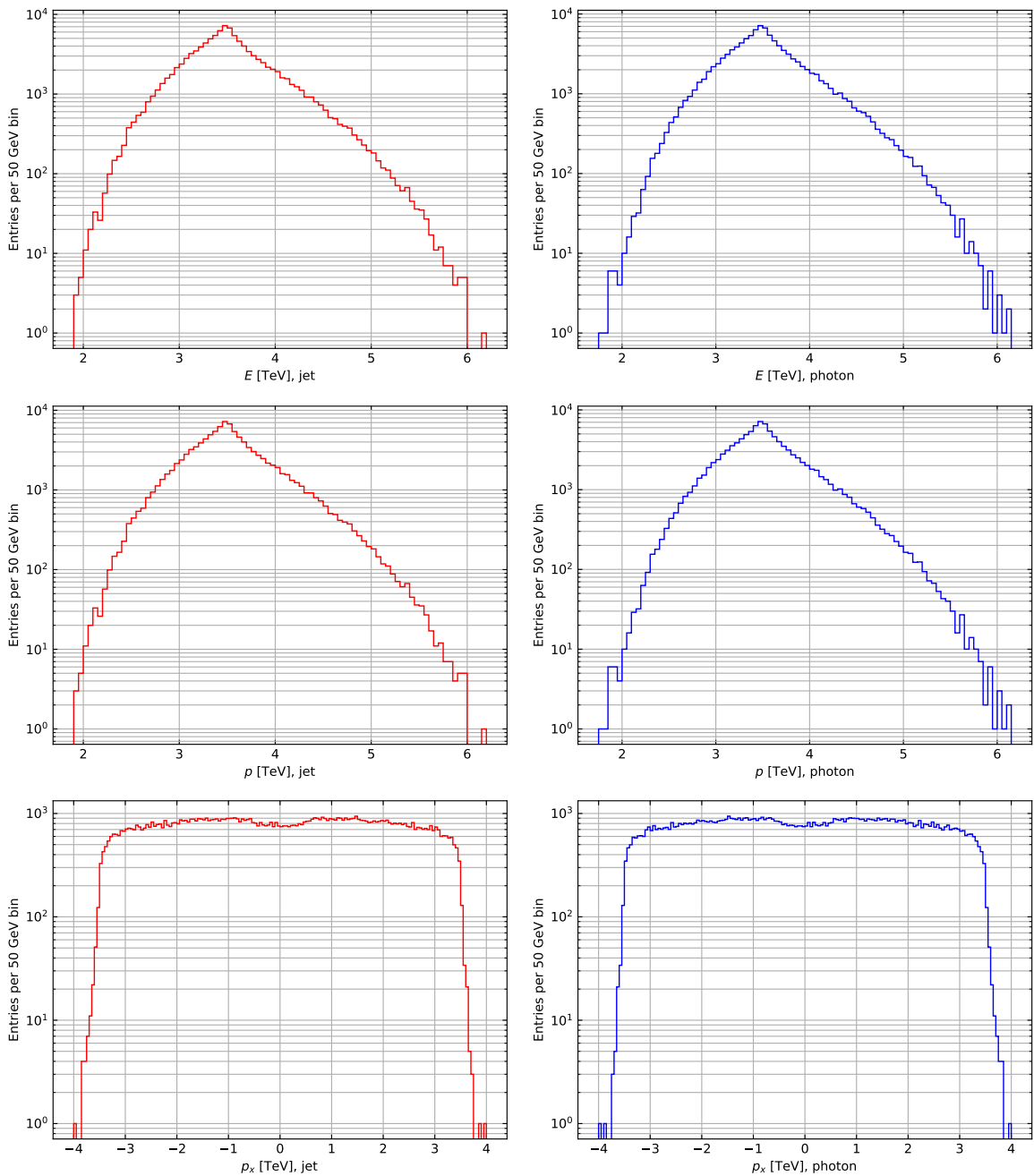


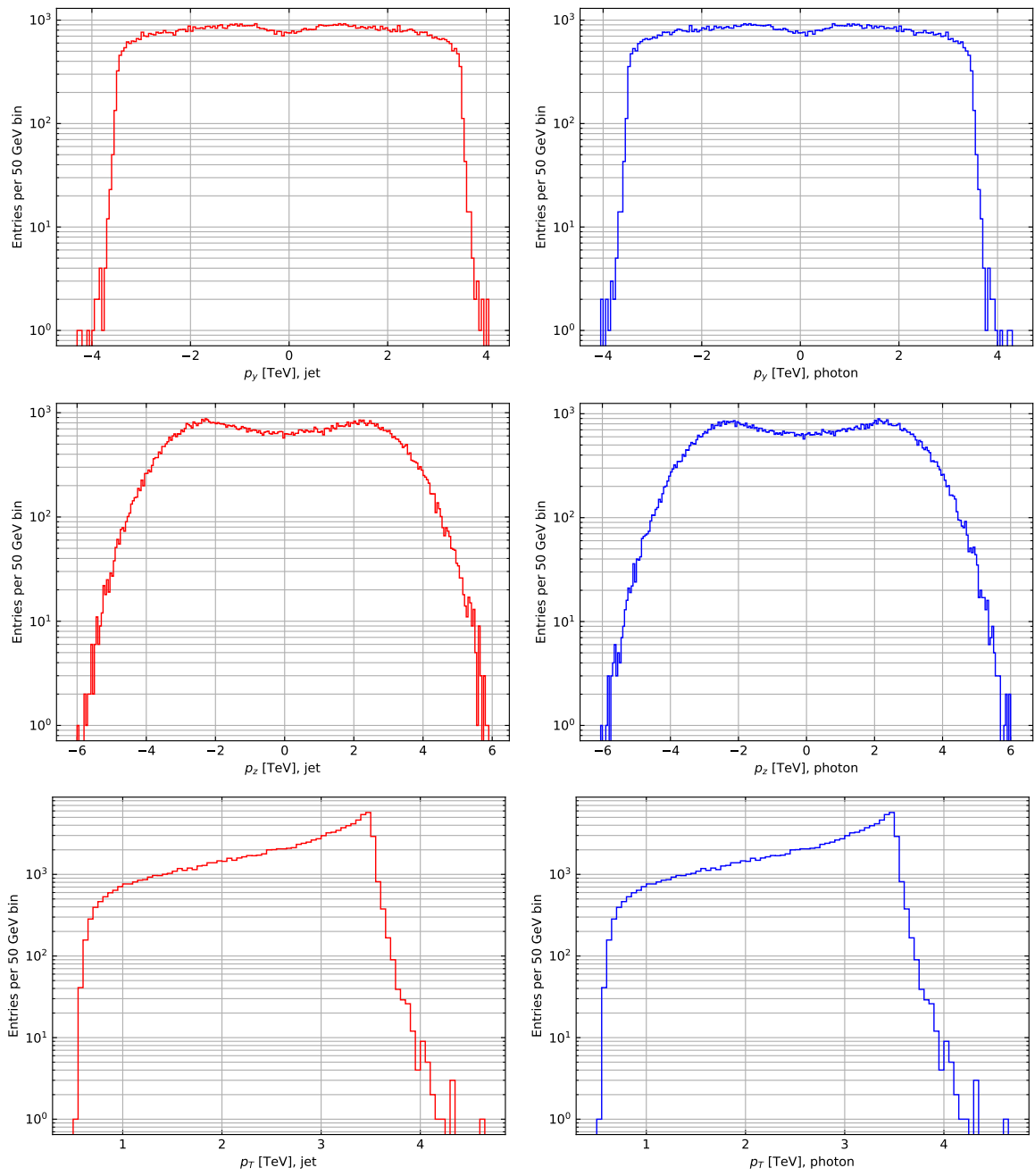


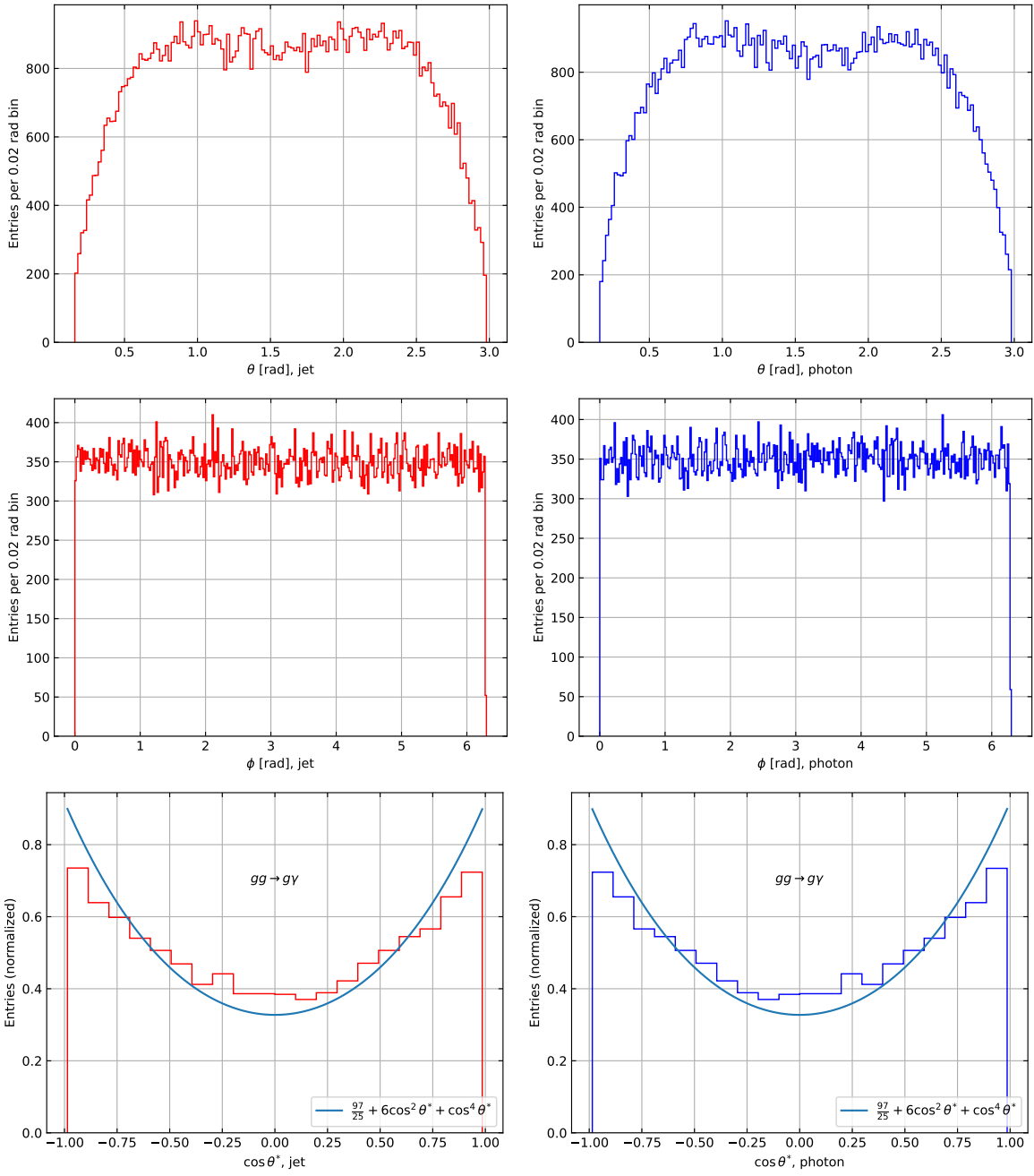


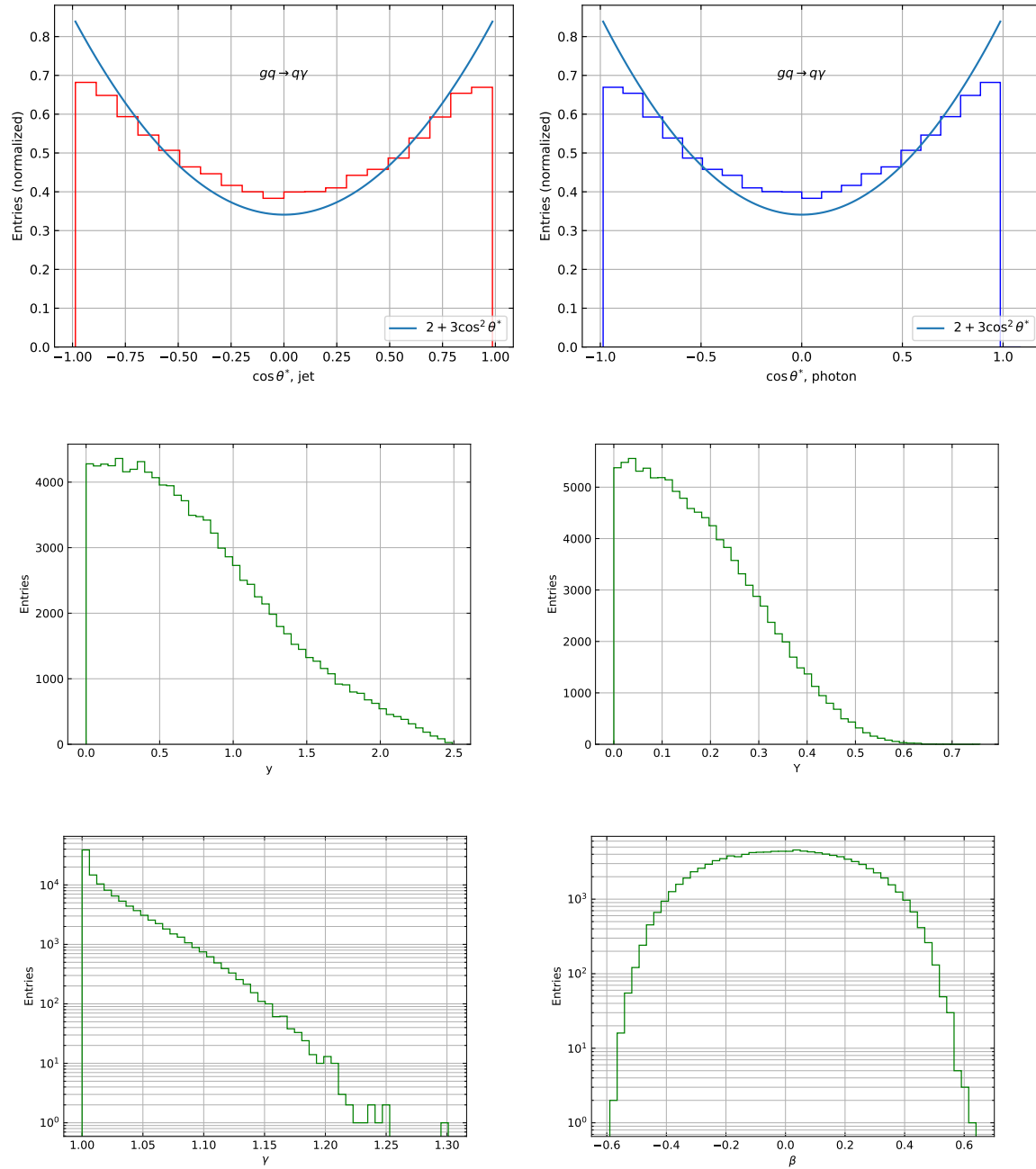


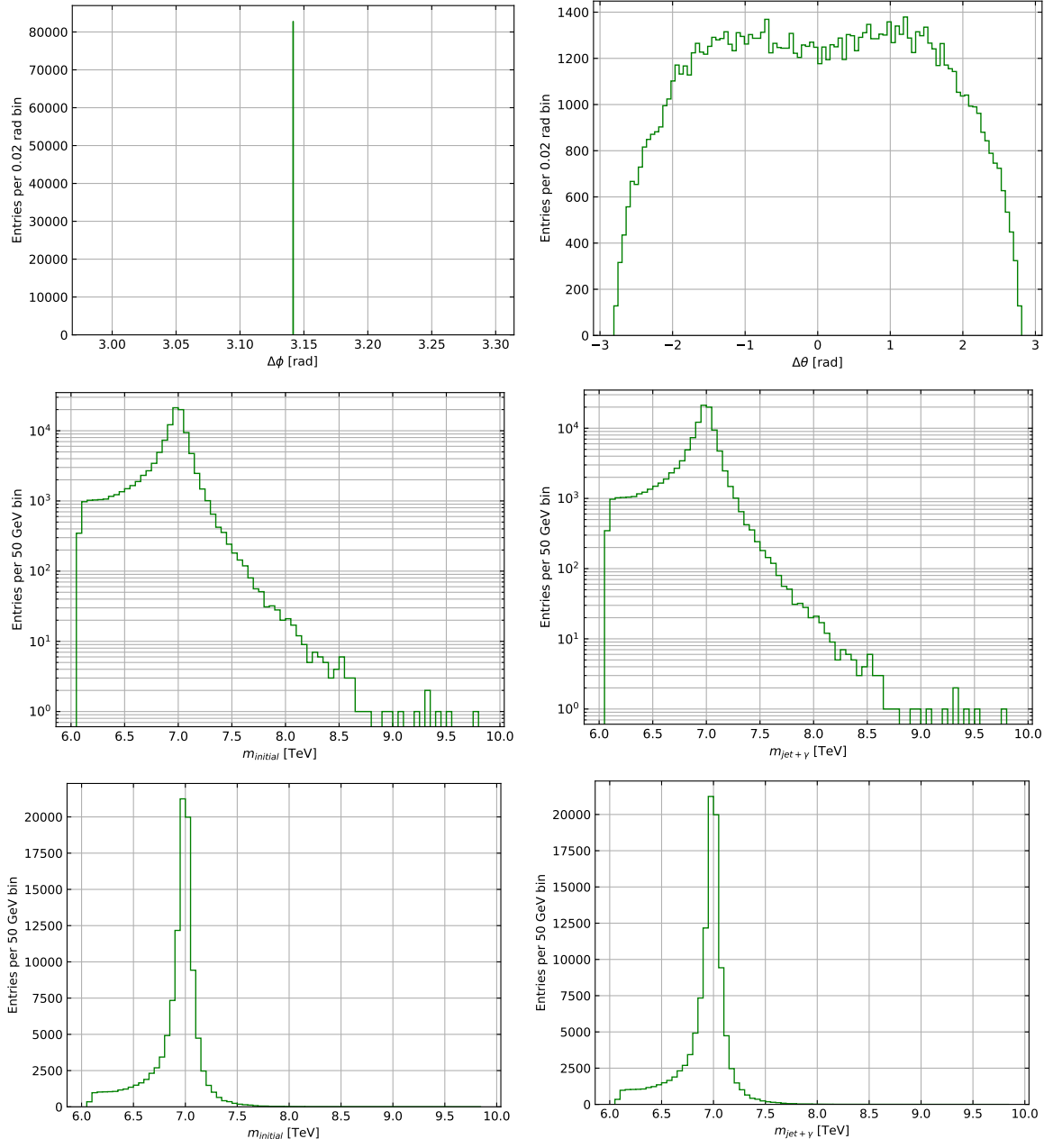
#### 9.4.10 $\sqrt{s} = 13.6$ TeV, $M_s = 7$ TeV





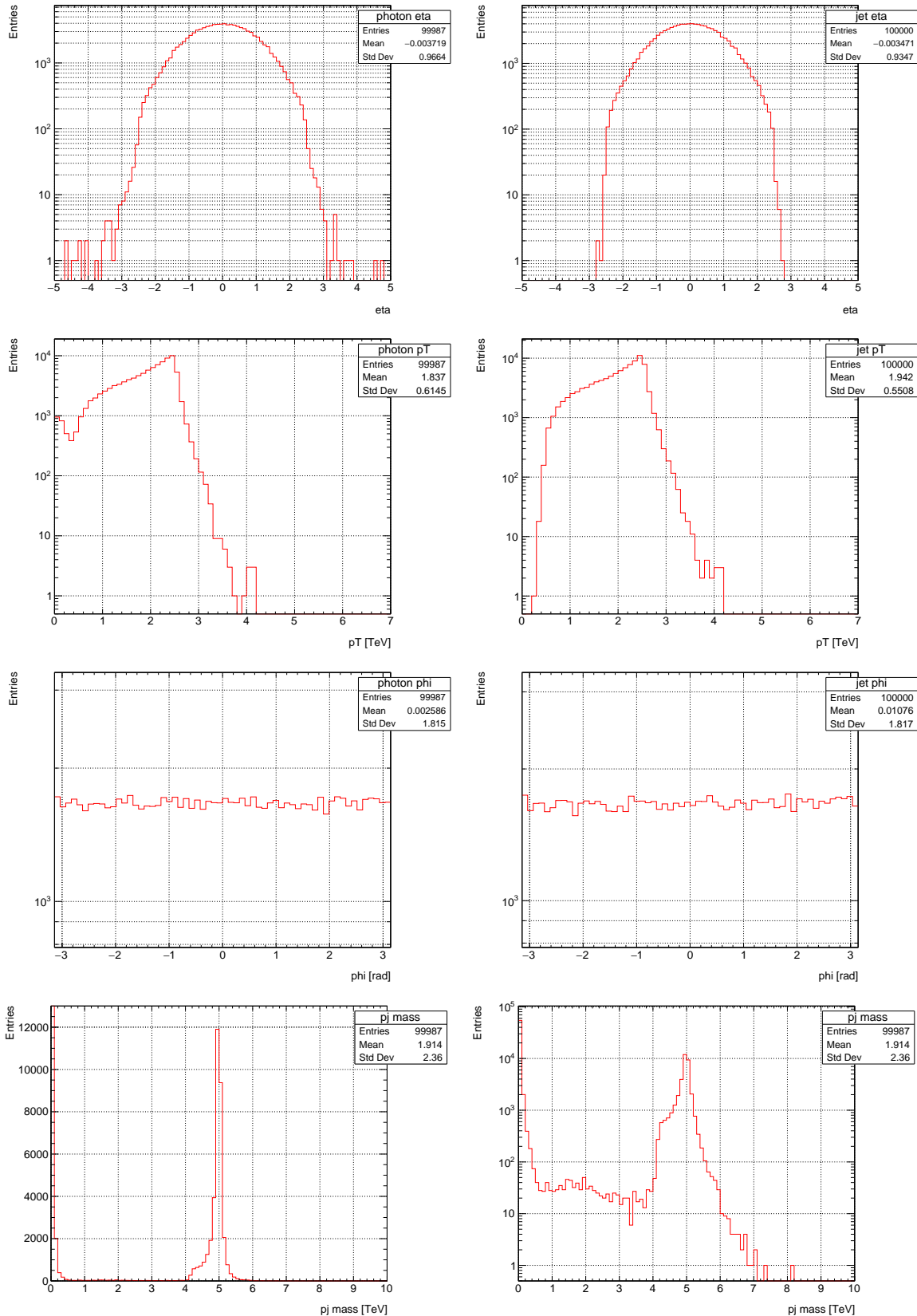




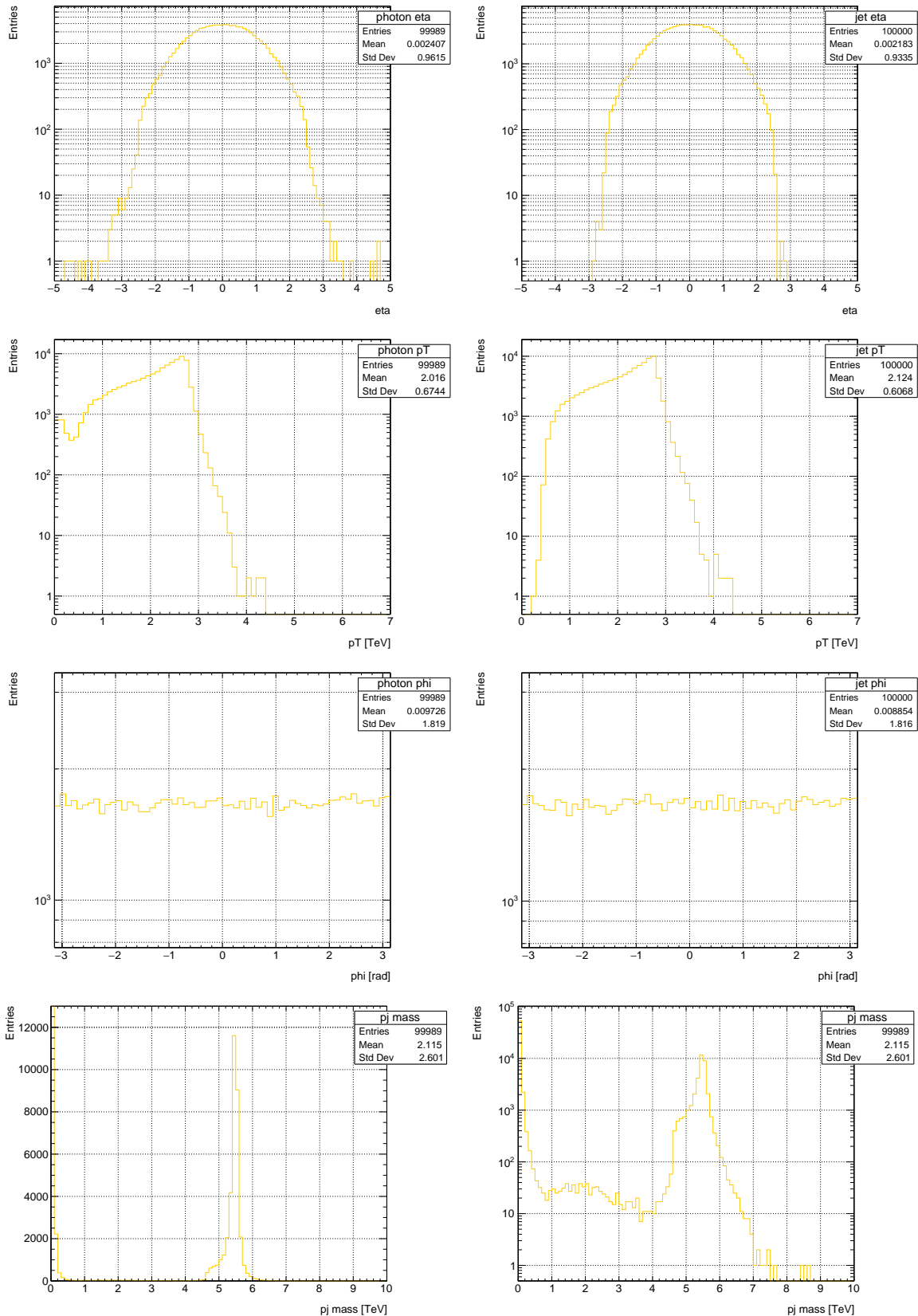


## 9.5 Pythia Kinematic Data

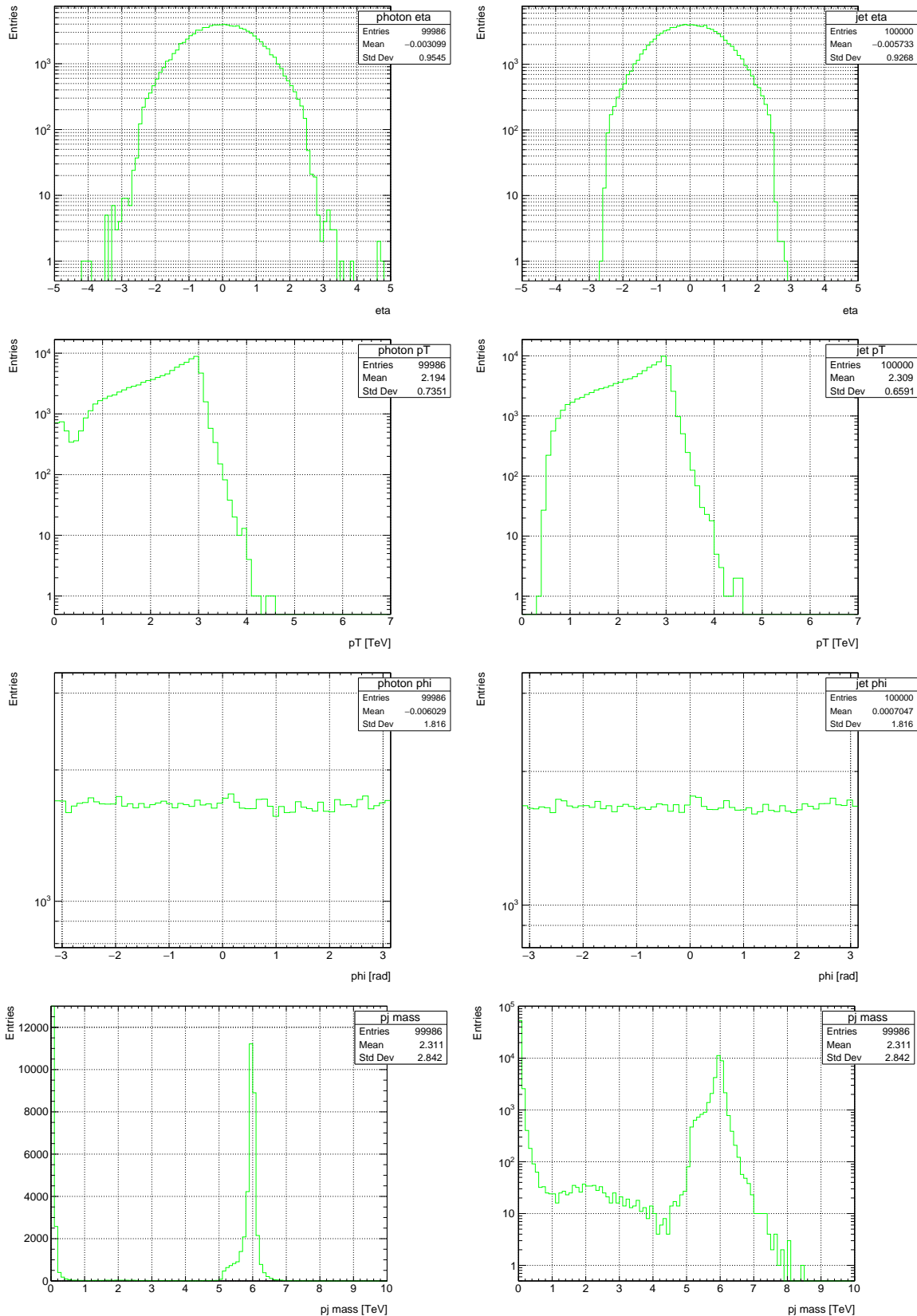
### 9.5.1 $M_s = 5 \text{ TeV}$ , $\sqrt{s} = 13 \text{ TeV}$



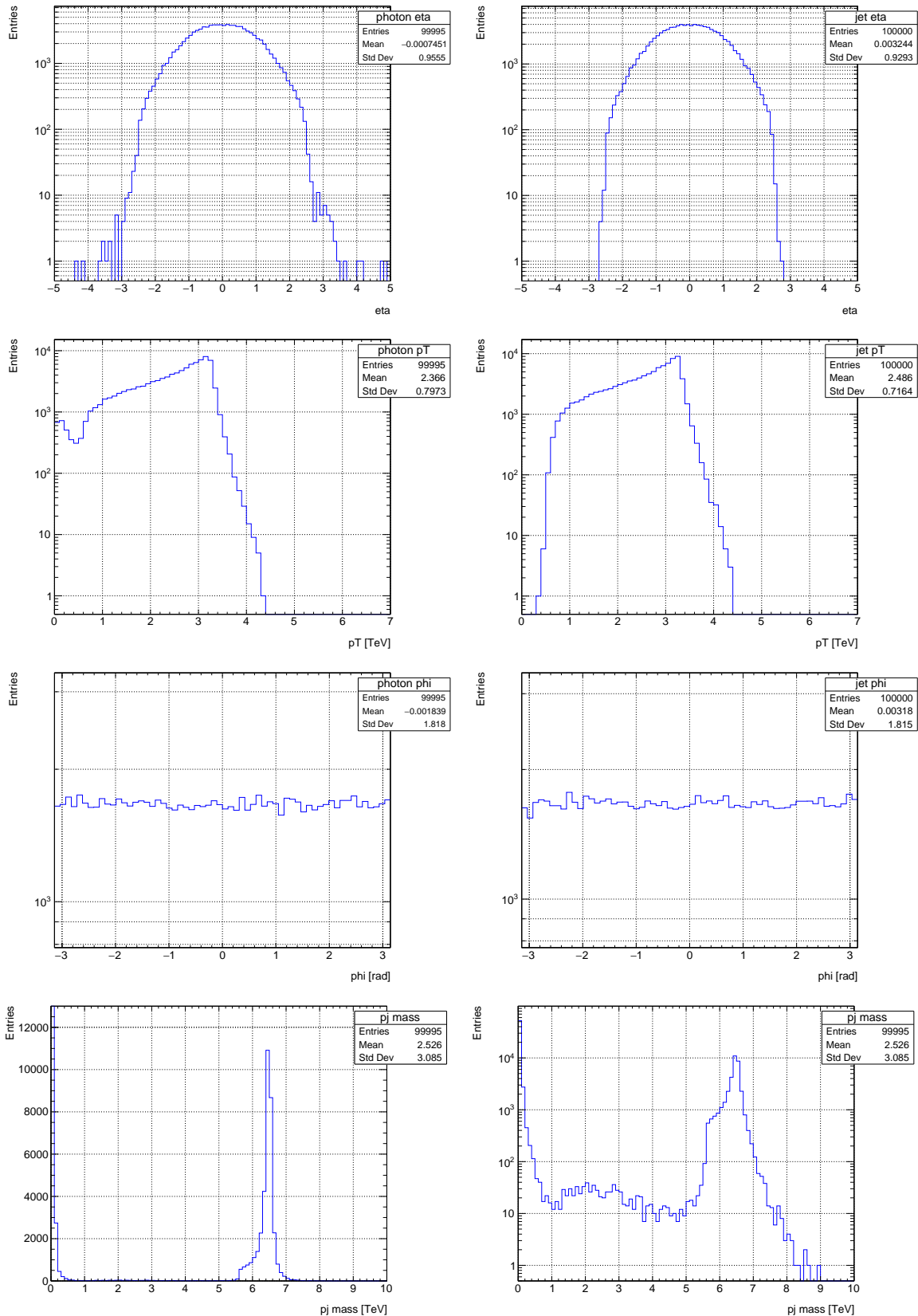
### 9.5.2 $M_s = 5.5$ TeV, $\sqrt{s} = 13$ TeV



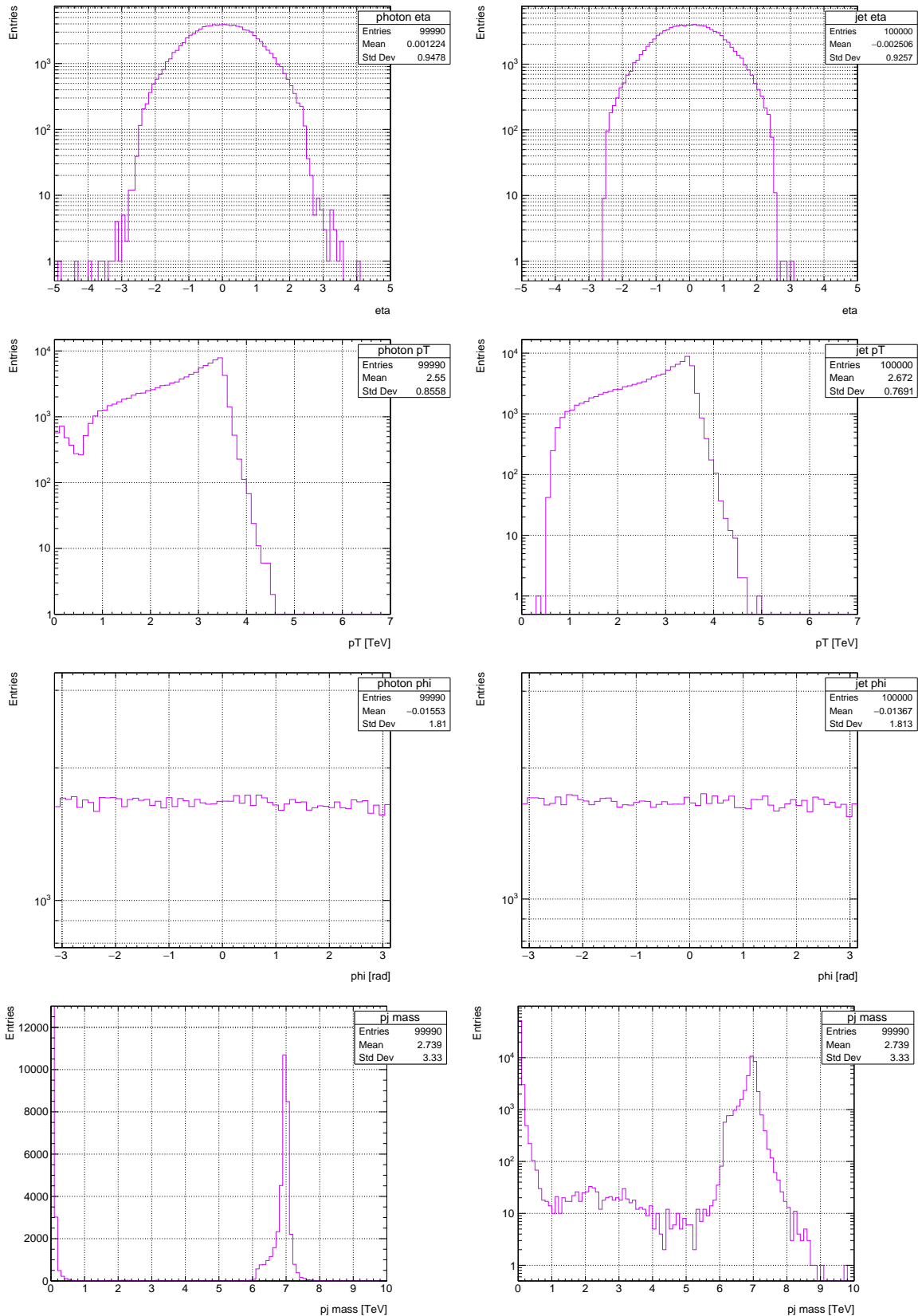
### 9.5.3 $M_s = 6$ TeV, $\sqrt{s} = 13$ TeV



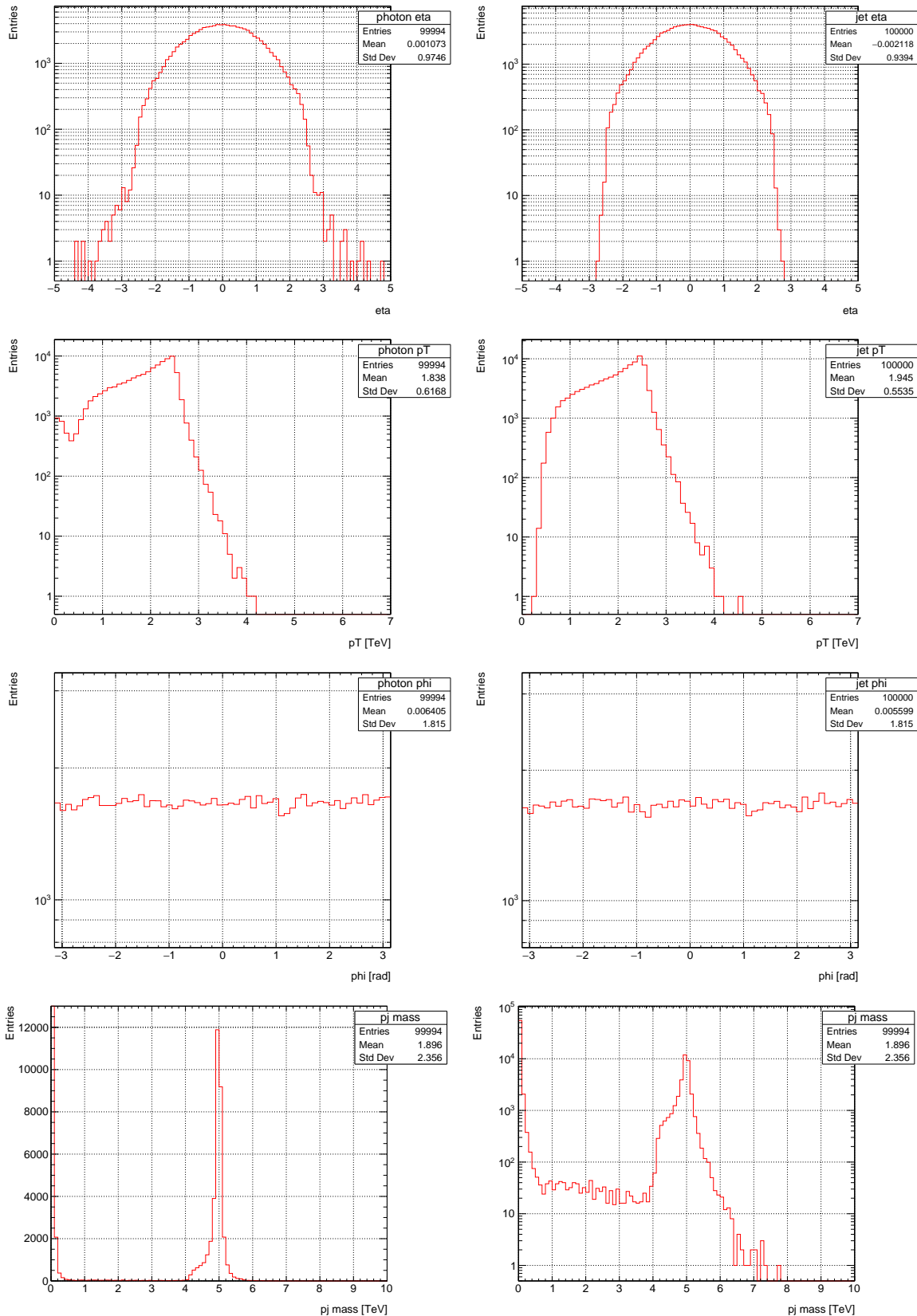
#### 9.5.4 $M_s = 6.5$ TeV, $\sqrt{s} = 13$ TeV



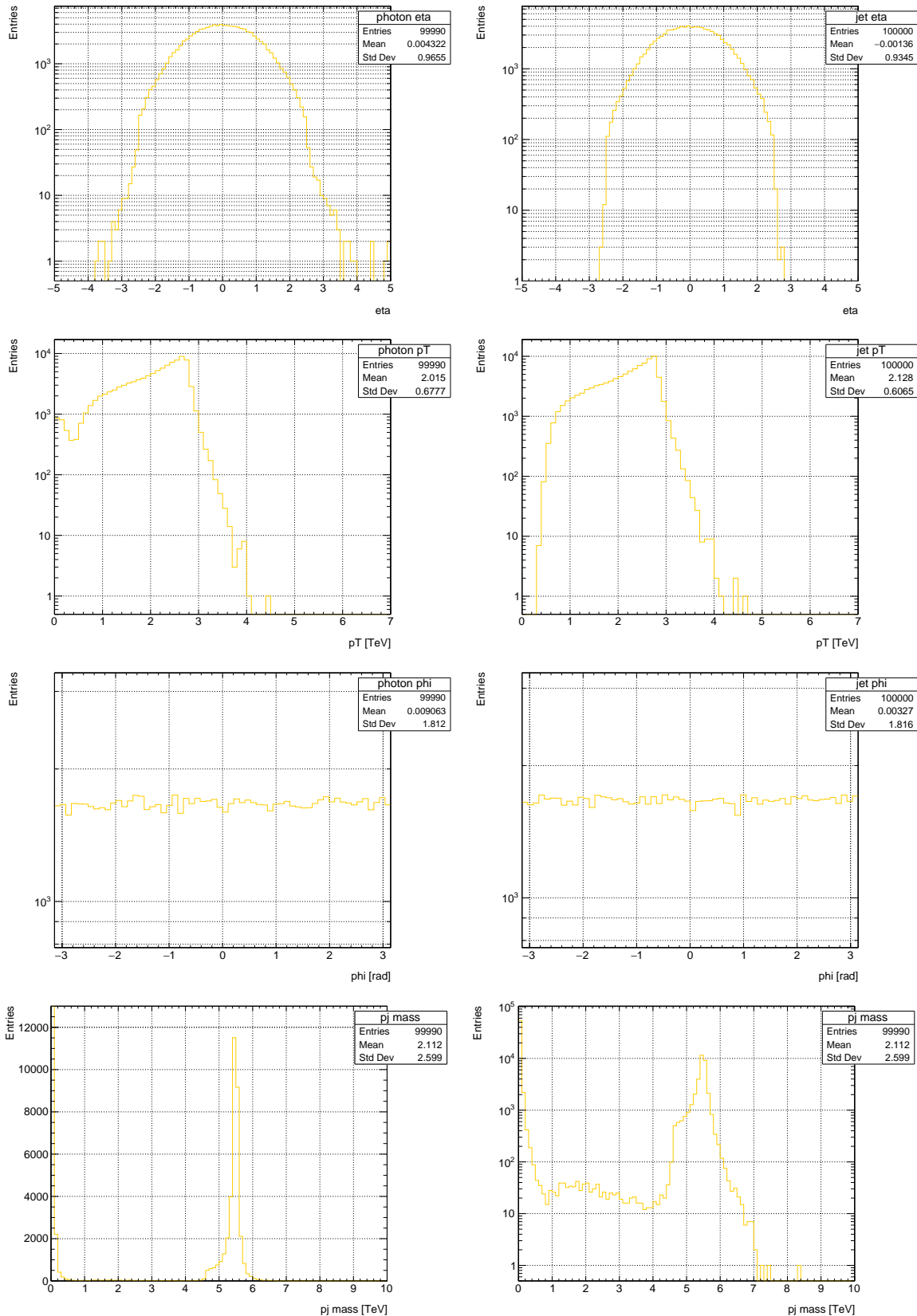
### 9.5.5 $M_s = 7$ TeV, $\sqrt{s} = 13$ TeV



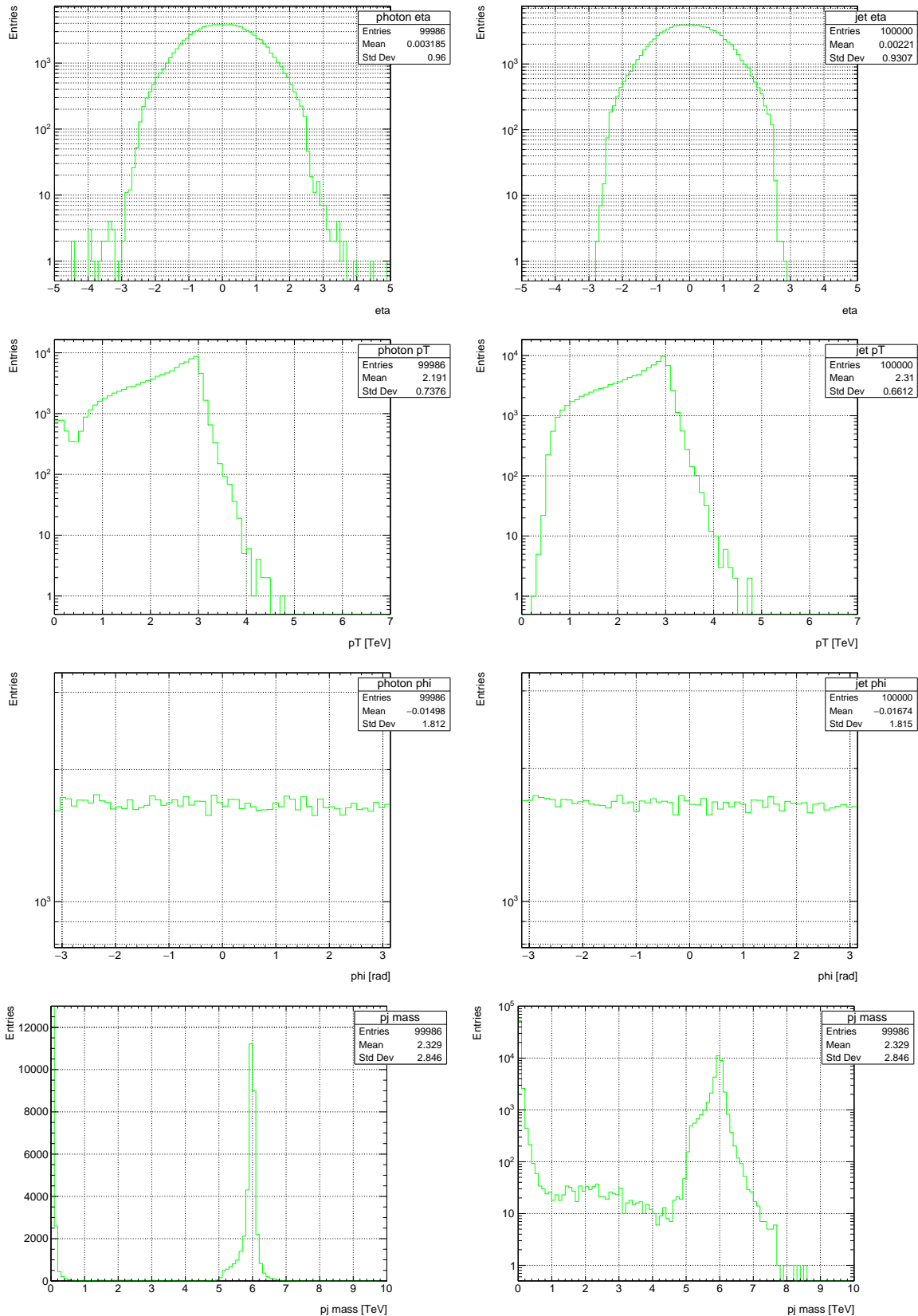
### 9.5.6 $M_s = 5$ TeV, $\sqrt{s} = 13.6$ TeV



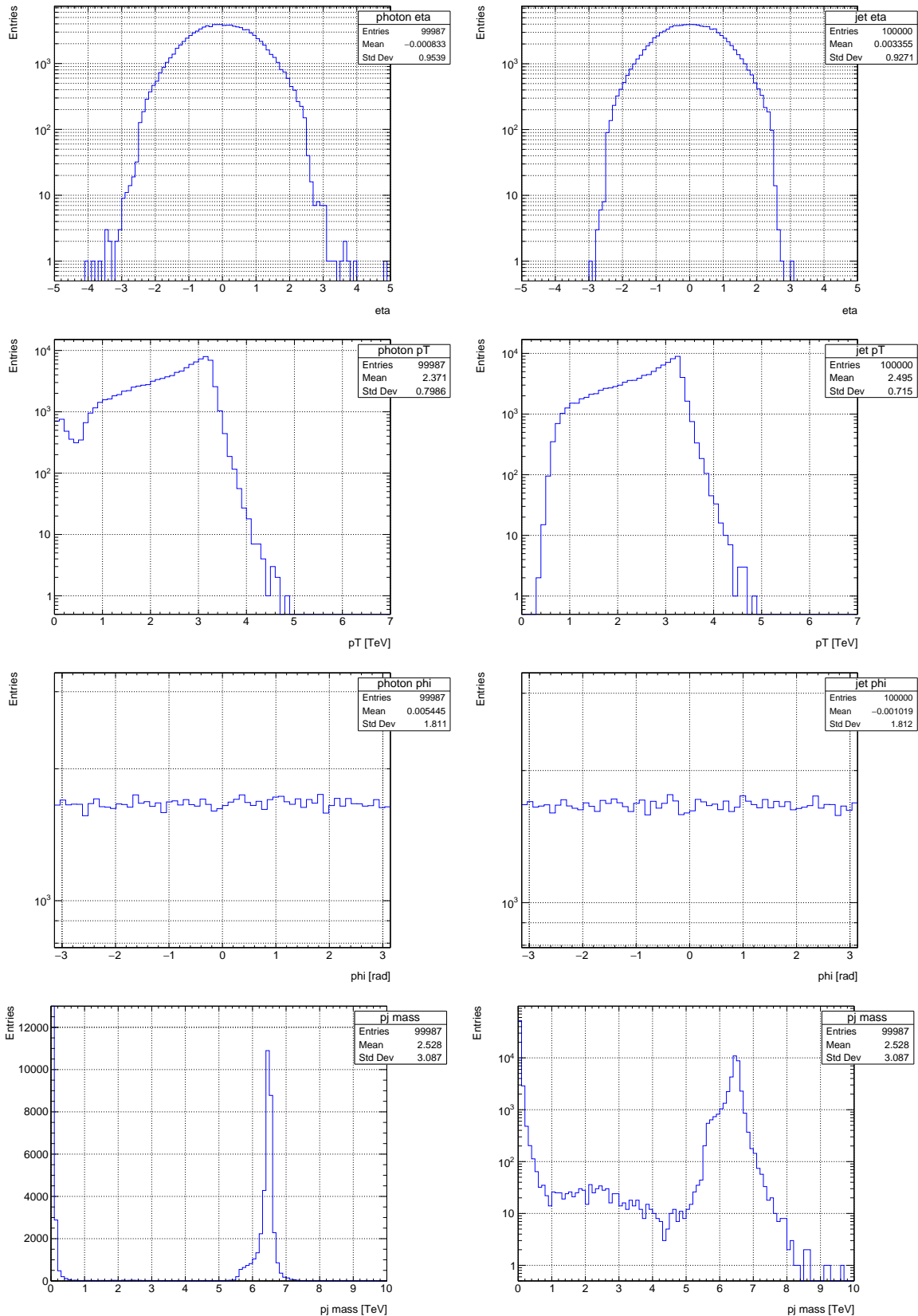
### 9.5.7 $M_s = 5.5$ TeV, $\sqrt{s} = 13.6$ TeV



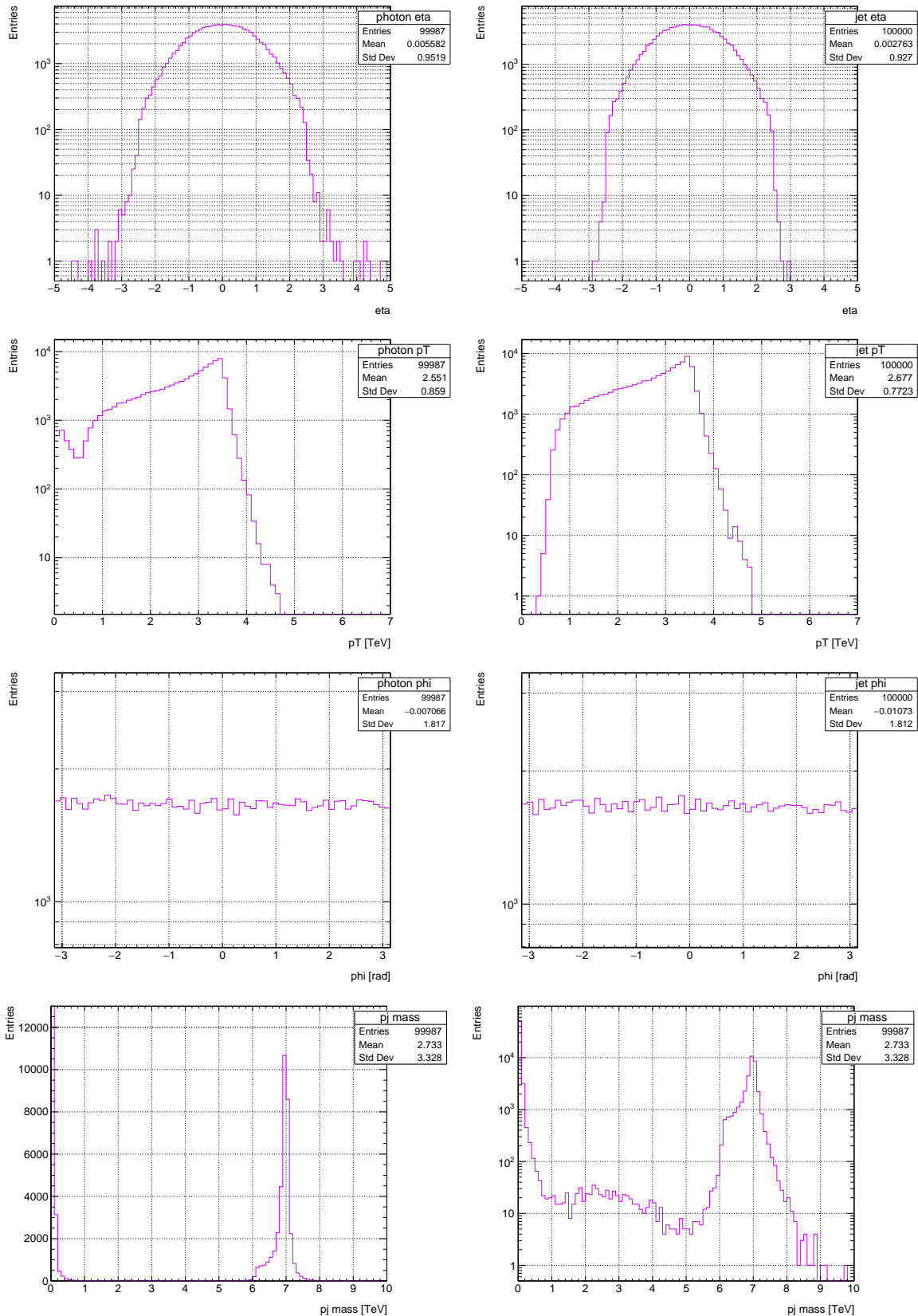
### 9.5.8 $M_s = 6$ TeV, $\sqrt{s} = 13.6$ TeV



### 9.5.9 $M_s = 6.5$ TeV, $\sqrt{s} = 13.6$ TeV



### 9.5.10 $M_s = 7$ TeV, $\sqrt{s} = 13.6$ TeV



## 9.6 Data and MC Samples

Pythia data samples are in the `/hepusers2/kmdrury/athena/24.0.8/TRUTH_mc20` and `/hepusers2/kmdrury/athena/24.` directories:



Figure 55: Subdirectories containing Pythia samples

## 9.7 File Organization on the UofA Local Cluster

Name	Size (KB)
..	1
.alrb	22
.cache	16
.config	12
.emacs.d	2
__pycache__	16
athena	16
EVNTbackups	20
figures	1
july30	1
STRINGS_simulations	1
testFolder	1
testFolder2	1
testFolder3	1
.asetaup	1
.bash_history	1
.cross.txt.swp	1
.data_sort.py.swp	1
.nfs00000000000f67dc00000034	1
.run.sh.sw0	1
.run.sh.swp	1
.strings_v3.py.swp	1
.viminfo	1
.Xauthority	1
batch.sh	1
howToUseVi.txt	1
log	1
main.py	14
run.sh	3
setup.sh	1
strings.py	45
stringsold.py	44

`strings.py` and `main.py` are scripts used for the MC generator and `run.sh` and `setup.sh` are the run and setup shell scripts, respectively. `stringsold.py` is the old version of strings with the *t*-channel bug.

The main STRINGS simulations are contained in the `/STRINGS_simulations` directory (see section 6.2). `/testFolder` contains two LHE files; `150000events.lhe` is the LHE file containing data for the

150,000-event run from section 6.2.1. `y10.lhe` is the LHE file for the 11,000 event running using  $y_{cut} = 10$  (section 6.3.1).

`/testFolder2` contains the 10 LHE files used in the  $y_{cut} = 6$  runs (6.3.1).

The `/athena` is where Pythia simulations are stored, along with the associated root files and programs.

All PLOTS (not figures) used in this report are located in `/figures`. Each subdirectory here is named after a section from this report, and each subdirectory contains all the figures from that section. If a section has no plots, the section will not have a folder.